Synthesis and solution-phase characterization of sulfonated oligothioetheramides.

*Joseph S Brown, Yaset M Acevedo, Grace D He, Paulette Clancy, and Christopher A Alabi*

Robert Frederick Smith School of Chemical & Biomolecular Engineering, Cornell University, Ithaca, NY 14850 USA

## SUPPLEMENTARY INFORMATION

### SUPPLEMENTARY METHODS:

General chemicals were purchased from Sigma Aldrich, Alfa Aesar, or Acros Organics. Fluorous tag and fluorous silica were purchased from Boron Specialties. Routine NMR spectra were recorded on INOVA 400, 500, or 600 MHz spectrometers and analyzed by MestReNova (version 10.0.0). 1H NMR chemical shifts are reported in units of ppm relative to the deuterated solvent. LCMS experiments were carried out on an Agilent 1100 LCMS system with a Poreshell 120 EC-C18 (3.0x100mm, 2.7um) column monitoring at 210nm with positive or negative mode for detection. Solvents for LCMS were water with 0.1% acetic acid (solvent A) and acetonitrile with 0.1% acetic acid (solvent B). A flow rate of 0.6 mL/min was used with a gradient starting at 5% solvent B, followed by a linear gradient of 5% to 95% solvent B over 10 min, 95% solvent B for 2 min, before returning to 0% solvent B over 2 min. Most all tabulated data was processed with GraphPad Prism 7.01.

**Synthesis of the protected sulfonate allyl acrylamide monomer (PSM):**

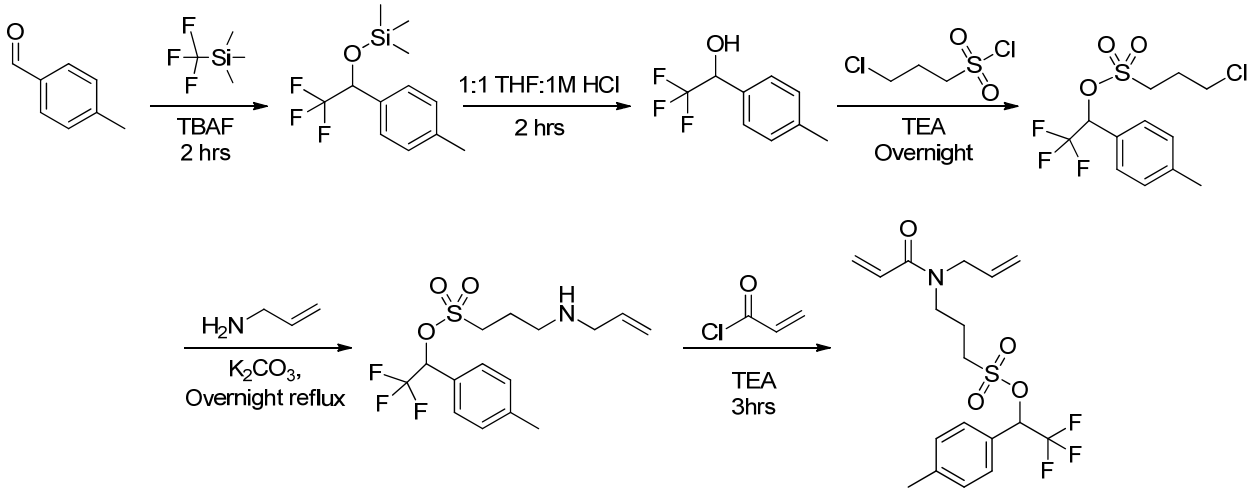


**Figure S1.** Synthetic scheme summarizing the assembly of the protected sulfonate allyl acrylamide monomer (PSM).

The protecting group was prepared as described in S Pauff and S Miller[1] Briefly, 1.4 equivalents of trimethyl(trifluoromethyl)silane was added to a solution of benzaldehyde in THF at 500mM at 0C. Approximately 1 drop per mmol of 1M TBAF solution in THF catalyzed the Ruppert-Prakash reaction and was brought to RT to stir for 1hr. The solution was concentrated and purified by flash

chromatography (0-1% ethyl acetate in hexanes) to give the trimethyl(2,2,2-trifluoro-1-(p-tolyl)ethoxy)silane at 85% yield after purification as a light yellow oil. The age of the silane reagent was seen to be a significant factor for the reaction conversion.

The TMS-protected alcohol was dissolved in 1:1 1M HCl:THF at 250mM and stirred vigorously at RT for 2hrs. The reaction was extracted using ethyl acetate and the combined organic layer was washed with 0.1M HCl, water, and brine. The 2,2,2-trifluoro-1-(p-tolyl)ethanol (TFMT) was obtained as a light yellow liquid in 90% yield.

The TFMT was dissolved in dry DCM at 110 mM with 2.0 equivalents of triethylamine and stirred on ice. 1.3 equivalents of chloropropylsulfonyl chloride was prepared in a 1.3 M solution of DCM and added dropwise. The 100 mM mixture stirred on ice for 1hr and then at RT overnight. The reaction was quenched with water, extracted using DCM washed with 0.1M HCl, water, and brine. Concentration and purification with flash chromatography (0-15% ethyl acetate in hexanes) yielded the 2,2,2-trifluoro-1-(p-tolyl)ethyl 3-chloropropane-1-sulfonate as a white amorphous solid at 90% yield. The melting point was observed to be just above room temperature, but not quantified.

The alkyl halide protected sulfonate was then put through *N*-allyl acrylamide monomer synthesis[2] with modifications. The chloropropane protected sulfonate (2.6 g, 8 mmol) was dissolved into 100 equivalents (800 mmol, 60 mL) of allyl amine and 5 equivalents (40 mmol, 5.6 g) of potassium chloride. The solution was stirred at a 50C reflux overnight. The solution was then filtered over Celite and concentrated to yield an amber oil. The conversion of the chloropropane to the *N*-allyl propane protected sulfonate was checked by NMR and TLC and assumed to be pure. Thus, the *N*-allyl propane protected sulfonate (2.8 g, 8.0 mmol) was dissolved in dry DCM at 150 mM and stirred with 1.2 equivalents of triethylamine. Acryloyl chloride (1.4 equivalents, 11.1 mmol, 880 uL) was diluted in DCM (3mL) and added dropwise. The reaction stirred over 1 hour and then allowed to come to RT for two hours. The reaction was then extracted using DCM and washed with 0.1M HCl, water, and brine. The concentrated amber oil was then purified by flash chromatography using 0-60% ethyl acetate in hexanes to give a clear light yellow liquid in 65% yield.

**General method for fluorous allyl amine synthesis:**
2-[2-(1H,1H,2H,2H-Perfluoro-9-methyldecyl)isopropoxycarbonyloxyimino]-2phenylacetonitrile (fluorous tag) was dissolved in THF (10mg/mL). Two equivalents of allyl amine and two equivalents of triethylamine were added to the reaction mixture and stirred at room temperature for at least 3 hours. Afterward, the THF was completely removed by vacuum centrifuge and the reaction mixture was dissolved in fluorophobic 20% Water in MeOH wash solution, directly loaded onto fluorous silica, and purified by FSPE. Methanol was evaporated under reduced pressure to yield fluorous allyl amine as an off-white solid.

**General method for thiolene reaction:**
Two equivalents of dithiothreitol and 2,2-dimethoxy-2-phenylacetophenone (DMPA, 10 mol % of dithiol) were added to a solution of corresponding fluorous-olefin in methanol (>80 mM). The reaction mixture was UV irradiated for 270 s at 20 mW/cm2. The product (fluorous-thiol) was purified by FSPE. Methanol

was removed by vacuum centrifuge or argon at 40C. The product was confirmed by NMR for reaction completion and purity or DTDP assay for approximate yield.

**General method for Michael addition:**
Two equivalents of the protected sulfonate allyl acrylamide monomer activated by dimethylphenylphosphine (DMPP, 5 mol% of monomer) were added to the fluorous-thiol (variable mM) in methanol. Thirty minutes of reaction time was sufficient to reach completion verified by NMR and DTDP assay at 100mM concentration. The reaction mixture was then purified by FSPE.

**Purification by fluorous solid-phase extraction (FSPE):**
The fluorous column was preconditioned with water (1mL / g of fluorous silica). The fluorous organic mixture was precipitated by adding one-fourth of the reaction volume of water and loaded onto the fluorous silica column (500mg or 2g per scale of reaction). Any remaining fluorous material in the reaction vessel was resolubilized in methanol, again precipitated by water addition, and transferred to the fluorous column. A fluorophobic wash (20 vol% Water in MeOH) was used to elute all non-fluorous molecules while the fluorous-tagged material was retained on the fluorous silica gel (Thiolene wash: 0.33mL/mg of fluorous material; Michael addition wash: 0.5mL/mg of fluorous material). A fluorophilic wash of methanol was then used to elute the fluorous material (0.2mL/mg fluorous material). For the FSPE purification of the MeS containing oligomers, the wash solution was made more fluorophobic by the addition of water up to 60 vol%.

**Generalized method for oligoTEAs synthesis:**
Fluorous allyl amine was synthesized and cycled through the thiolene and Michael additions until desired oligomer length was reached as described. Upon completion, oligoTEAs were treated with 5mM TFA with 5 v/v% DI water for 2hrs if the PSM was used in its preparation; otherwise, the oligoTEA was treated with 1:1 TFA:DCM at 5mM. Then, the mixture was dried at room temperature under argon and HPLC purified.

**Assay of organic thiol concentration by 2,2' dithiodipyridine (DTDP):**
Thiol concentration was qualitatively assessed after purification at the end of each thiolene and during the Michael addition to track the oligoTEAs synthesis. Following previously published procedure[3,4] 5uL of 12mM DTDP and 300uL of 0.1v/v% TEA in DMSO were prepared for each assay sample. Aliquots of fluorous material were added to the assay such that the concentration would be 100uM, mixed, and allowed to sit for 3-5 minutes. The reaction was quenched with 10uL of acetic acid and 150uL were analyzed by an absorbance scan from 325-450 nm (step size 2nm). Spectra were normalized to 450nm and analyzed.

**HPLC purification of oligoTEAs**
HPLC purification was performed on an 1100 Series Agilent HPLC system using a reverse phase Agilent Eclipse Plus C18 column (4.6x150 mm, 5µm) or an Agilent Eclipse XDB-C18 (9.4x250mm, 5µm) column and collected using an automated fraction collector. The column compartment was kept at 30°C. Solvents for HPLC were water with 0.1% trifluoroacetic acid (solvent A) and acetonitrile with 0.1% trifluoroacetic acid (solvent B). Compounds were eluted at a flow rate of 1 mL/min or 4 mL/min over specified gradients.

**Pulse-field gradient nuclear magnetic spectroscopy (PFG NMR)**

Measurements were performed with a Varian Unity INOVA 600MHz spectrometer equipped with a Varian 600 triple resonance XYZ PFG (HCN) inverted probe. 1H spectra were first acquired with optimized 90° pulse angle from -2 to 14 ppm using 4 scans, a relaxation delay of 2 seconds, and an acquisition time of 1.7 seconds. Diffusion measurements were accomplished using the double-stimulated echo convection compensated sequence[5] using 3mm tubes and 20 LPM of VT gas flow to diminish convection. Measurements were completed with an array of 20 linearly developed pulse field gradient strengths, an acquisition time of 1.7 seconds, 8 steady state pulses, diffusion gradient length of 2.0 milliseconds (ms), 0.0 ms of off-center delay (del2), 0.00 unbalancing factor, and alternating gradient pulse sign. The diffusion delay was set to 120 ms as it attenuated the $(DTT\text{-}Sulf)_5$ to approximately 10% of its original intensity at the maximum gradient pulse. Scout diffusion measurements of small scan numbers were completed to estimate and determine the best gradient stabilization delay (1.0-2.5 ms) to minimize the phase errors caused by eddy currents[6]. A standard of 99.9% D2O was run to calibrate the probe (gcal) by the observed diffusion coefficient of HDO for each temperature as described by a Speedy-Angell power law fit[7] of Longsworth's data[8] (Figure S2, Equation S1). Example processing is shown in Figure S4 and S5.

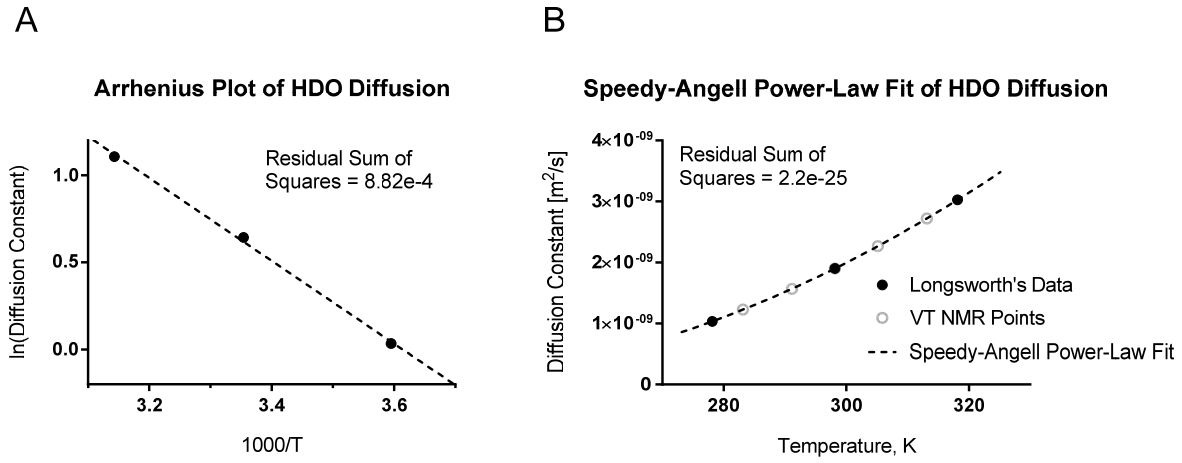


**Figure S2. A.** Arrhenius plot of HDO diffusion in 99.9% $D_2O$ as measured by Longsworth[8]. The Arrhenius plot can fit diffusion data in a linear fashion with some small error. **B.** As seen in literature,[7] a better fit can be achieved using the Speedy-Angell power-law using parameters listed in Equation S1 to eliminate nearly all error. This data allowed a control experiment to measure the HDO diffusion in 99% D2O at each temperature provided as described in literature[6].

$$D = D_0\left[\frac{T}{T_s} - 1\right]^{\gamma} \quad ; \quad D_0 = 1.62421 \times 10^{-4},\ T_s = 223.36,\ \gamma = 1.96$$

**Equation S1.** The Speedy-Angell power-law as applied to translational diffusion. While an Arrhenius plot does show appreciable linearity of HDO diffusion measured by Longsworth[8], systemic error can be

reduced by the use of the Speedy-Angell power-law as previously seen[7]. Fitted parameters to Longsworth data are listed and used in Figure S1.

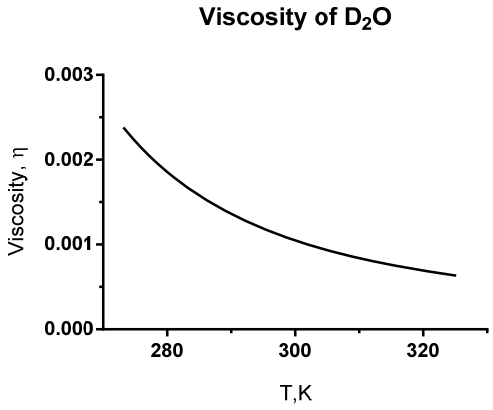


**Figure S3.** Plot of D2O viscosity that was utilized in DOSY analysis from J Lapham et al[9]. This data was used in the analysis of PFG NMR data.

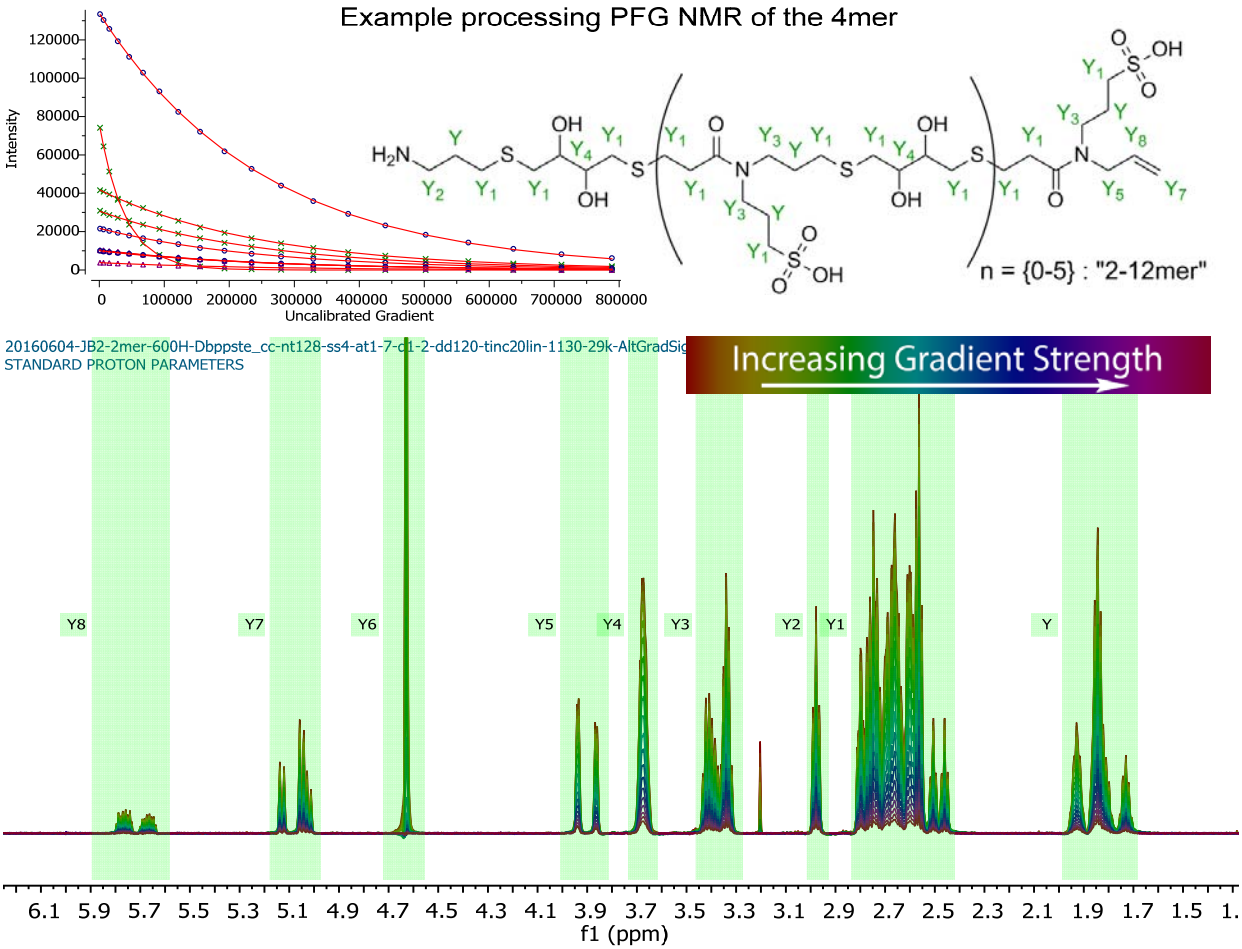


**Figure S4.** Example of PFG NMR processing of the 2mer at 25C. Acquisition parameters are in Supplemental Methods. 1H spectra was examined for quality signal-to-noise and phase errors associated with eddy currents, phased manually, and baseline corrected. Sets of peaks were integrated as a function

of the pulse field gradient strengths that was applied to reveal a single exponential decay of each molecule. This serves as an example for all collected PFG NMR spectra.

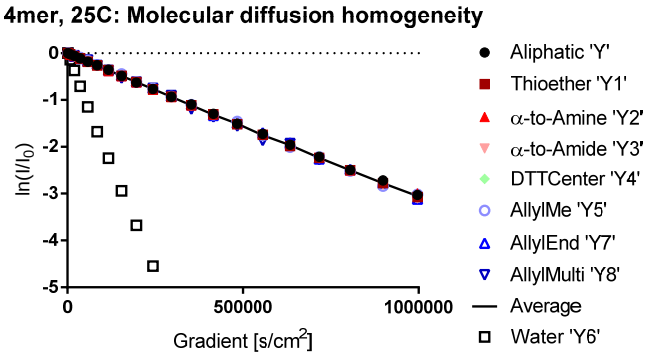


**Figure S5.** The natural logarithm of the normalized intensity versus the calibrated gradient strength to observe the molecular diffusion homogeneity of the 4mer at 25C. Individual sets of peaks from different regions of the oligomers demonstrate that the end of the oligomer (e.g. allyl protons Y5, Y7-8) diffuses the same as the backbone of the oligomer (e.g. aliphatic Y or thioether Y1). This observation demonstrates there were no major differences between the end and backbone groups. This serves as an example for all spectra.

**Conjugation of Proxyl to sulfonated oligoTEAs:**

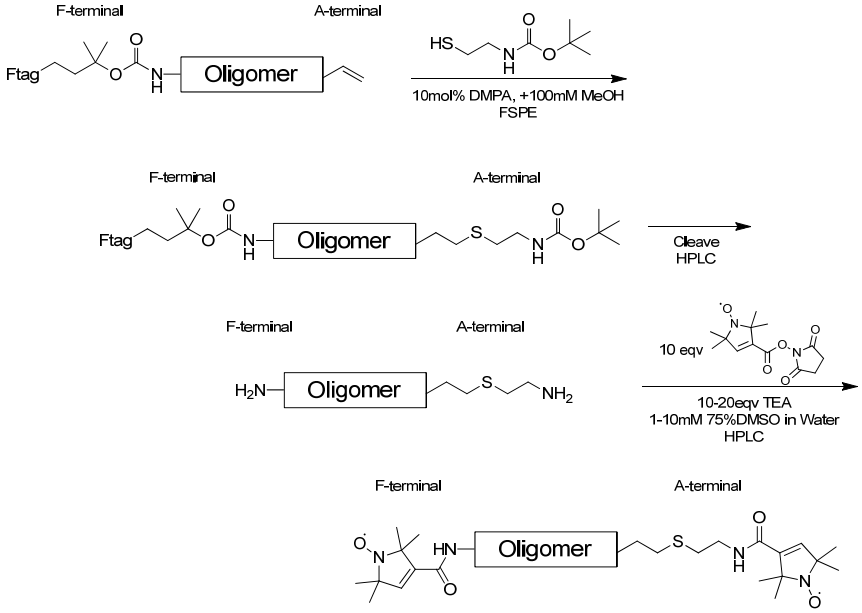


**Figure S6.** Synthetic scheme to produce di-spin labeled sulfonated oligoTEAs.

Before TFA cleavage of the fluorous support, 3 equivalents of 2-(Boc-amino)ethanethiol and DMPA (10 mol%) were reacted with the elongated oligoTEA allyl (A) terminal. Cleavage and HPLC purification was completed as described generally. During confirmation of the cleaved product by 1H NMR, 19F NMR was completed with a trifluoroethanol standard to quantify residual trifluoroacetic acid (TFA) from

the HPLC to inform the equivalency of base to be used in subsequent conjugation. The confirmed oligoTEA was reacted with 5 equivalents of 2,2,5,5-Tetramethyl-3-pyrrolin-1-oxyl-3-carboxylic acid N-hydroxysuccinimide ester (PROXYL NHS ester) and with 5-20 equivalents triethylamine at 1-10mM in 30% water in DMSO at room temperature for 4 hours. Upon reaction completion, the di-spin labeled oligoTEAs was HPLC purified and confirmed by LCMS.

**Electron spin resonance distance measurements:**
ESR measurements were completed at the Advanced Electron Spin Resonance Technology (ACERT) Center. Di-spin labeled oligoTEAs were reduced using aqueous ammonia for 1-2 hours at 50-500uM at room temperature. Some samples as labeled were dialyzed against ultrapure water using a 100-500 MWCO Micro-Float-A-Lyzer (Spectrum Labs) and monitored by a calibrated Accumet Four Cell Conductivity/ATC probe (Cat 13-620-165) with an Accumet Excel XL20 conductivity meter. All samples were prepared at 100 uM and vitrified to 70K rapidly from room temperature. A working frequency of 17.3 GHz with a 30G magnetic component in a rotating reference frame was sufficient for distances of 10 Å or longer. Most samples were measured by 4-pulse sequence double electron-electron resonance (DEER) and some were measured by double quantum coherence (DQC). Time domain data was processed in MATLAB; an example is shown in Figure S16. Then, distance distributions were calculated by Tikhonov regularization based on the L-curve method ($\alpha \sim 2$-7) using modified MATLAB scripts from the ACERT website (acert.cornell.edu).

**Molecular Dynamics Simulations:**
The oligomer simulations were run in LAMMPS, Sandia's molecular dynamics software package[10]. A single oligomer chain was simulated for 50 ns with 1 fs timesteps in a water-filled box with periodic boundary conditions to simulate the motion of disperse oligomers in aqueous solution. An isothermal, NVT, ensemble was implemented in the MD simulation using a Nosé−Hoover thermostat set to 300 K. The OPLS (Optimized Potential for Liquid Simulations) force field developed by Jorgensen[11] was used for the oligomers and is expected to well represent the system since OPLS parameters are optimized to fit experimental properties of liquids, such as density and heat of vaporization, in addition to fitting gas-phase torsional profiles. To supplement the core OPLS parameters, the sulfonate parameters were taken from research by J N C Lopes, A A H Padua, and K Shimizu which studied ionic liquids.[12,13] Since ionic liquid properties are heavily derived from charge interactions, we expect this force field to appropriately handle charge contributions to the system's dynamics. Finally, the force field selected for the water solvent was the TIP4P model, which offers a good compromise between computational efficiency and charge accuracy.[14]

Accurately simulating an isolated oligomer required careful design of physical constraints and charge constraints. The periodic simulation box was made large enough to minimize self-interaction errors. This was done by running a relatively long 10 ns simulation for each oligomer size to determine the approximate end-to-end distance distribution. Less than 1% of the collected data is affected by self-interaction. The box sizes selected were from 3.7 nm for the shortest oligomers to 7 nm for the longest oligomers. The amount of water molecules required to fill those respective simulation boxes, ranged from 1700 molecules to 7200 molecules. The total amount of atoms simulated, including the oligomer, ranged from 5100 atoms to 22000 atoms.

The charge calculation was done using a long-range particle-particle particle-mesh solver in LAMMPS. In solution, the $(DTT\text{-}Sulf)_{1\text{-}6}$ have a permanent negative charge on each sulfonate group. Charge neutrality was achieved in the simulations by using sodium ions.

**Circular dichroism measurements (Figure S17):**
Spectra were collected from 185-400nm (2nm step size) on an AVIV Biomedical Circular Dichroism Spectrometer Model 400 (Lakewood, NJ) using a 0.2cm cuvette filled with 700uL of oligoTEA at variable concentration {45-300uM}. The automatically calculated CD signal, Dynode (PMT voltage), CD current (Abs), CD Delta – Absorbance (Raw data) were collected. Sample concentration was found to be optimal at approximately 200uM based on a maximized Dynode (PMT voltage) with regards to the resulting signal to noise.

**DIFFUSION THEORY**
Compiled and made explicit from Stokes-Einstein-Sutherland, Chen and Chen[15], and G. de la Torre[16], and F. Perrin[17–19] with a review by A. Macchioni[20].

$$D_t = \frac{k_B T}{f} = \frac{k_B T}{c(r_H) f_S(p) \pi \eta r_H} \xrightarrow{for\ "large"\ spheres} \frac{k_B T}{6\pi\eta r_H}$$

**Equation S2.** Stokes-Einstein-Sutherland (SES) equation relating the Boltzmann temperature and the translational molecular diffusion where $k_B$ is the Boltzmann constant, T is the temperature in Kelvin, $r_H$ is the prospective hydrodynamic radius, η is the dynamic viscosity, c is a size-dependent modification to transition between the slip/no-slip boundary conditions, p is the geometrically defined aspect ratio, and $f_s$ is the shape-modified friction factor.[20]

$$D_t = \left(\frac{k_B}{c(r_H) f_S(p) \pi r_H}\right) \frac{T}{\eta}$$

**Equation S3.** Algebraic rearrangement of the SES equation to clearly show that if there is a linear relationship between the translational diffusion and the normalized temperature (T/η), then the quantity in the parentheses is equal to the slope, if linear and constant.

$$\alpha \equiv \left(\frac{k_B}{c(r_H) f_S(p) \pi r_H}\right) \rightarrow \beta \equiv \frac{k_B}{\alpha\pi} = c(r_H) f_S(p) r_H$$

**Equation S4.** Definition of the slope from Equation S2 and algebraic rearrangement to yield a purely experimentally derived parameter (β) as it constrains the prospective size and aspect ratio, two unknown parameters.

$$c(r_H) = \frac{6}{1 + 0.695\left(\frac{r_{solv}}{r_H}\right)^{2.234}} \qquad 4 < c(r_H) < 6$$

**Equation S5.** Microfrictional correction to the SES by H Chen and S Chen relating the van der Waals radius of the solvent to the prospective molecule hydrodynamic radius. The expression was derived to

correct the translational diffusion of crown ethers, which are notably smaller than the prospective sulfonated oligoTEAs[15].

$$f_{Prolate} = \frac{\sqrt{1-p^2}}{p^{2/3}\ln\left(\frac{1+\sqrt{1-p^2}}{p}\right)} \;\; ; \;\; p \equiv \frac{b}{a} < 1$$

**Equation S6.** The friction factor for a prolate ellipsoid as defined by F Perrin 1934,1936 and corrected by S Koenig 1975 with the limits of the aspect ratio[17–19].

$$f_{Oblate} = \frac{\sqrt{p^2-1}}{p^{2/3}\arctan\left(\sqrt{p^2-1}\right)} \;\; ; \;\; p \equiv \frac{b}{a} > 1$$

**Equation S7.** The friction factor for an obalte ellipsoid as defined by F Perrin 1934 and1936 with the limits of the aspect ratio[17,18].

$$\begin{aligned} f_{Rod} = {} & 1.009 + 1.395\times10^{-2}(\ln p) \\ & +7.88\times10^{-2}(\ln p)^2 \qquad ; \;\; 0.1 < p \equiv \frac{L}{d} < 20 \\ & +6.040\times10^{-3}(\ln p)^3 \end{aligned}$$

**Equation S8.** The semi-emperical friction factor for a rod as defined by A Ortega and J García de la Torre with the limits of the aspect ratio[16].

$$V_{equivalent\ sphere} = V_{shaped} = \frac{4}{3}\pi {r_H}^3$$

$$V_{Rod} = \pi r^2 L \rightarrow r_H = \sqrt[3]{\frac{3r^2L}{4}}$$

**Equation S9.** The volumetric constraint that assumes the prospective oligomer shape fills a volume that to be equivalent in volume to a sphere described by the hydrodynamic radius, $r_H$. The parameters in these equations are described in Figure S7 where r is the geometric rod radius, and L is the rod length.

$$d_{ESR} = long\ dimension\ of\ rod = L \rightarrow r = \frac{d_{ESR}}{2}$$

$$p \equiv 0.1 < \frac{L}{2r} < 20 = \frac{d_{ESR}}{2r} \rightarrow r = \frac{d_{ESR}}{2p}$$

$$r_H = \sqrt[3]{\frac{3r^2L}{4}} = \sqrt[3]{\frac{3{d_{ESR}}^3}{16p^2}}$$

$$\beta = c(r_H) f_S(p) r_H = \frac{6}{1 + 0.695\left(\frac{r_{solv}}{\sqrt[3]{\frac{3d_{ESR}{}^3}{16p^2}}}\right)^{2.234}} \times \sqrt[3]{\frac{3d_{ESR}{}^3}{16p^2}} \times \begin{bmatrix} 1.009 + 1.395 \times 10^{-2}(\ln p) \\ +7.88 \times 10^{-2}(\ln p)^2 \\ +6.040 \times 10^{-3}(\ln p)^3 \end{bmatrix}$$

**Equation S10.** Algebraic result of the final expression relating the diffusion constant within β to the constrained SES with the rod model, assuming the ESR distance applies in the long dimension as described by Figure S7. This equation was solved using fsolve in MATLAB R2013a with MaxIter = 800, MaxFunEvals = 200, a tolerance of $10^{-25}$, and a multiplier on the residual of $10^{15}$.

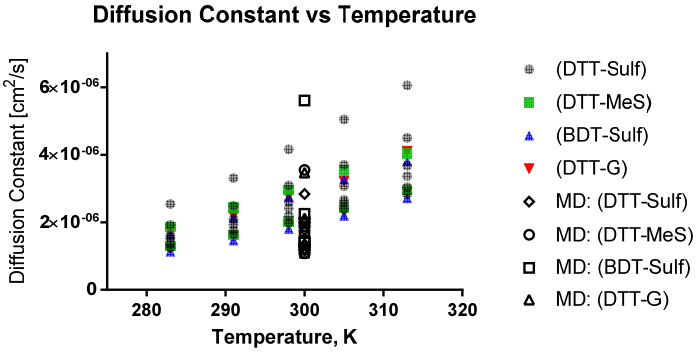


**Figure S7.** All diffusion data from both PFG NMR and single-chain MD simulations in water. Similar range of diffusion and trends were observed, providing validation for the MD simulations with respect to the oligomer dynamics. At most a factor of 3 difference was observed between the PFG NMR and MD, which is reasonable for a macroscopic property.

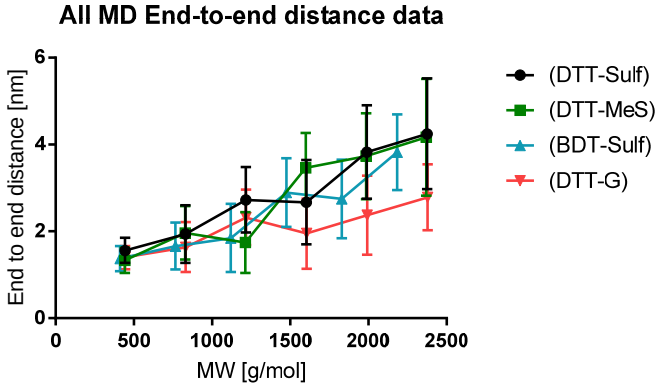


**Figure S8.** All end-to-end distance measurements produced by single-chain molecular dynamics (MD) simulations at 300K in explicit water solvent versus the oligoTEA molecular weight. Error bars represent standard deviation of the end-to-end distance over the MD time evolution.

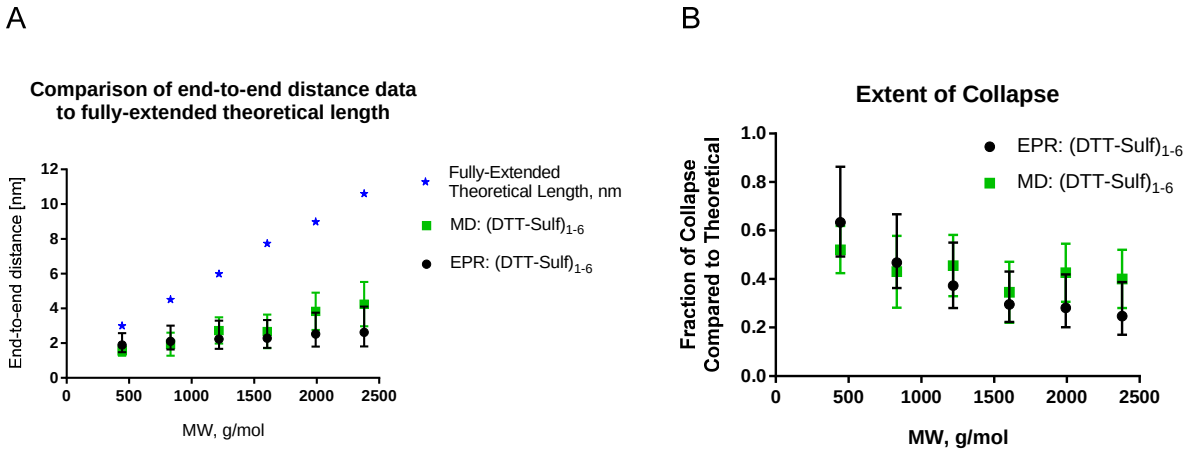


**Figure S9. A.** Comparison of the fully-extended theoretical length of 100uM $(DTT\text{-}Sulf)_{1\text{-}6}$ oligoTEAs in 20% ethylene glycol in water vitrified to 70K from room temperature revealing the extent of molecular collapse experienced in solution. All oligomers appear to experience some level of collapse likely due to entropy, hydrophobic collapse, and/or screening of intramolecular electrostatic repulsion. **B.** Calculation of the fraction of $(DTT\text{-}Sulf)_{1\text{-}6}$ oligoTEA collapse.

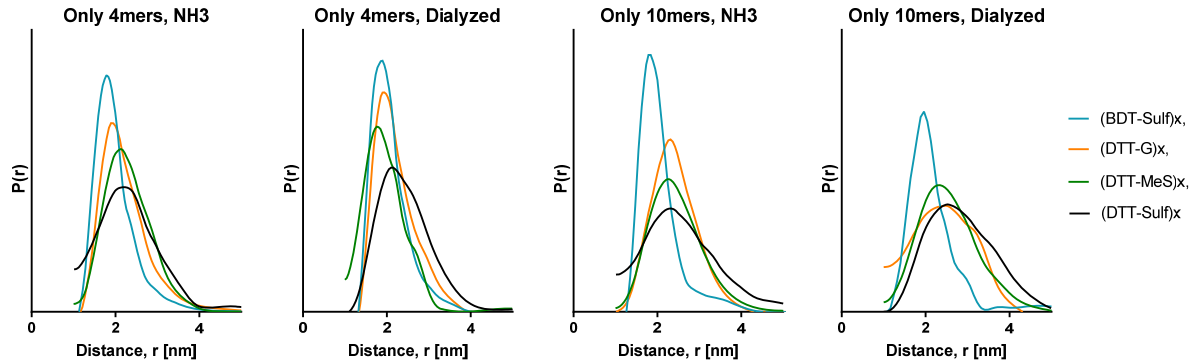


**Figure S10.** All end-to-end distance reconstructions of DEER distributions of (BDT-Sulf)2,5 in blue, (DTT-G)2,5 in red, (DTT-MeS)2,5 in green, and (DTT-Sulf)2,5 in black measured by DEER and DQC EPR. Samples were measured at 100 uM in 20% ethylene glycol in water and vitrified to 70K from room temperature. Detail is described in Supplementary Methods.

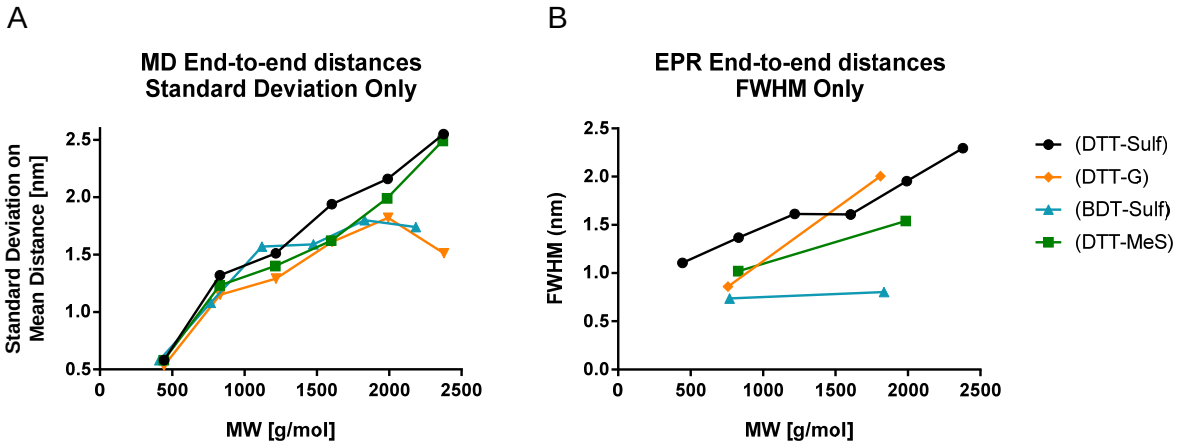


**Figure S11. A.** The standard deviation on the mean end-to-end distance calculated by single-chain MD simulations (300K, explicit water solvent), which qualitatively assesses the size of the conformational space. **B.** The full-width at half maximum (FWHM) of the EPR distance distributions. In almost all cases, the DTT-MeS has a smaller distribution width (SD or FWHM) than other hydroxylated oligomers, with the exception of $(DTT\text{-}G)_2$.

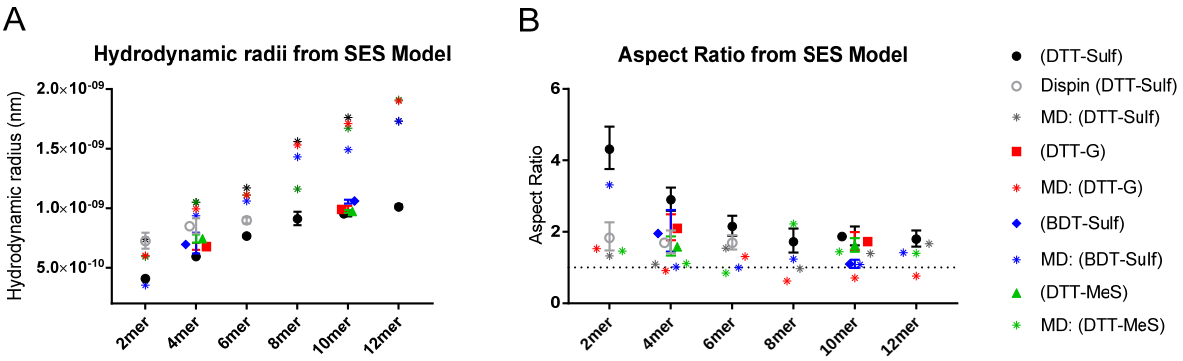


**Figure S12.** Results from solutions of the SES model utilizing the rod model assuming the end-to-end distance data describes the long dimension (length) of the rod. **A.** Hydrodynamic radii results derived from the DEER data (solid lines) and MD (dashed lines). **B.** The aspect ratio calculated simultaneously in the SES solution. The PEG3 is also reported from an additional control experiment. In both graphs, the error bars represent the distribution propagated through the SES model (SD from MD, FWHM from DEER).

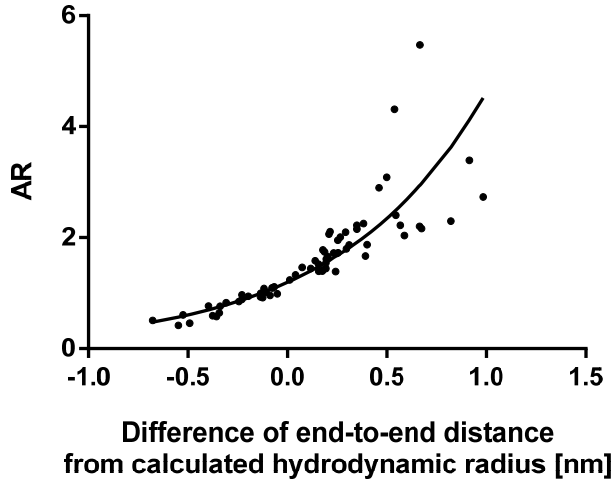


**Figure S13.** The correlation between the difference of the end-to-end distance from DEER or MD input into the SES model (solved in MATLAB) and the calculated hydrodynamic radius versus the aspect ratio. An exponential fit is shown for illustration. This correlation demystifies the SES method by showing that the end-to-end distance as it differs from the hydrodynamic radius produces the aspect ratio. Thus, the accuracy of the end-to-end distance measurement is very important to measure an accurate aspect ratio.

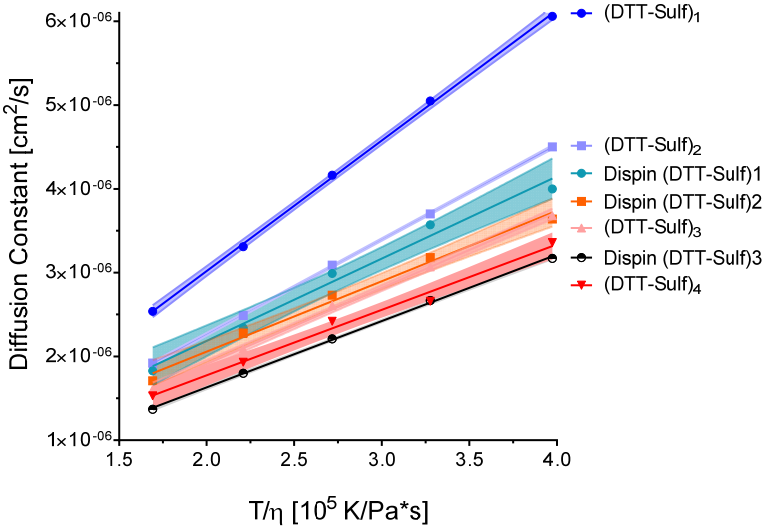


**Figure S14.** Variable temperature diffusion measurement of 1-3 mM regular and dispin labeled (DTT-Sulf) oligomers in $D_2O$.

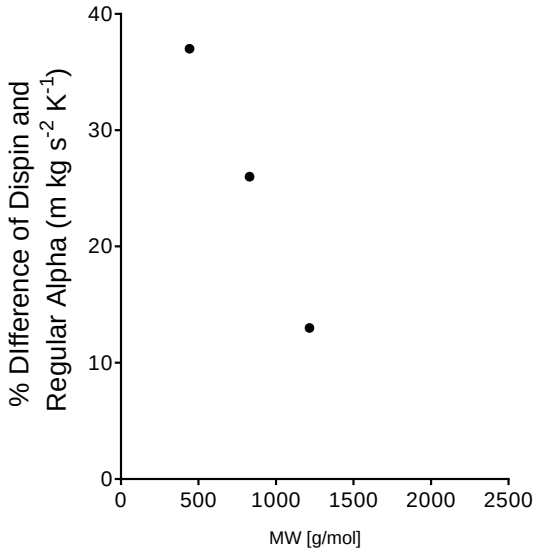


**Figure S15.** The difference between the dispin labeled and regular oligomer diffusion, demonstrating a significant increase at low oligomer lengths, where the spin label contributes significantly to the oligomer diffusion.

## SUPPLEMENTARY SPECTRA (EPR, CD, NMR, LCMS)

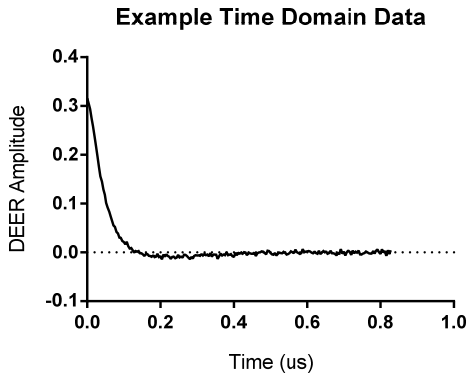


**Figure S16.** Example time domain data collected from DEER of 100 uM dispin labeled oligoTEAs in 20% ethylene glycol vitrified to 70K from room temperature.

Oligomers were synthesized with L(-)-DTT as described, purified by HPLC, and measured with circular dichroism (CD), showing chirality of monomer units is maintained during synthesis (Figure S7).

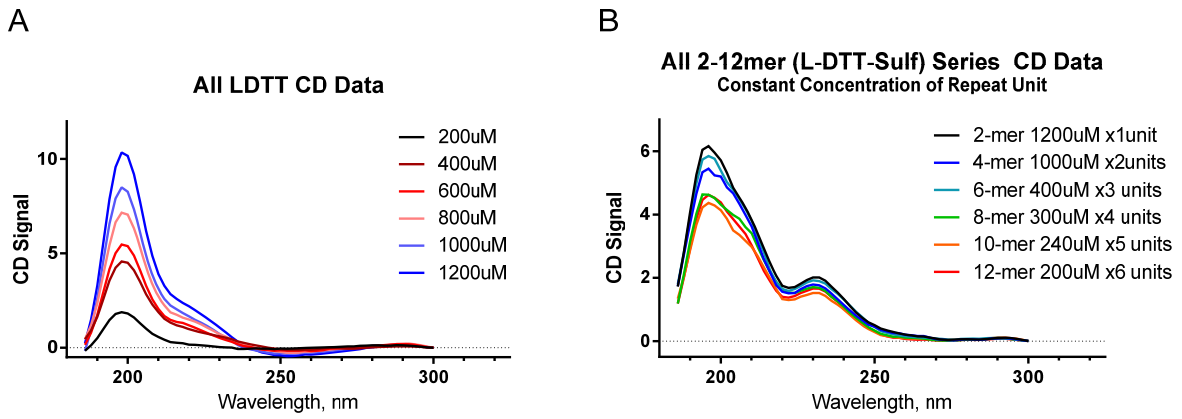


**Figure S17. A.** Circular dichroism data of L(-)-DTT as a control and **B.** 2-12mer sulfonated hydroxylated oligoTEAs at room temperature in water. The oligoTEA CD can be normalized by the concentration of the repeat unit of thiolene and Michael addition cycle. The L(-)-DTT has clear signals on its own at 200 and 220 nm, which are slightly modified when incorporated in to the oligomer, which shows signals at 200 and 232 nm. There is not any evolution of the CD signal as a function of synthetic length, indicating no clear secondary structure is developed.

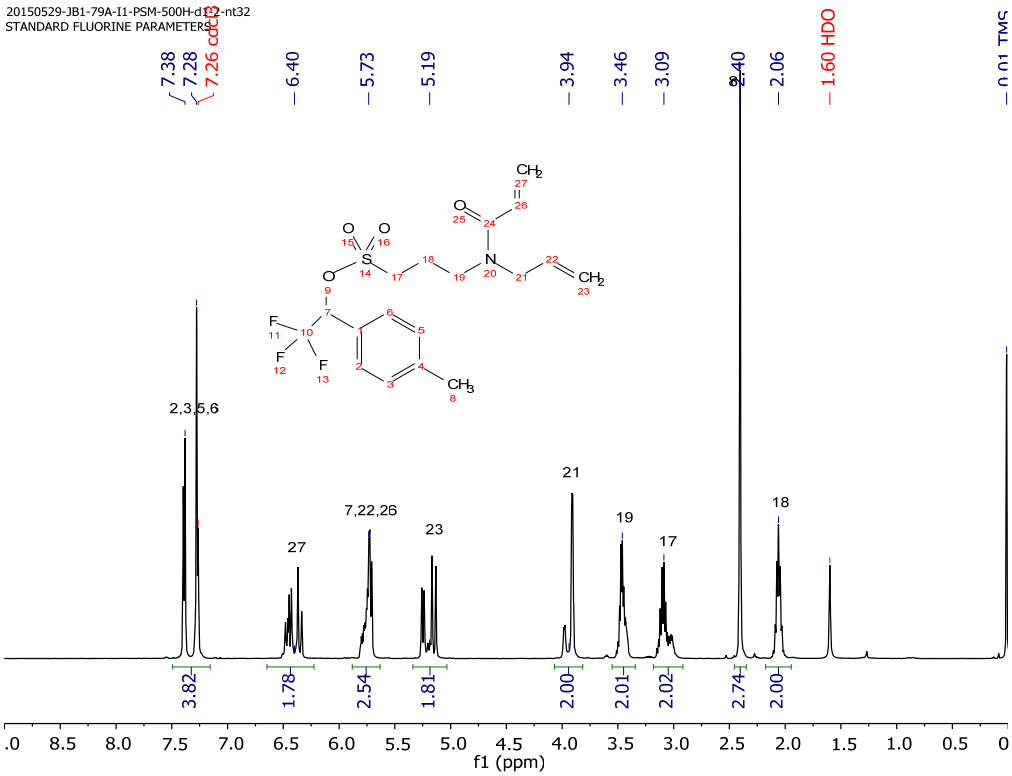


**Figure S18.** $^{1}$H NMR of the protected sulfonate *N*-allyl acrylamide monomer (PSM) in d-chloroform.

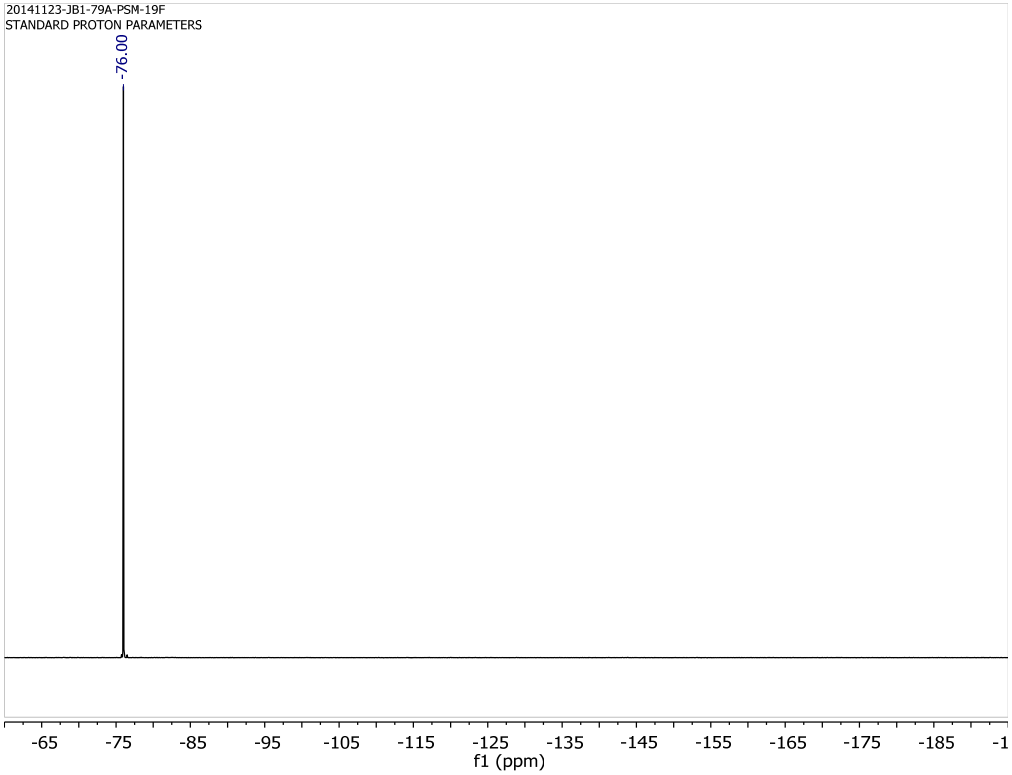


**Figure S19.** $^{19}$F NMR of the PSM in d-chloroform.

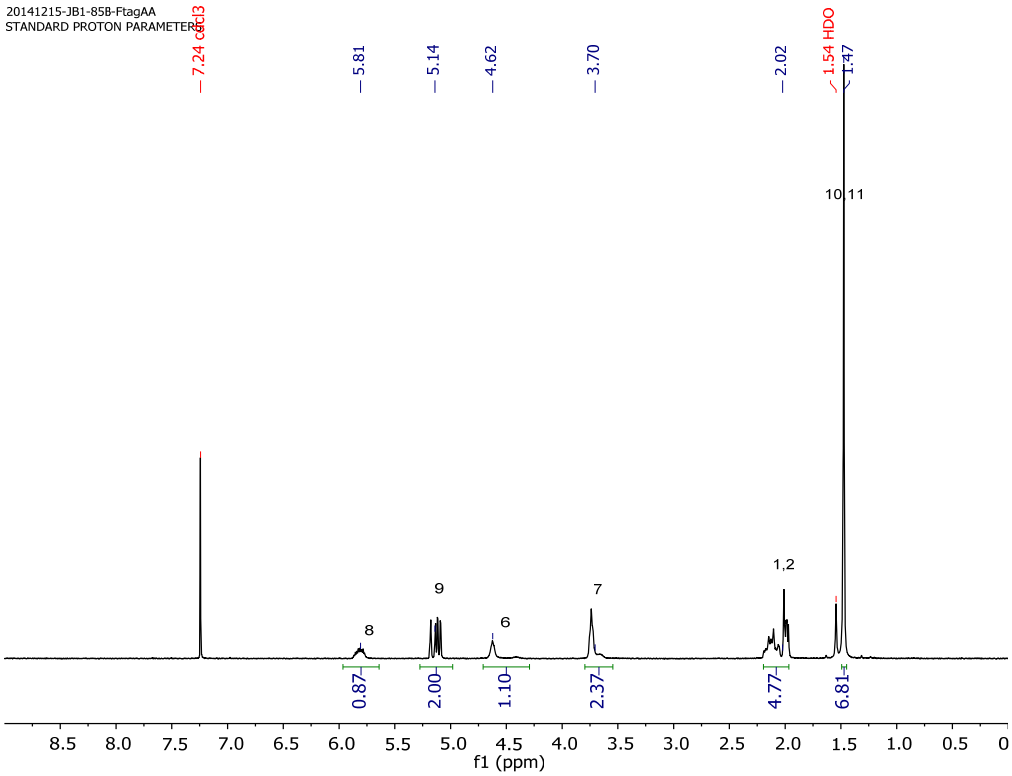


**Figure S20.** [1]H NMR of "fluorous allyl amine" or 5,6,6,7,7,8,8,9,9,9-decafluoro-2-methyl-5-(perfluorobutyl)nonan-2-yl allylcarbamate in d-chloroform.

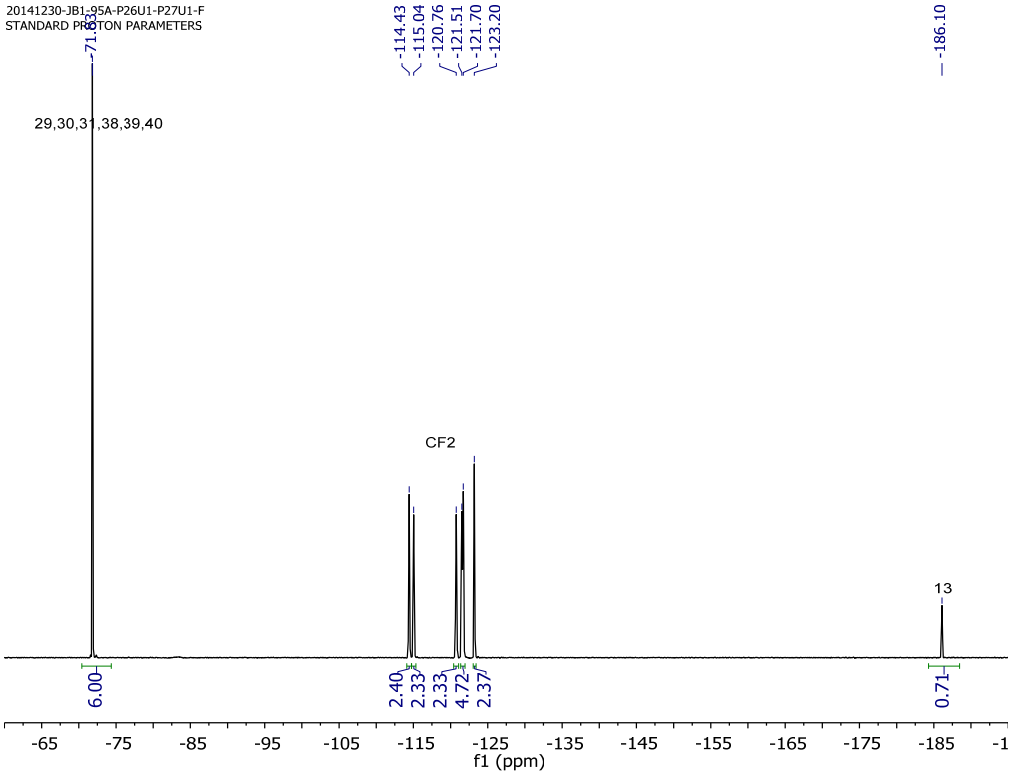


**Figure S21.** [19]F NMR of "fluorous allyl amine" or 5,6,6,7,7,8,8,9,9,9-decafluoro-2-methyl-5-(perfluorobutyl)nonan-2-yl allylcarbamate in d-chloroform.

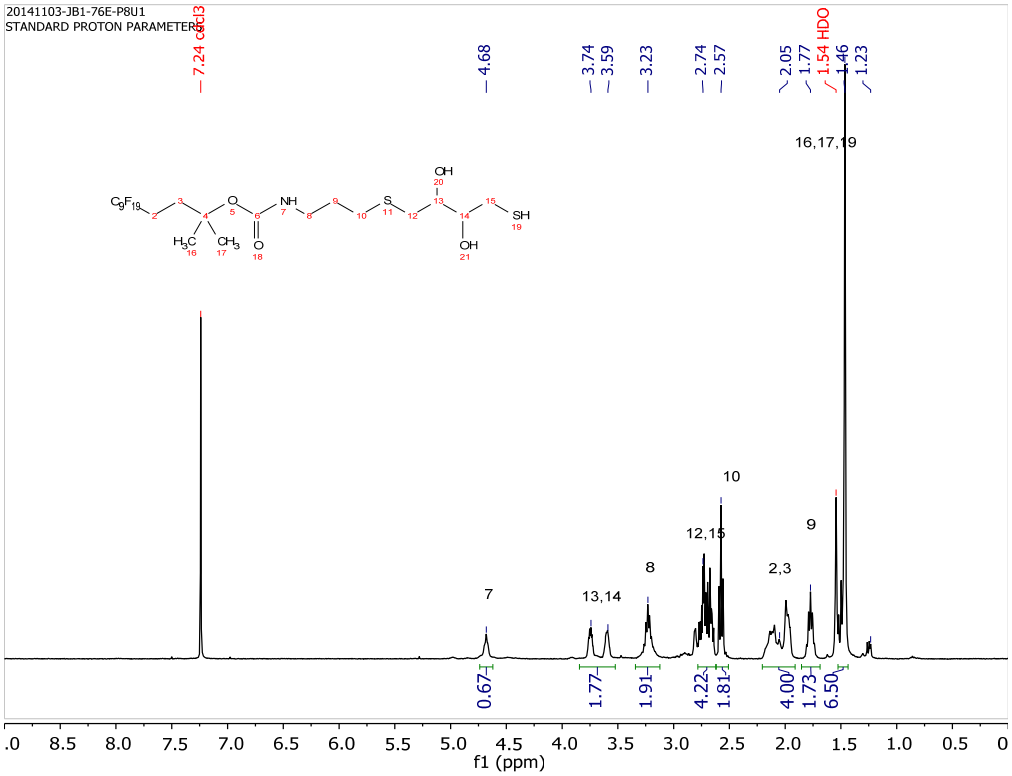


**Figure S22.** $^{1}$H NMR of "fluorous DTT" the fluorous purified product of the thiolene reaction of fluorous allyl amine and DTT in d-chloroform. Note the disappearance of the allyl peaks.

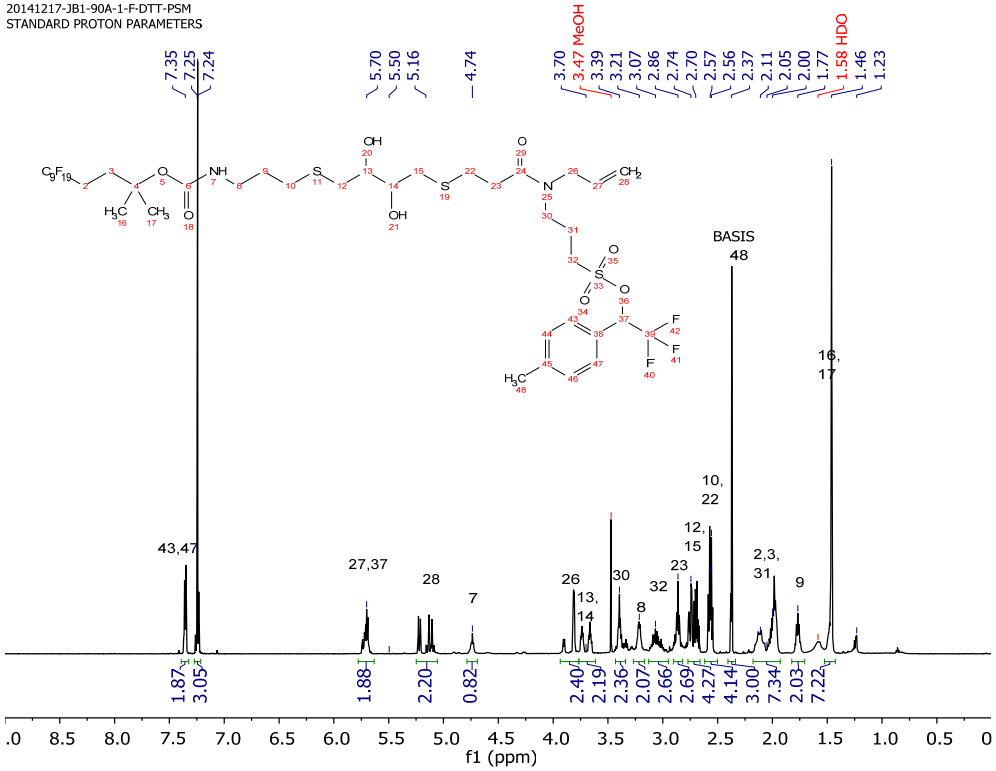


**Figure S23.** $^{1}$H NMR of "fluorous DTT-PSM" the FSPE purified product of fluorous DTT and the protected sulfonate allyl acrylamide monomer thiol-Michael in d-chloroform. Note the allyl peaks.

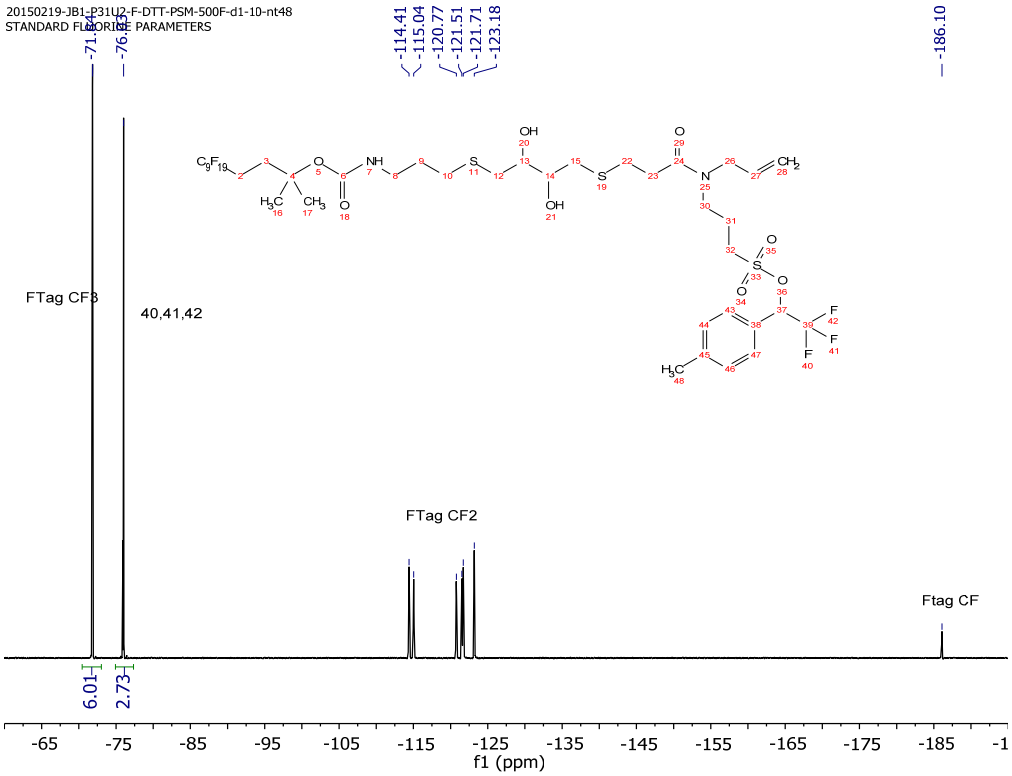


**Figure S24.** $^{19}$F NMR of "fluorous DTT-PSM" in d-chloroform. Note the PSM trifluoro peaks.

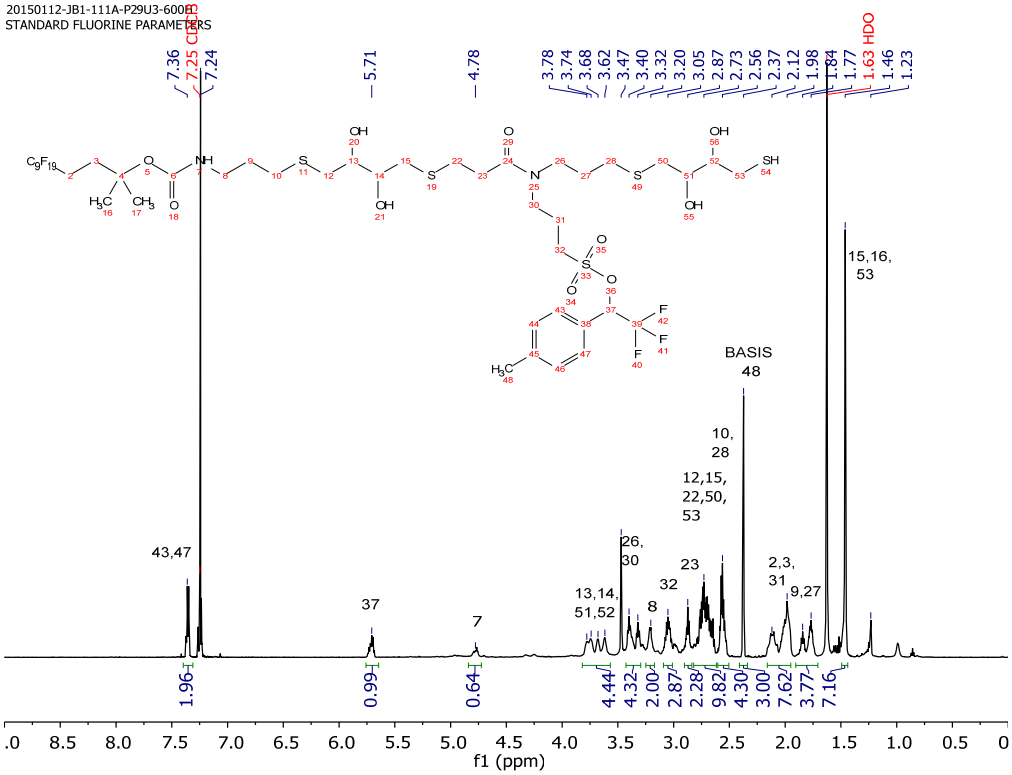


**Figure S25.** $^{1}$H NMR of "fluorous DTT-PSM-DTT" the fluorous purified product of the thiolene of the fluorous DTT-PSM and DTT in d-chloroform. Note the disappearance of the allyl peaks.

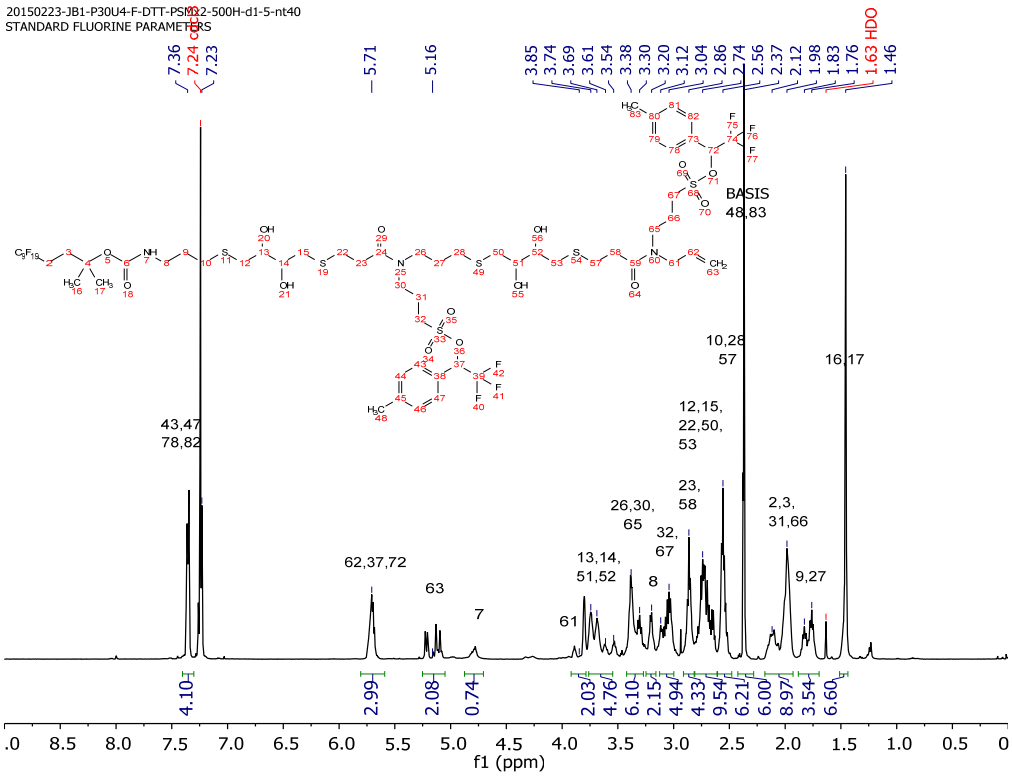


**Figure S26.** $^{1}$H NMR of "fluorous (DTT-PSM)$_2$" the fluorous purified product of the thiol-Michael of the fluorous DTT-PSM-DTT and the PSM in d-chloroform. Note the allyl peaks.

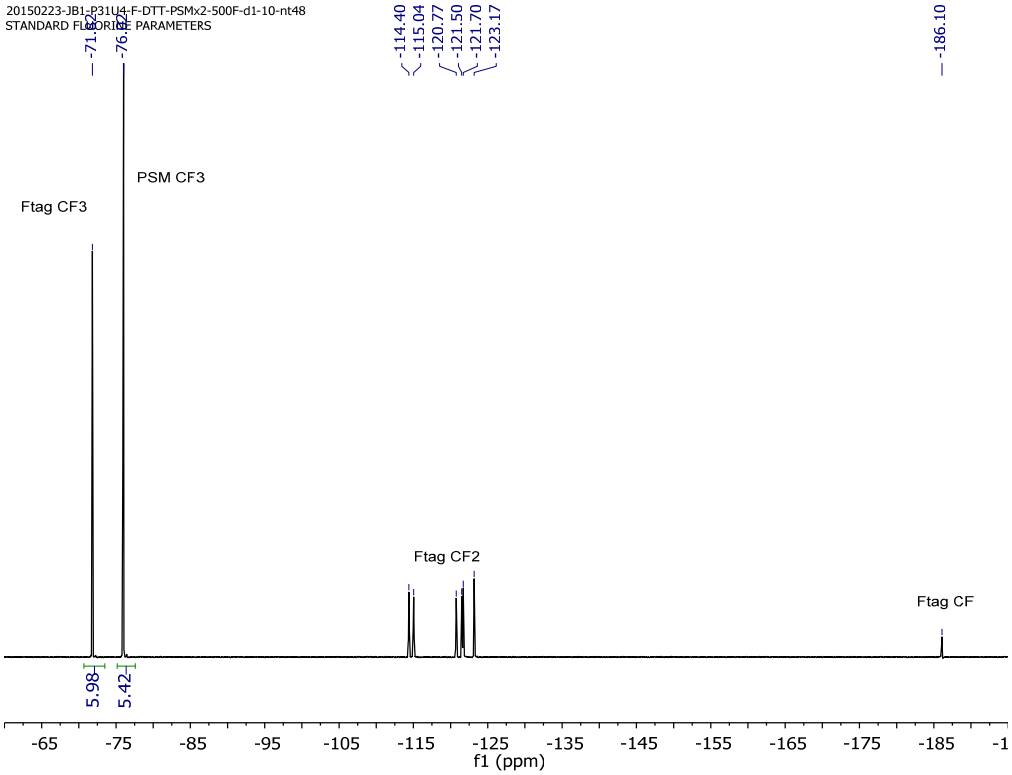


**Figure S27.** $^{19}$F NMR of "fluorous (DTT-PSM)$_2$" the fluorous purified product of the thiol-Michael of the fluorous DTT-PSM-DTT and the PSM in d-chloroform.

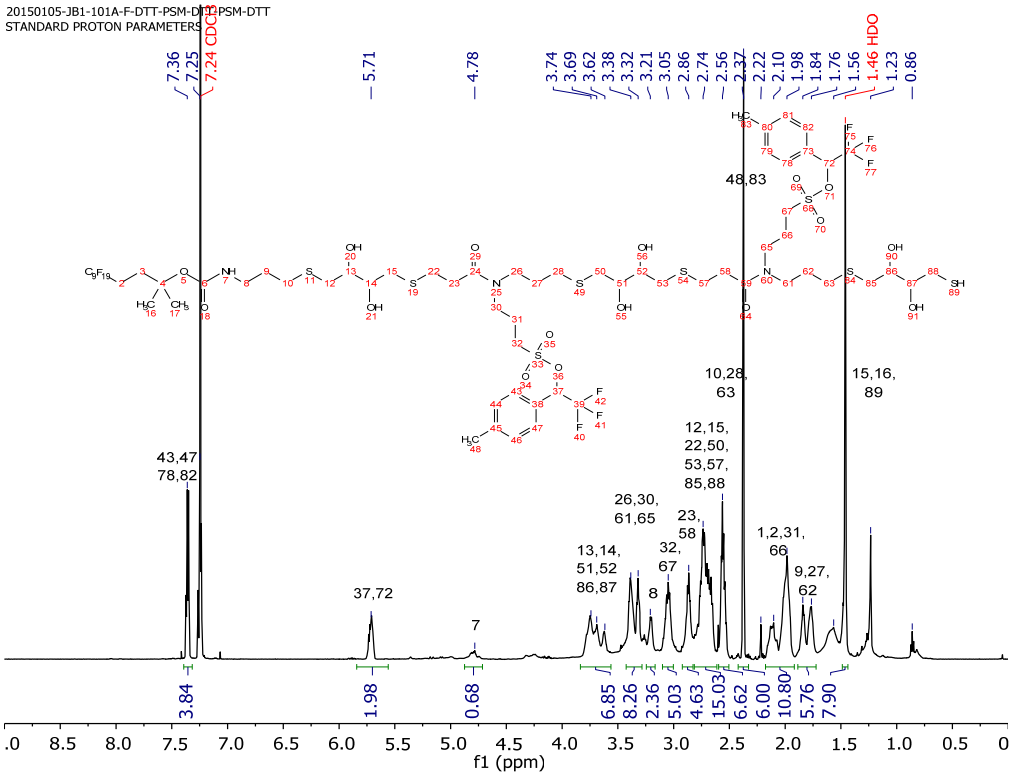


**Figure S28.** $^{1}$H NMR of "fluorous (DTT-PSM)$_2$-DTT" the fluorous purified product of the thiolene of the fluorous (DTT-PSM)$_2$ and DTT in d-chloroform. Note the disappearance of the allyl peaks.

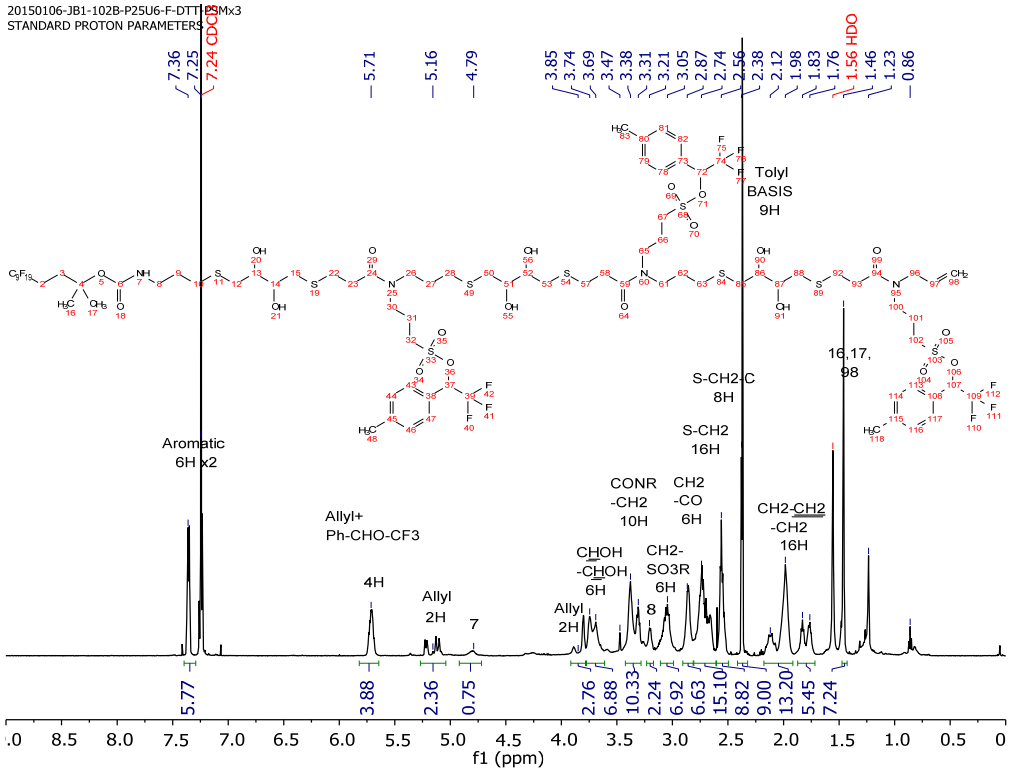


**Figure S29.** $^{1}$H NMR of "fluorous (DTT-PSM)$_3$" the fluorous purified product of the thiol-Michael of the fluorous (DTT-PSM)$_2$-DTT and the PSM in d-chloroform. Note the allyl peaks.

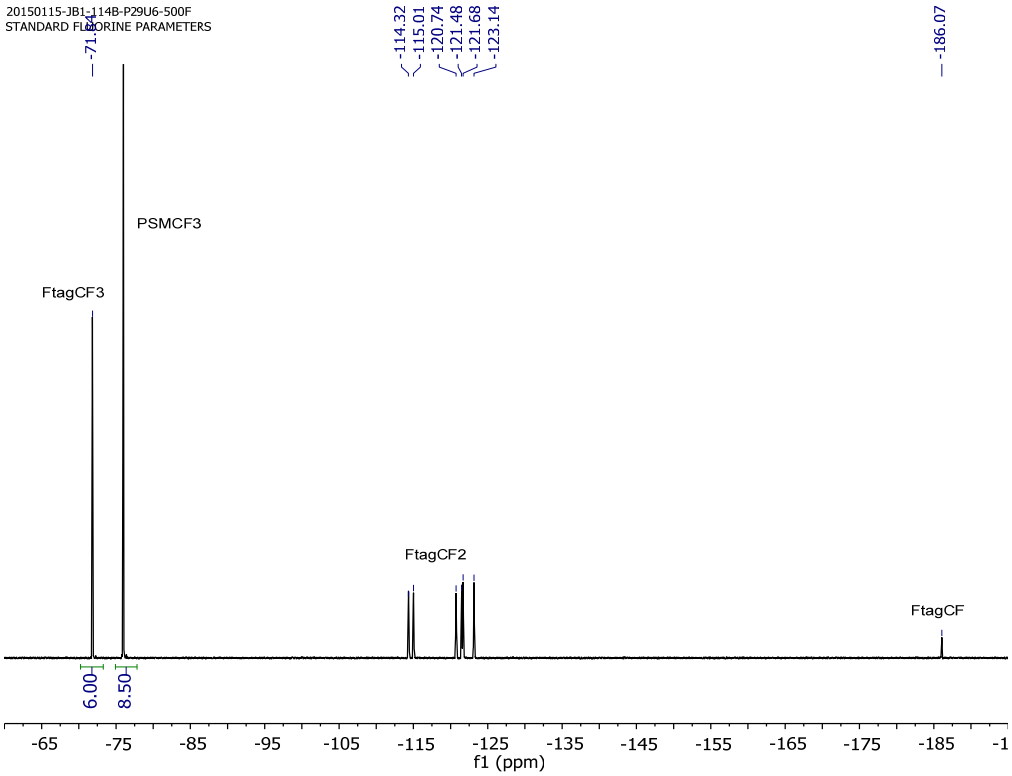


**Figure S30.** $^{19}F$ NMR of "fluorous (DTT-PSM)$_3$" the fluorous purified product of the thiol-Michael of the fluorous (DTT-PSM)$_2$-DTT and the PSM in d-chloroform.

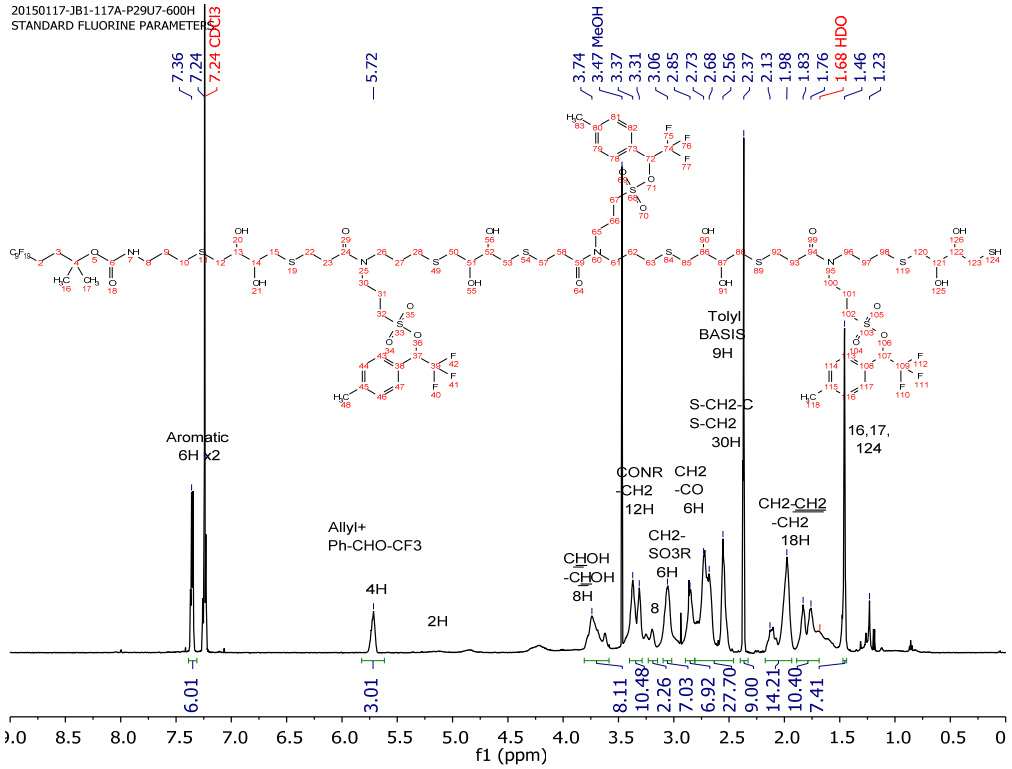


**Figure S31.** $^{1}H$ NMR of "fluorous (DTT-PSM)$_3$-DTT" the fluorous purified product of the thiolene of the fluorous (DTT-PSM)$_3$ and DTT in d-chloroform. Note the disappearance of the allyl peaks.

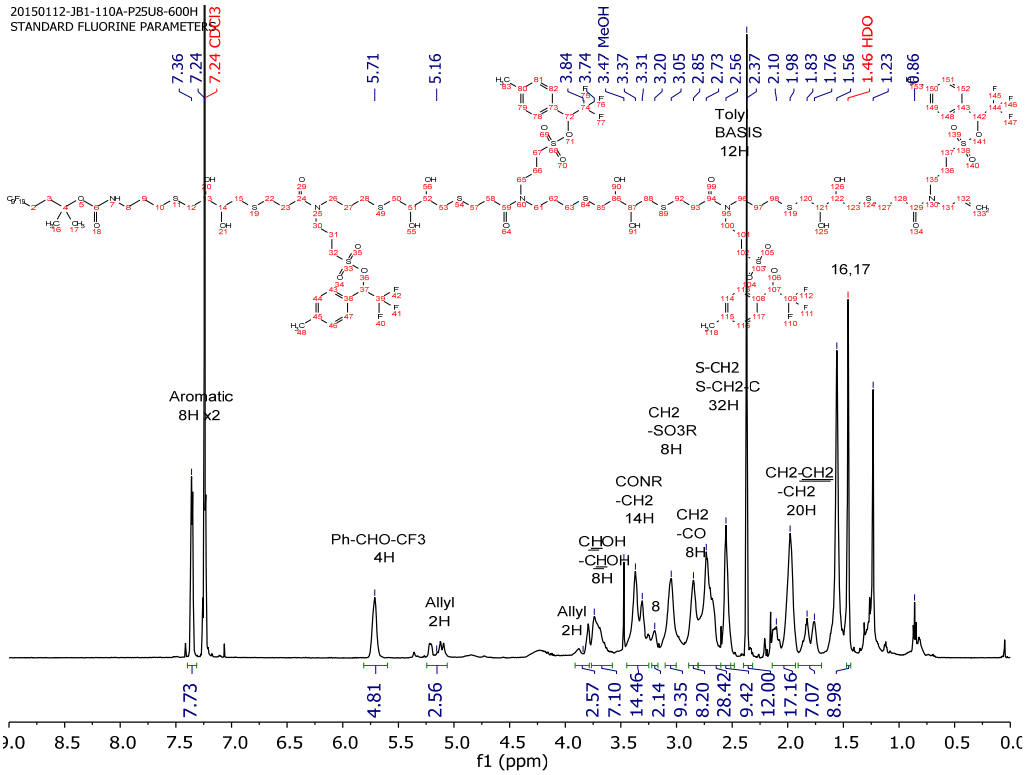


**Figure S32.** $^{1}$H NMR of "fluorous (DTT-PSM)$_4$" the fluorous purified product of the thiol-Michael of the fluorous (DTT-PSM)$_3$-DTT and the PSM in d-chloroform. Note the allyl peaks.

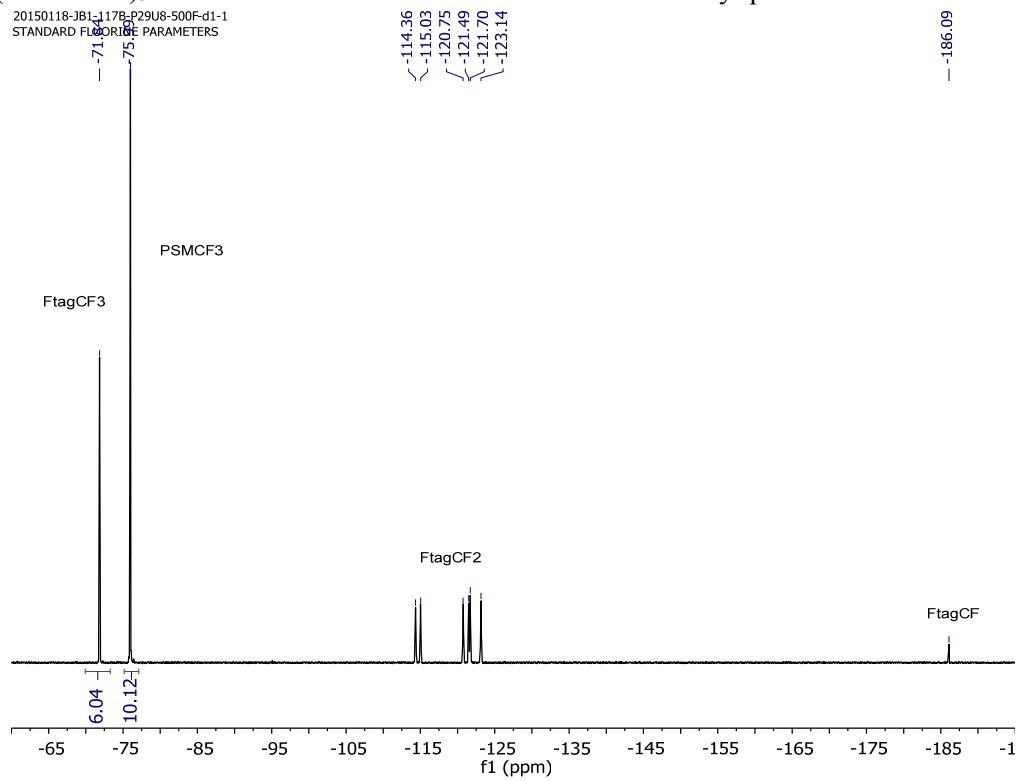


**Figure S33.** $^{19}$F NMR of "fluorous (DTT-PSM)$_4$" the fluorous purified product of the thiol-Michael of the fluorous (DTT-PSM)$_3$-DTT and the PSM in d-chloroform.

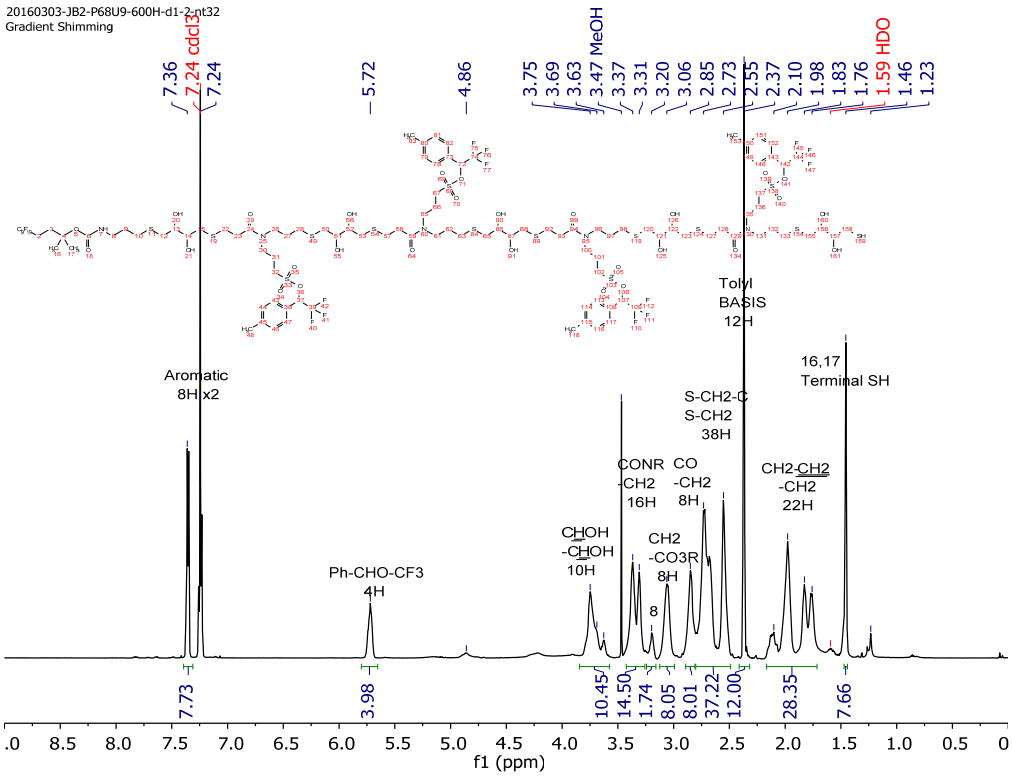


**Figure S34.** $^{1}$H NMR of "fluorous (DTT-PSM)$_4$-DTT" the fluorous purified product of the thiolene of the fluorous (DTT-PSM)$_4$ and DTT in d-chloroform. Note the disappearance of the allyl peaks.

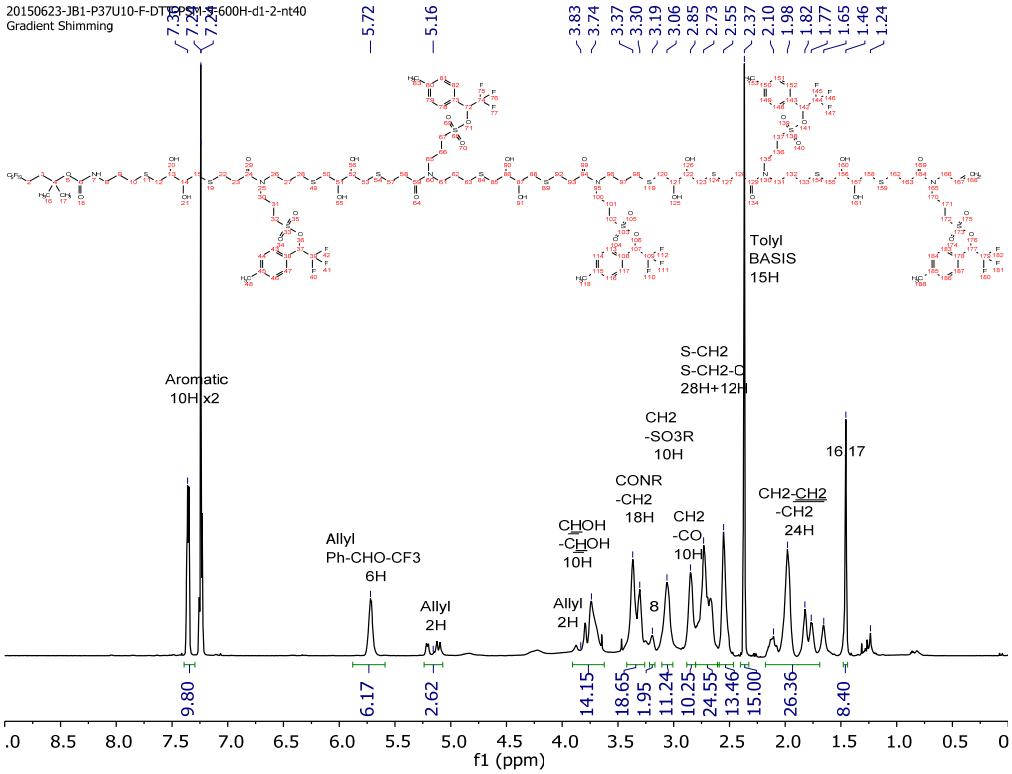


**Figure S35.** $^{1}$H NMR of "fluorous (DTT-PSM)$_5$" the fluorous purified product of the thiol-Michael of the fluorous (DTT-PSM)$_4$-DTT and the PSM in d-chloroform. Note the allyl peaks.

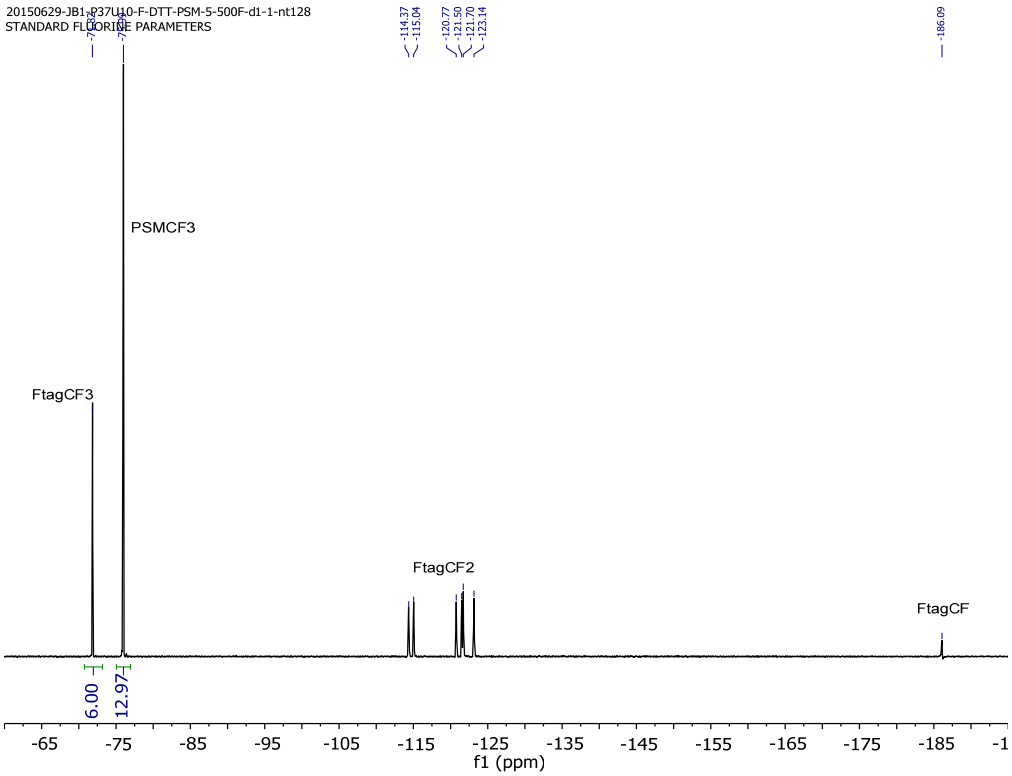


**Figure S36.** $^{19}F$ NMR of "fluorous (DTT-PSM)$_5$" the fluorous purified product of the thiol-Michael of the fluorous (DTT-PSM)$_4$-DTT and the PSM in d-chloroform.

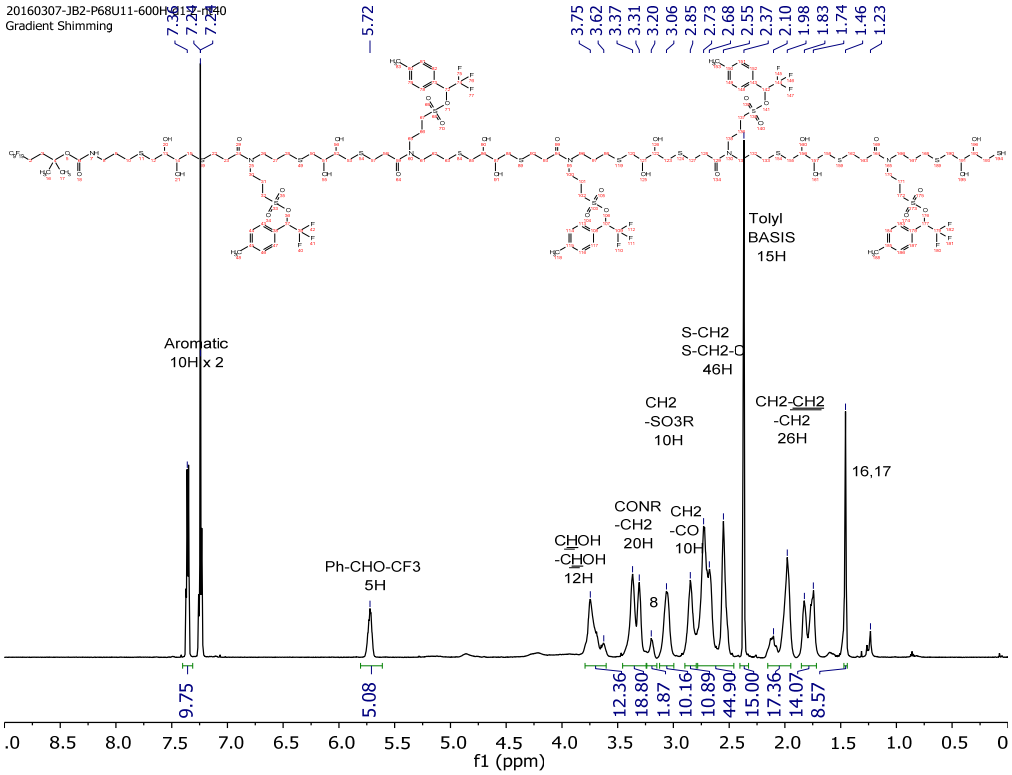


**Figure S37.** $^{1}H$ NMR of "fluorous (DTT-PSM)$_5$-DTT" the fluorous purified product of the thiolene of the fluorous (DTT-PSM)$_5$ and DTT in d-chloroform. Note the disappearance of the allyl peaks.

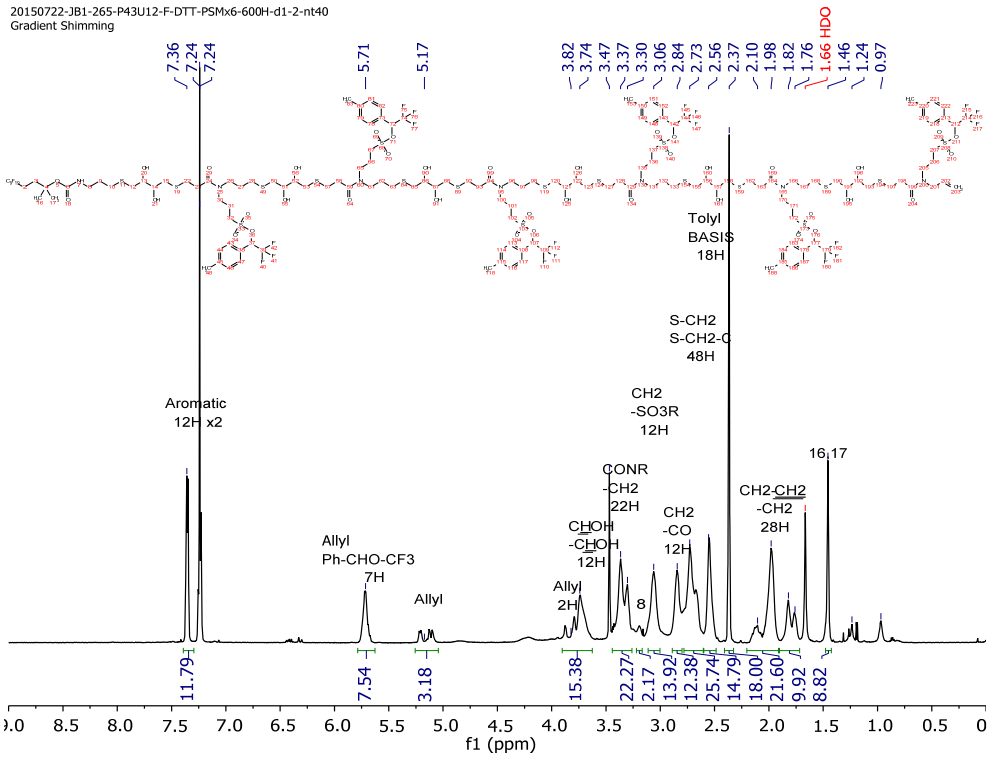


**Figure S38.** $^{1}$H NMR of "fluorous (DTT-PSM)$_6$" the fluorous purified product of the thiol-Michael of the fluorous (DTT-PSM)$_5$-DTT and the PSM in d-chloroform. Note the appearance of the allyl peaks and small acrylamide peaks indicating a small amount of PSM remains after purification.

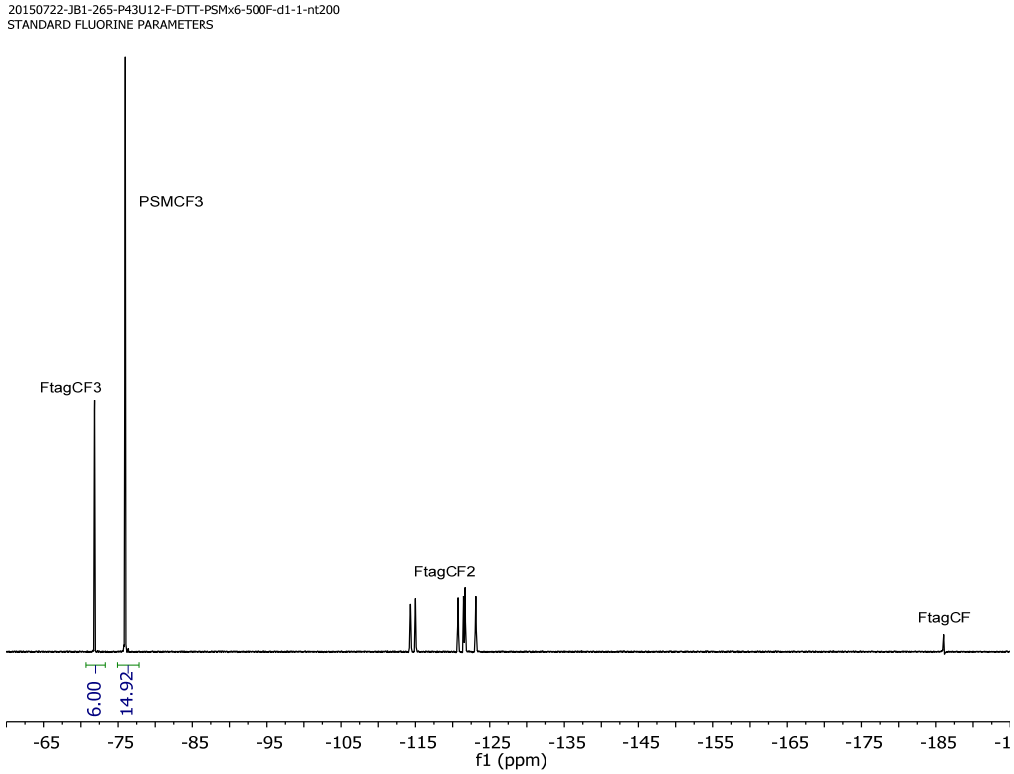


**Figure S39.** $^{19}$F NMR of "fluorous (DTT-PSM)$_6$" the fluorous purified product of the thiol-Michael of the fluorous (DTT-PSM)$_6$-DTT and the PSM in d-chloroform.

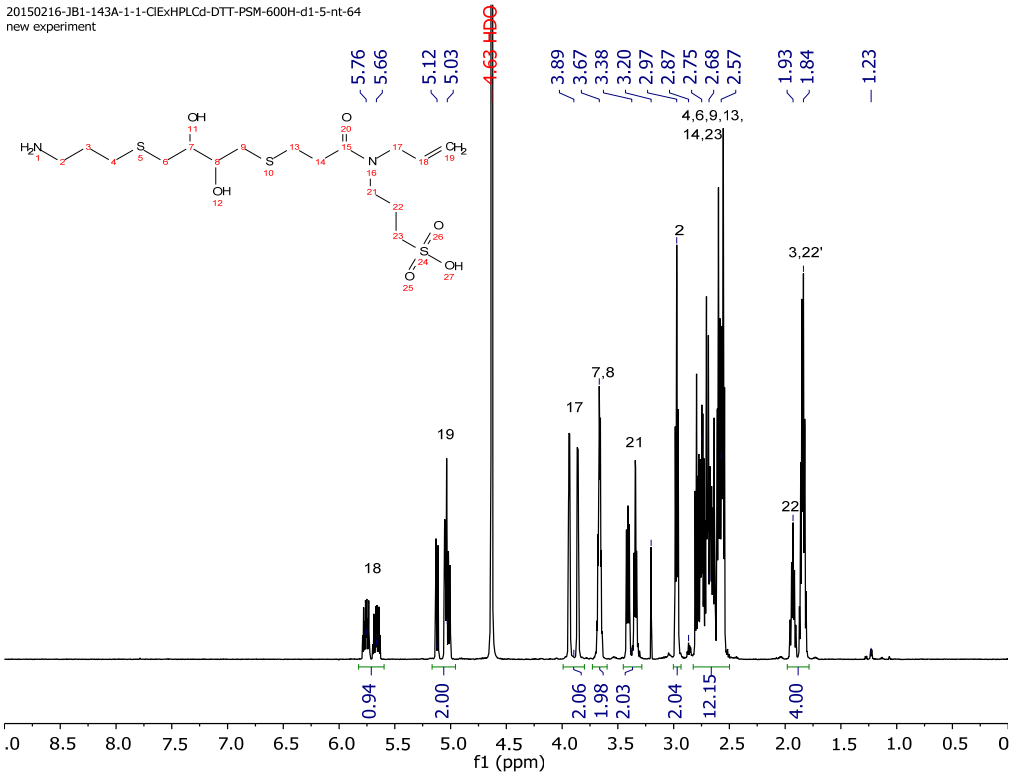


**Figure S40.** $^{1}$H NMR of the "2mer," the $NH_2$-(DTT-PSM)$_1$ product in deuterated water obtained from the TFA-cleavage of the fluorous-DTT-PSM after HPLC purification.

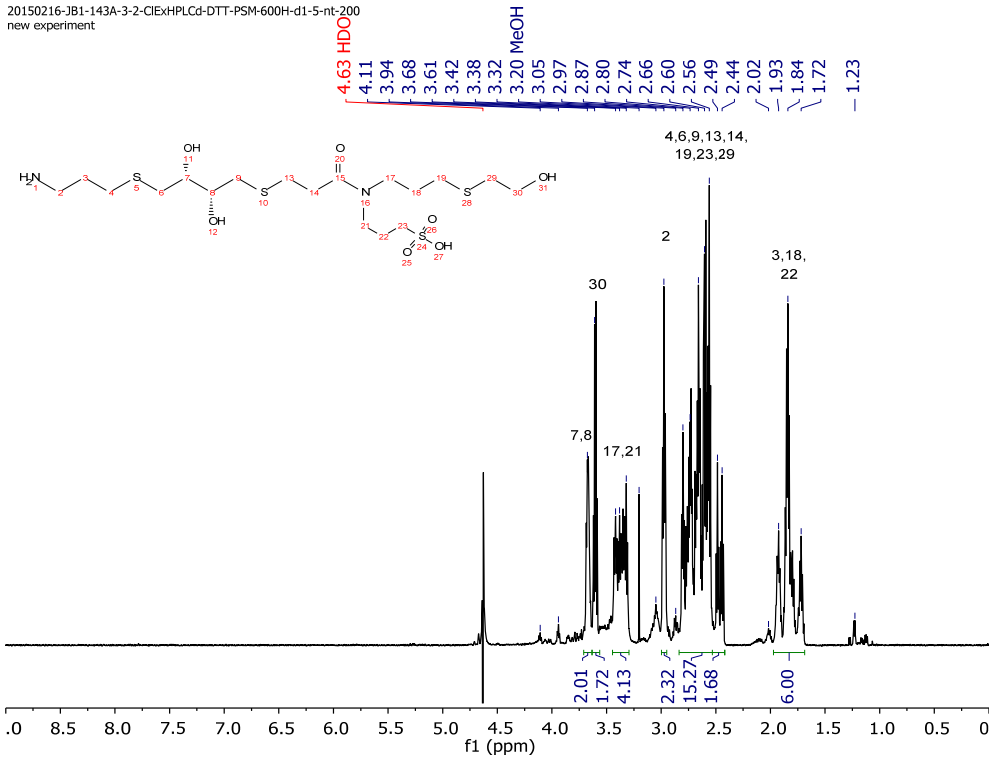


**Figure S41.** $^{1}$H NMR of a "3mer" in deuterated water with solvent suppression on the HDO peak, where the fluorous-DTT-PSM was reacted with 2-mercaptoethanol (BME), fluorous and HPLC purified. This molecule was prepared only to understand other oligomer assignments.

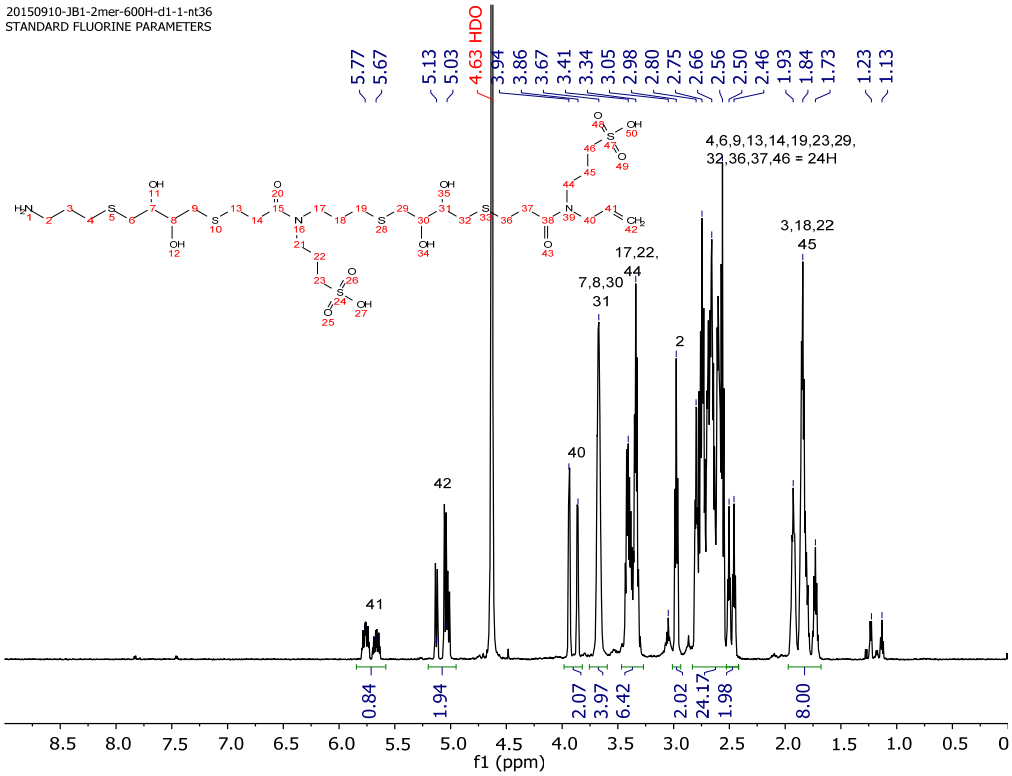


**Figure S42.** $^{1}$H NMR of the "4mer," the $NH_2$-(DTT-PSM)$_2$ product in deuterated water obtained from the TFA-cleavage of the fluorous-(DTT-PSM)$_2$ after HPLC purification.

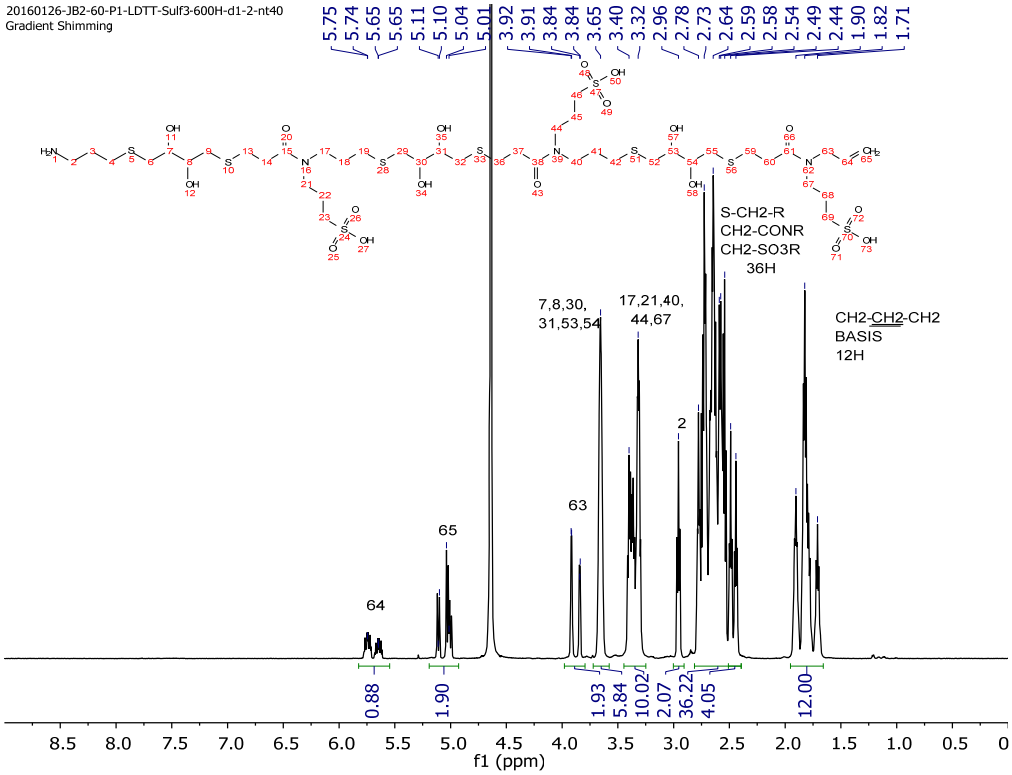


**Figure S43.** $^{1}$H NMR of the "6mer," the $NH_2$-(DTT-PSM)$_3$ product in deuterated water obtained from the TFA-cleavage of the fluorous-(DTT-PSM)$_3$ after HPLC purification.

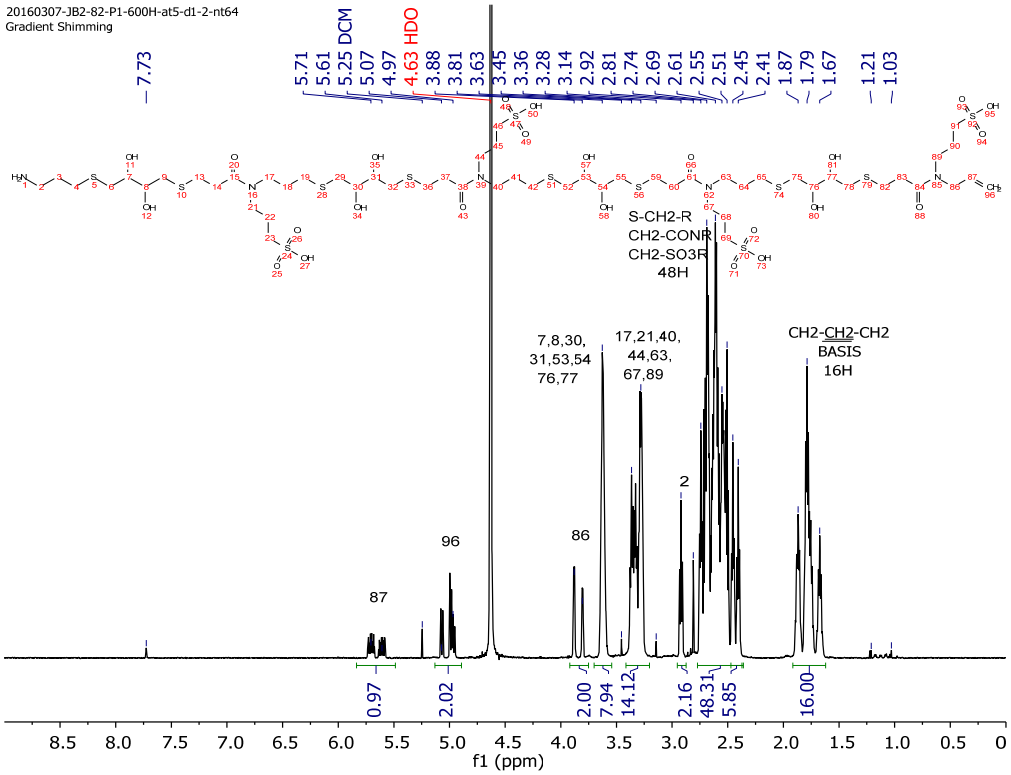


**Figure S44.** $^{1}$H NMR of the "8mer," the $NH_2$-(DTT-PSM)$_4$ product in deuterated water obtained from the TFA-cleavage of the fluorous-(DTT-PSM)$_4$ after HPLC purification.

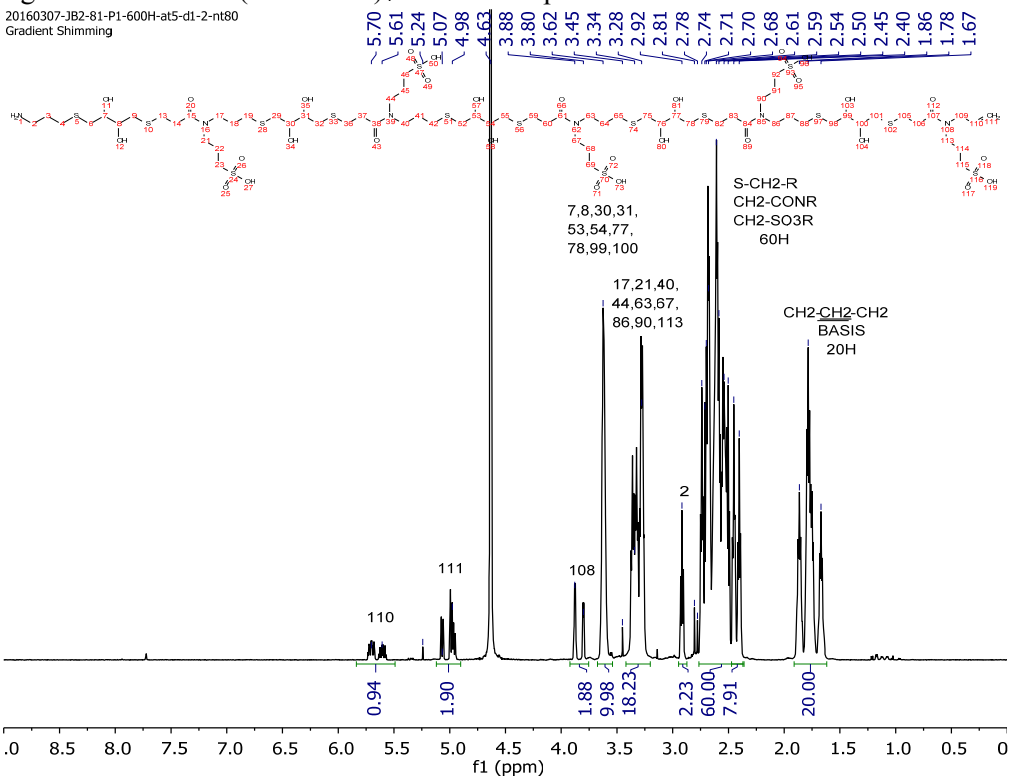


**Figure S45.** $^{1}$H NMR of the "10mer," the $NH_2$-(DTT-PSM)$_5$ product in deuterated water obtained from the TFA-cleavage of the fluorous-(DTT-PSM)$_5$ after HPLC purification.

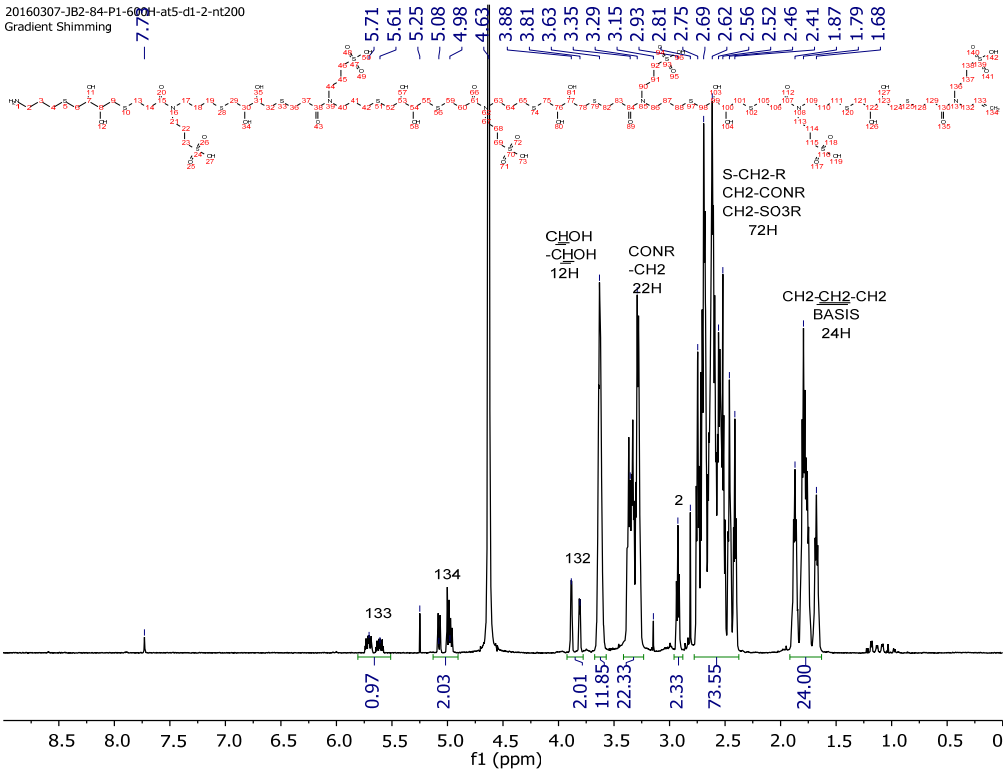


**Figure S46.** $^{1}$H NMR of the "12mer," the $NH_2$-(DTT-PSM)$_6$ product in deuterated water obtained from the TFA-cleavage of the fluorous-(DTT-PSM)$_6$ after HPLC purification.

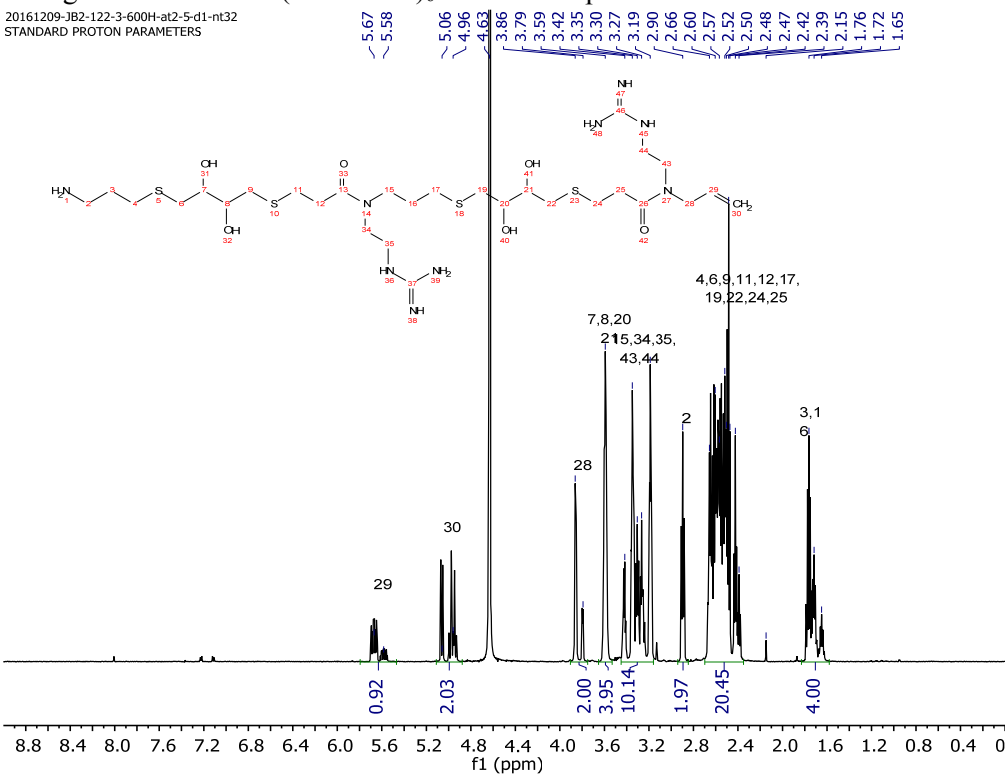


**Figure S47.** $^{1}$H NMR of the "4mer" of the $NH_2$-(DTT-G)$_2$ product in deuterated water obtained from the TFA-cleavage of the fluorous-(DTT-G)$_2$ after HPLC purification.

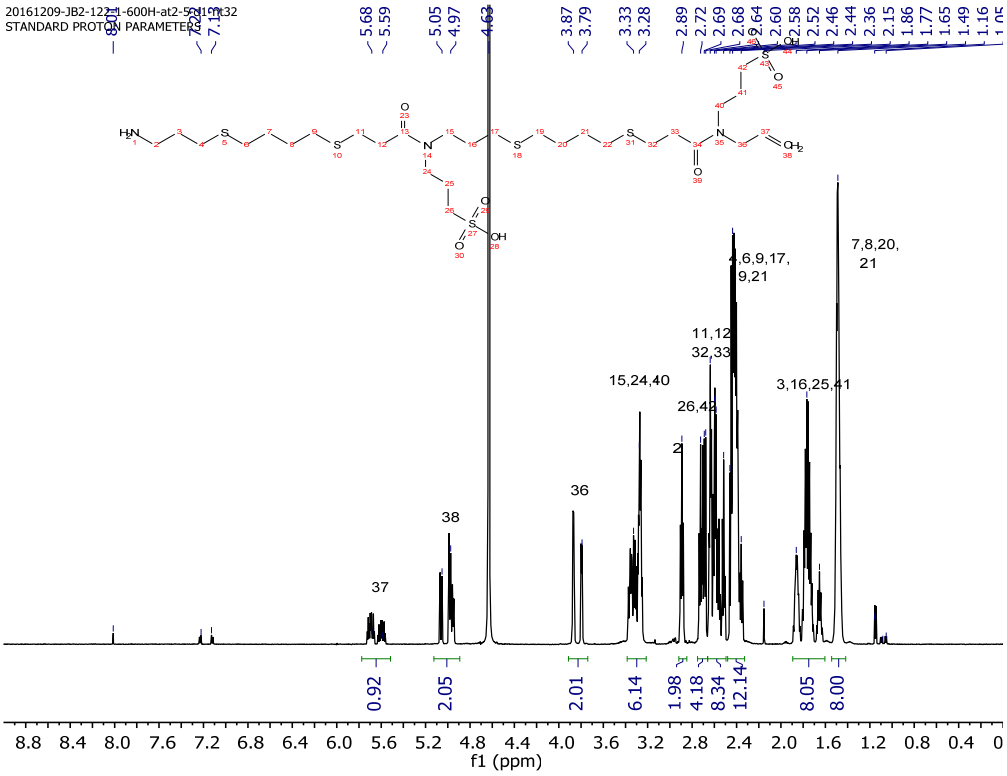


**Figure S48.** $^{1}$H NMR of the "4mer" of the $NH_2$-(BDT-Sulf)$_2$ product in deuterated water obtained from the TFA-cleavage of the fluorous-(BDT-Sulf)$_2$ after HPLC purification.

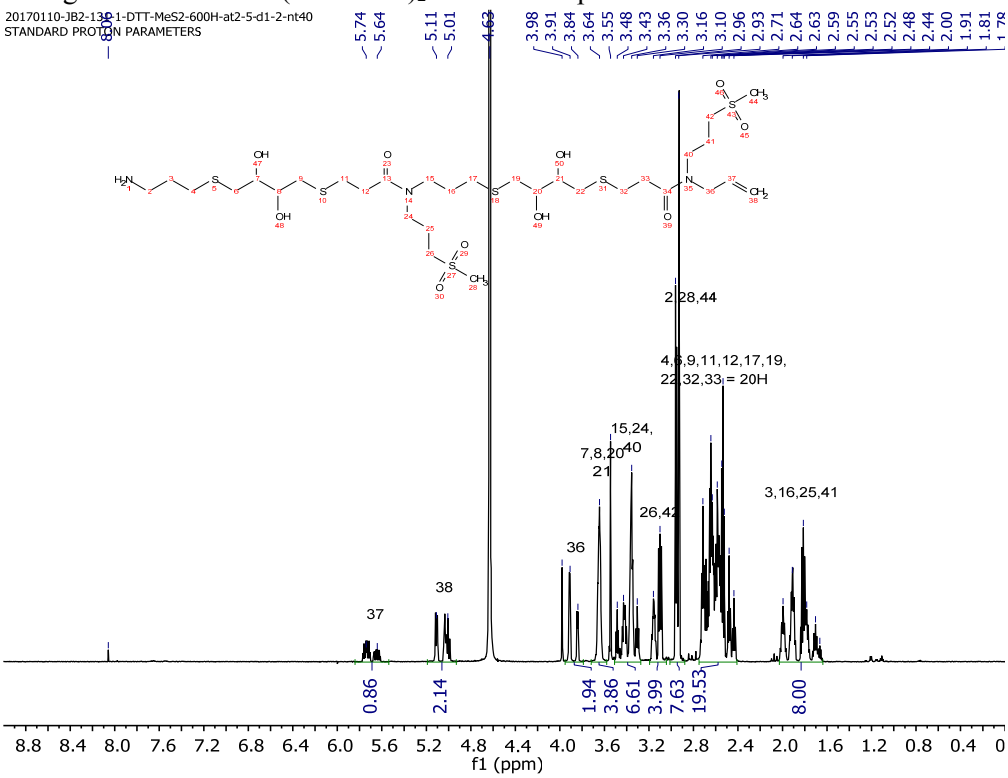


**Figure S49.** $^{1}$H NMR of the "4mer" of the $NH_2$-(DTT-MeS)$_2$ product in deuterated water obtained from the TFA-cleavage of the fluorous-(DTT-MeS)$_2$ after HPLC purification.

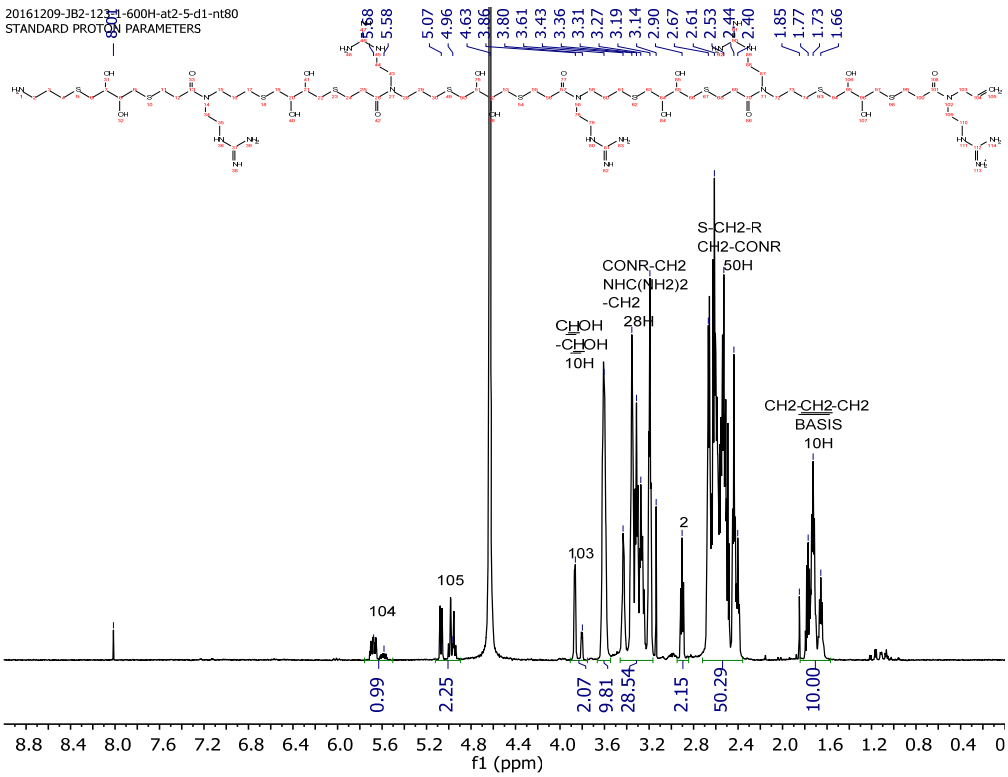


**Figure S50.** $^{1}$H NMR of the "10mer" of the $NH_2$-(DTT-G)$_5$ product in deuterated water obtained from the TFA-cleavage of the fluorous-(DTT-G)$_5$ after HPLC purification.

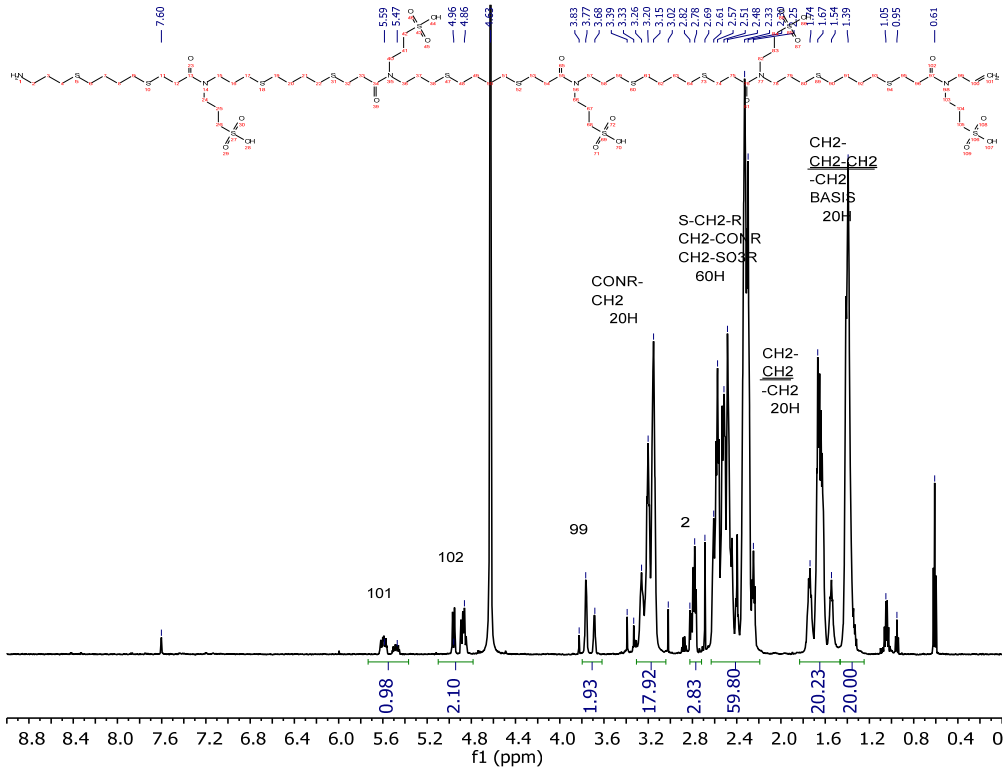


**Figure S51.** $^{1}$H NMR of the "10mer" of the $NH_2$-(BDT-Sulf)$_5$ product in deuterated water obtained from the TFA-cleavage of the fluorous-(BDT-Sulf)$_5$ after HPLC purification.

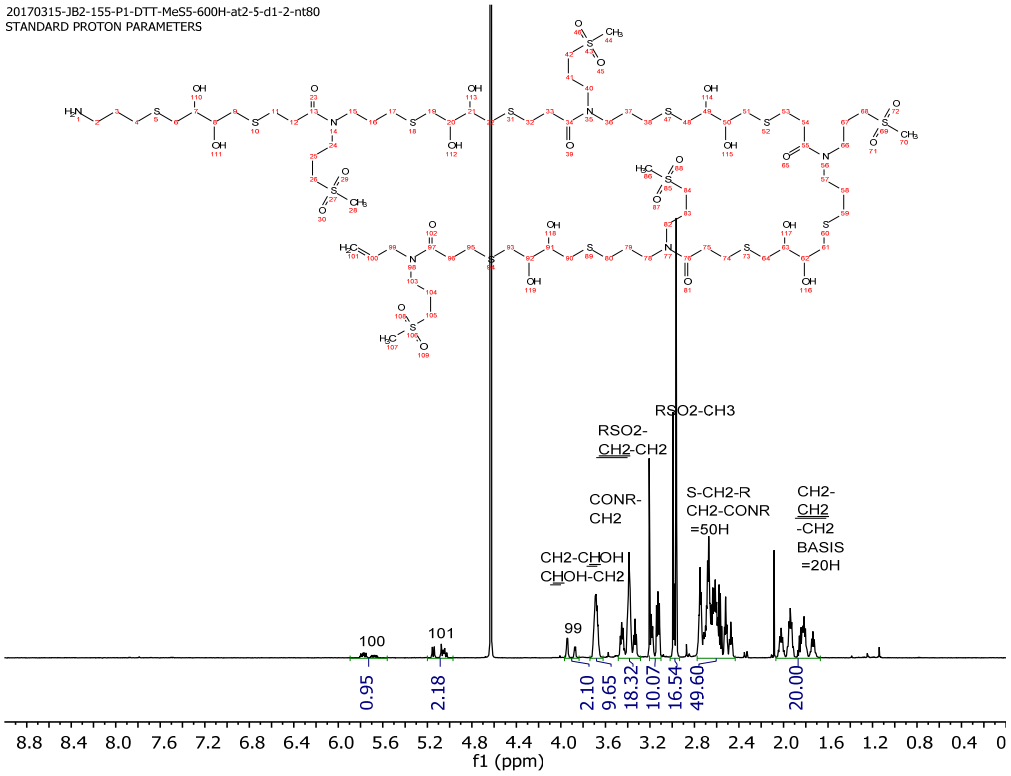


**Figure S52.** $^{1}$H NMR of the "10mer" of the $NH_2$-$(DTT\text{-}MeS)_5$ product in deuterated water obtained from the TFA-cleavage of the fluorous-$(DTT\text{-}MeS)_5$ after HPLC purification.

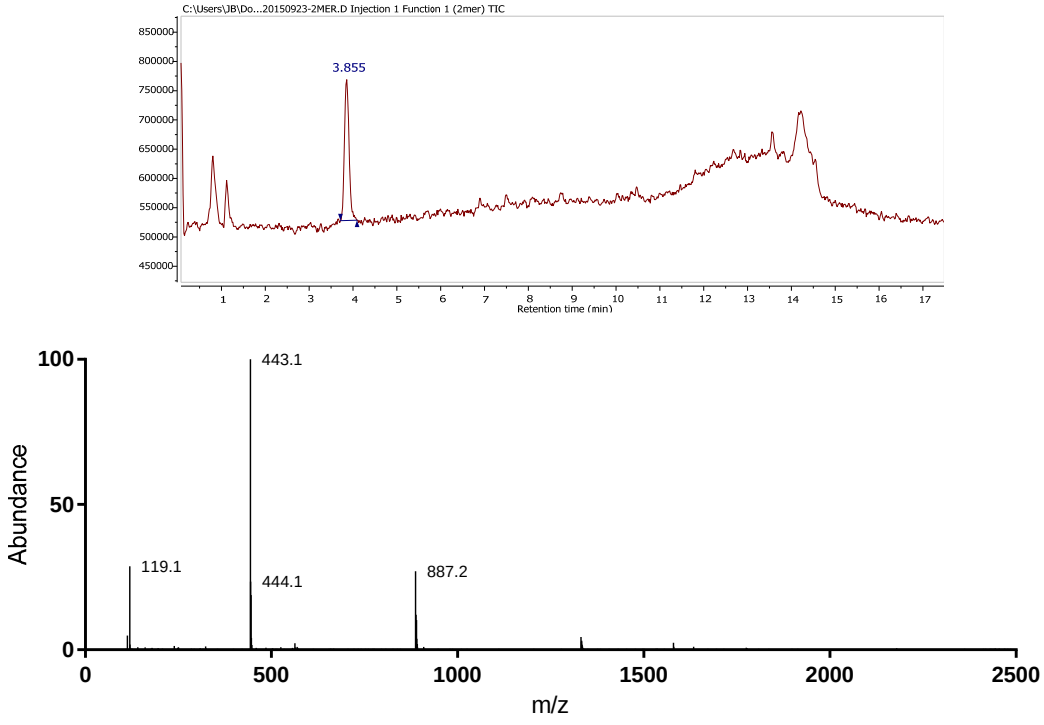


**Figure S53.** Negative mode LCMS of the $(DTT\text{-}Sulf)_1$ with the TIC (top) and the corresponding mass spectra (bottom). Parent mass: 444.14; $[M\text{-}H]^{-1}$ Expected: 443.13 Obs. 443.1; $[2M\text{-}H]^{-1}$ Expected: 887.27 Obs. 887.2.

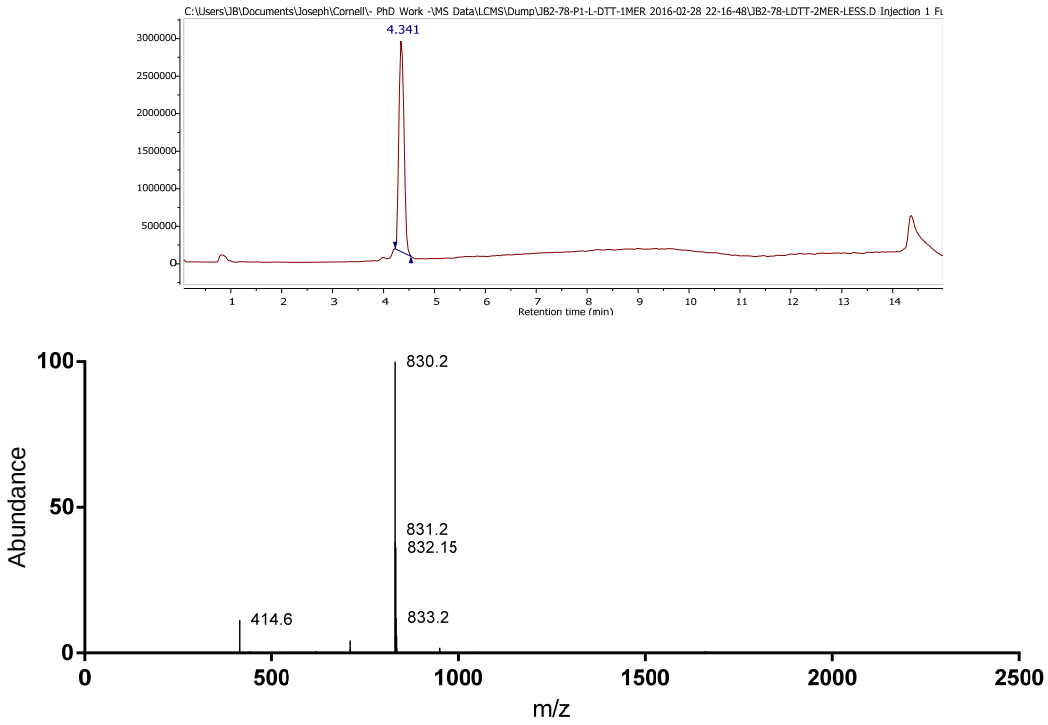


**Figure S54.** Negative mode LCMS of the $(DTT\text{-}Sulf)_2$ with the TIC (top) and the corresponding mass spectra (bottom). Parent mass: 831.23; $[M\text{-}H]^{-1}$ Expected: 830.22 Obs. 830.2; $[M\text{-}2H]^{-2}$ Expected: 414.61 Obs. 414.6.

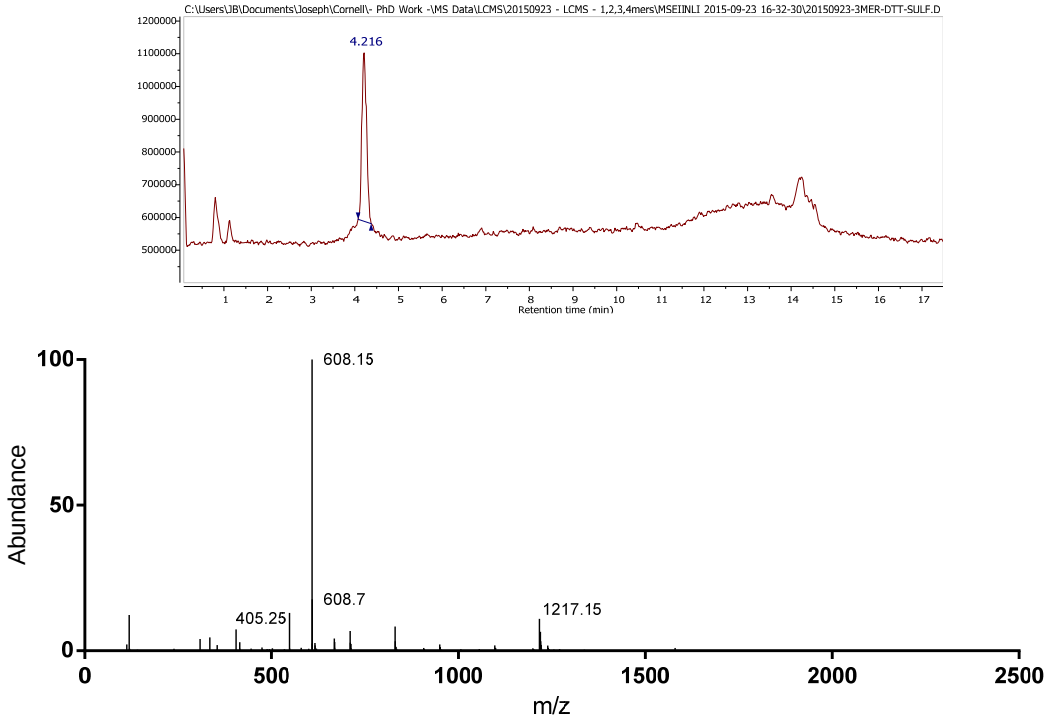


**Figure S55.** Negative mode LCMS of the $(DTT\text{-}Sulf)_3$ with the TIC (top) and the corresponding mass spectra (bottom). Parent mass: 1218.31; $[M\text{-}H]^{-1}$ Expected: 1217.30 Obs. 1217.15; $[M\text{-}2H]^{-2}$ Expected: 608.15 Obs. 608.15; $[M\text{-}3H]^{-3}$ Expected: 405.10 Obs. 405.25.

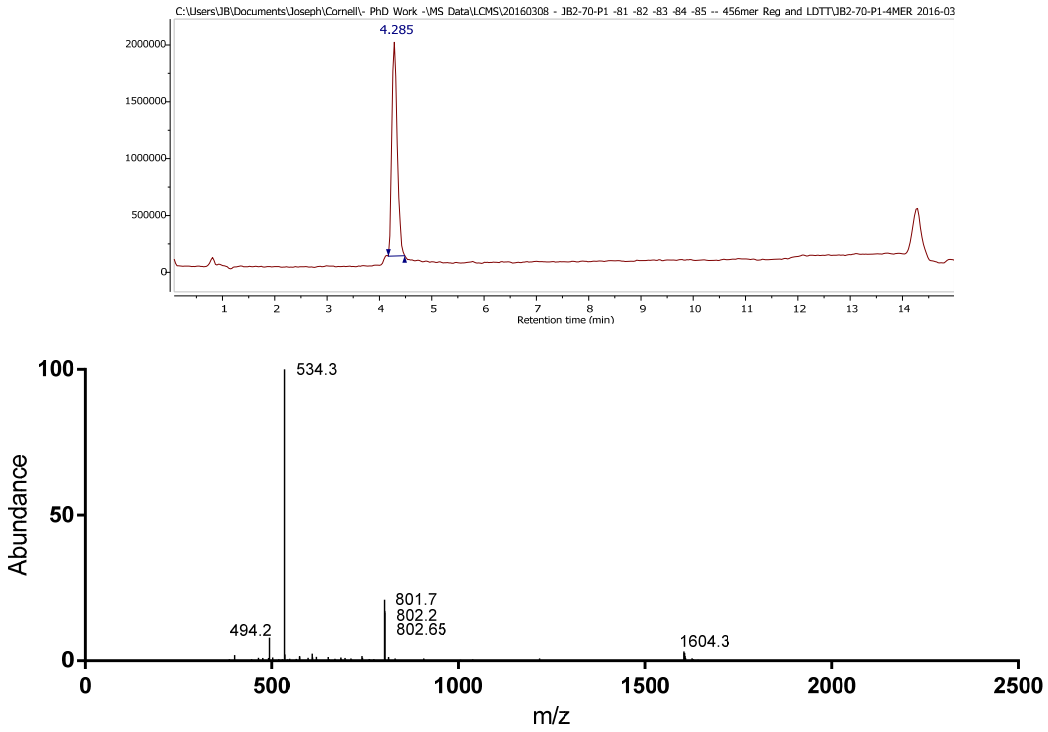


**Figure S56.** Negative mode LCMS of the $(DTT\text{-}Sulf)_4$ with the TIC (top) and the corresponding mass spectra (bottom). Parent mass: 1605.40; $[M\text{-}H]^{-1}$ Expected: 1604.39 Obs. 1604.3; $[M\text{-}2H]^{-2}$ Expected: 801.69 Obs. 801.7; $[M\text{-}3H]^{-3}$ Expected: 534.13 Obs. 534.3.

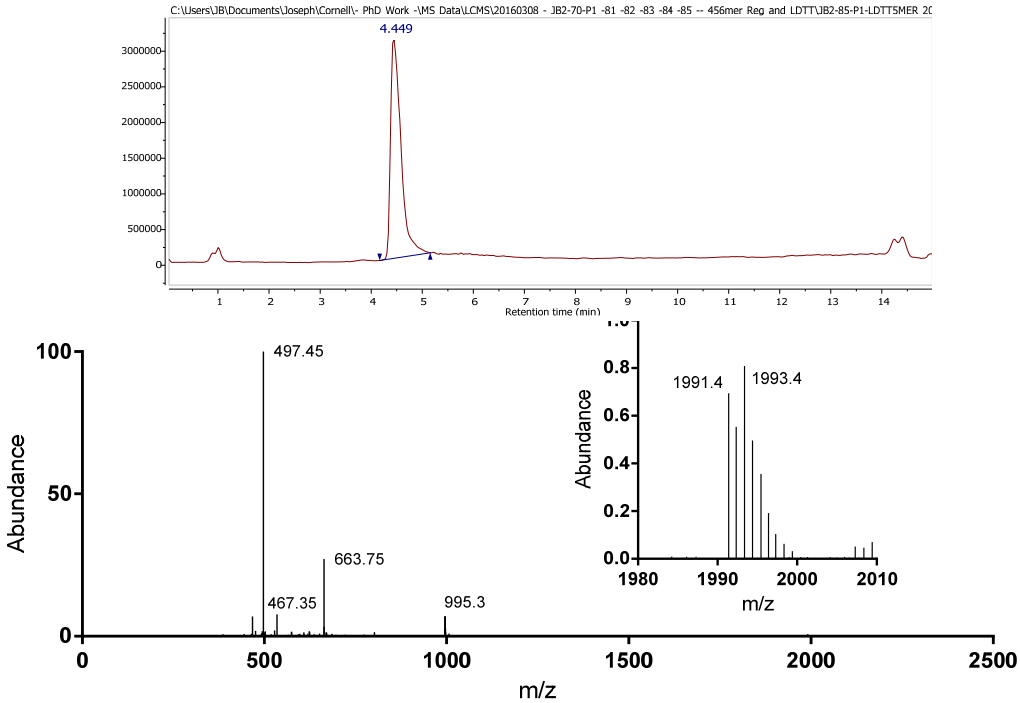


**Figure S57.** Negative mode LCMS of the $(DTT\text{-}Sulf)_5$ with the TIC (top) and the corresponding mass spectra (bottom). Parent mass: 1992.48; $[M\text{-}H]^{-1}$ Expected: 1991.47 Obs. 1991.4 (inset); $[M\text{-}2H]^{-2}$ Expected: 995.23 Obs. 995.3; $[M\text{-}3H]^{-3}$ Expected: 663.15 Obs. 663.75; $[M\text{-}4H]^{-4}$ Expected: 497.11 Obs. 497.45.

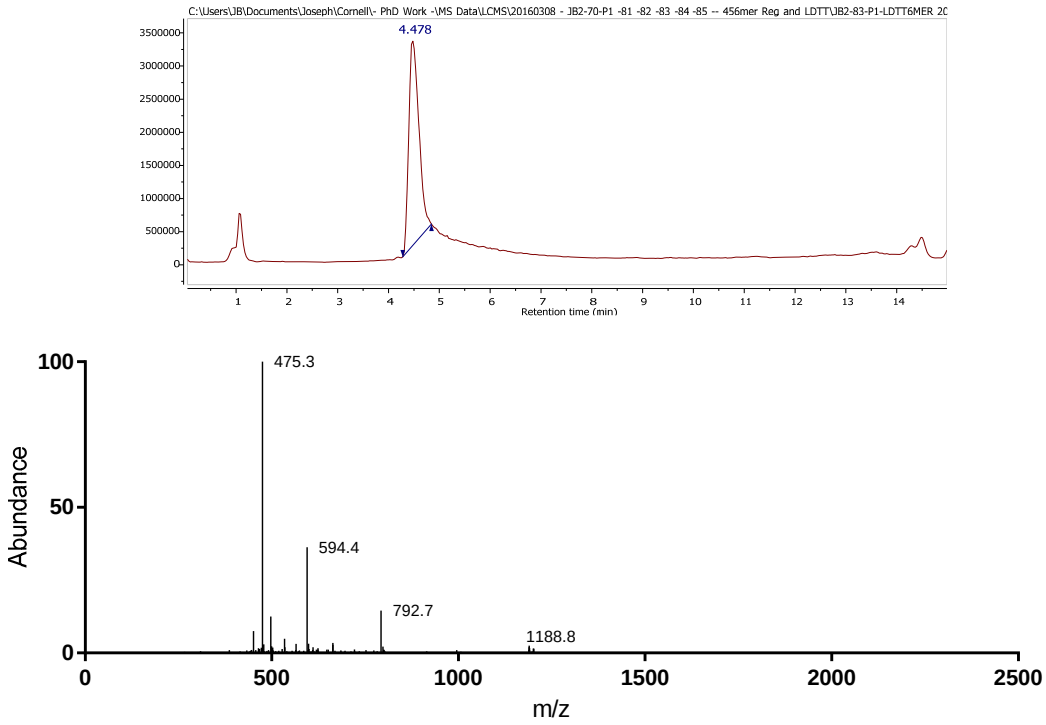


**Figure S58.** Negative mode LCMS of the $(DTT\text{-}Sulf)_6$ with the TIC (top) and the corresponding mass spectra (bottom). Parent mass: 2379.56; $[M\text{-}2H]^{-2}$ Expected: 1188.77 Obs. 1188.8; $[M\text{-}3H]^{-3}$ Expected: 792.18 Obs. 792.7; $[M\text{-}4H]^{-4}$ Expected: 474.90 Obs. 475.3.

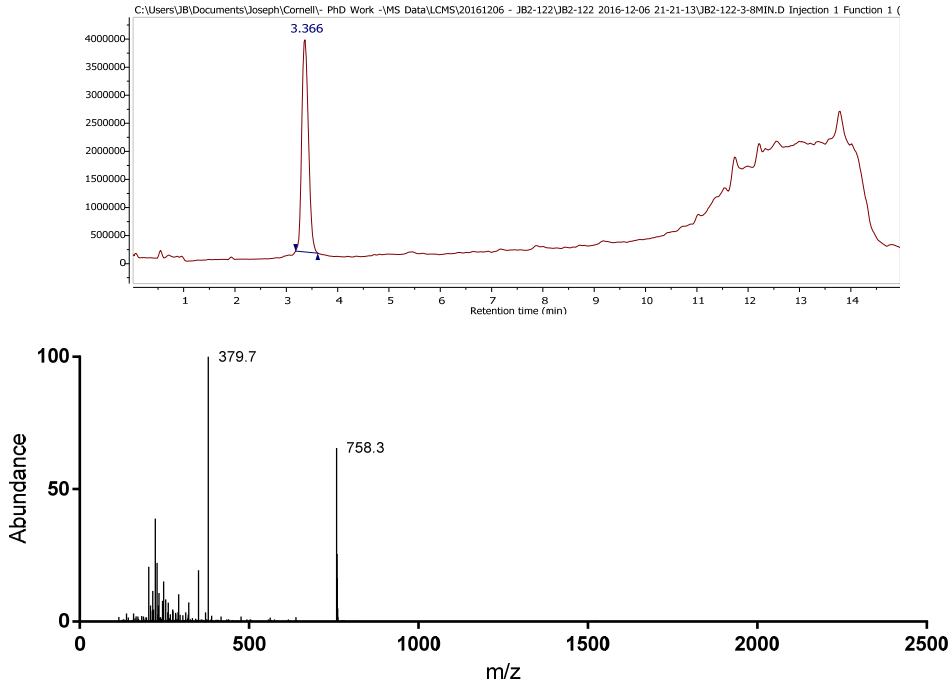


**Figure S59.** Positive mode LCMS of the $NH_2\text{-}(DTT\text{-}G)_2$ with the TIC (top) and the corresponding mass spectra (bottom). Parent mass: 757.35; $[M+H]^{+1}$ Expected: 758.35 Obs. 758.3; $[M+2H]^{+2}$ Expected: 379.68 Obs. 379.7.

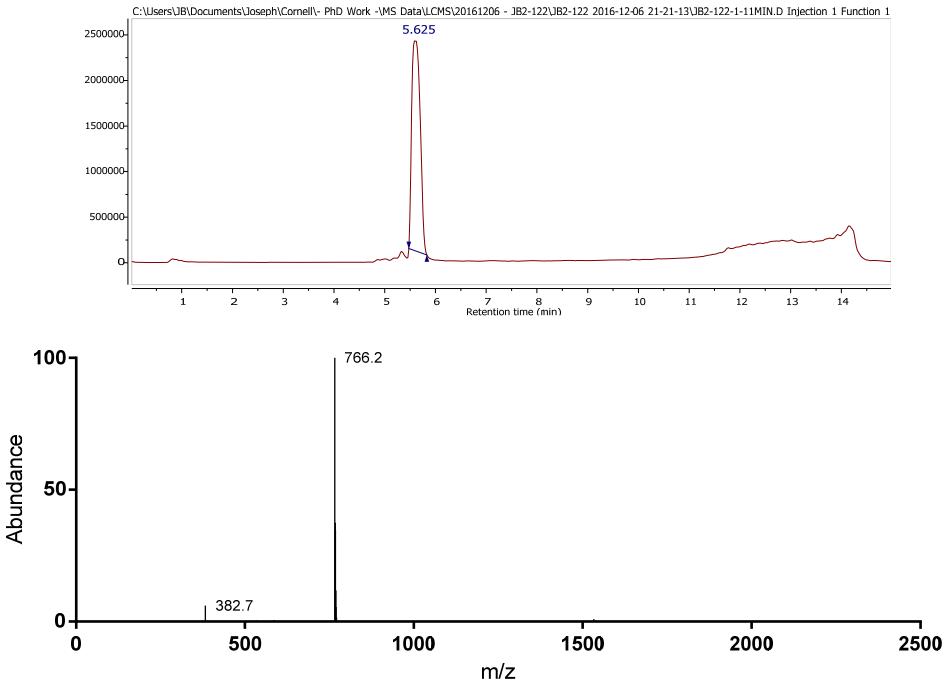


**Figure S60.** Negative mode LCMS of the $NH_2$-(BDT-Sulf)$_2$ with the TIC (top) and the corresponding mass spectra (bottom). Parent mass: 767.25; $[M-H]^{-1}$ Expected: 766.24 Obs. 762.2; $[M-2H]^{-2}$ Expected: 382.62 Obs. 382.7.

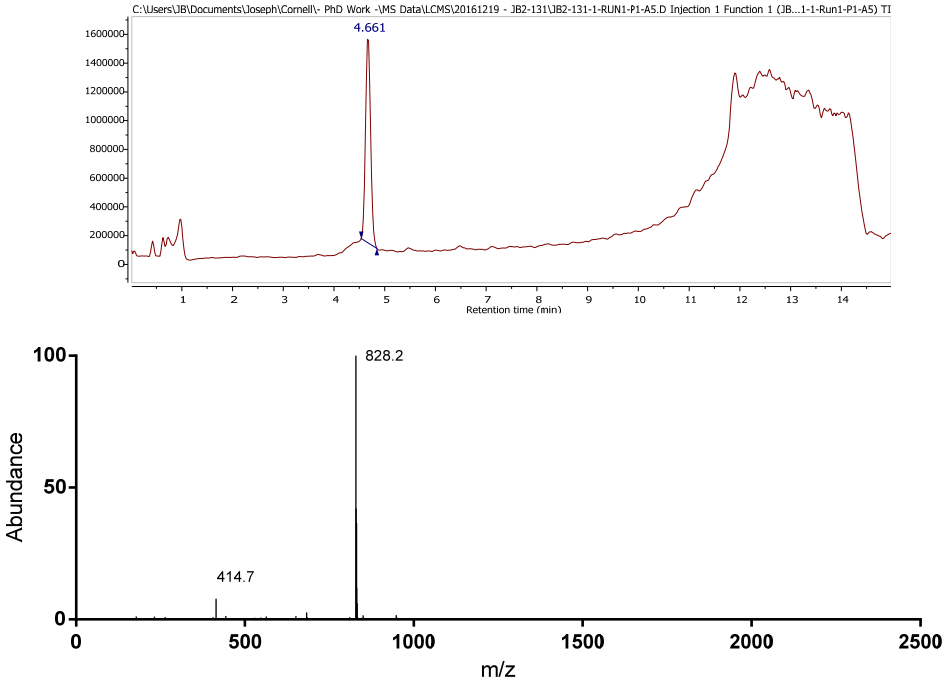


**Figure S61.** Positive mode LCMS of the $NH_2$-(DTT-MeS)$_2$ with the TIC (top) and the corresponding mass spectra (bottom). Parent mass: 827.27; $[M+H]^{+1}$ Expected: 828.28 Obs. 828.2; $[M+2H]^{+2}$ Expected: 414.64 Obs. 414.7.

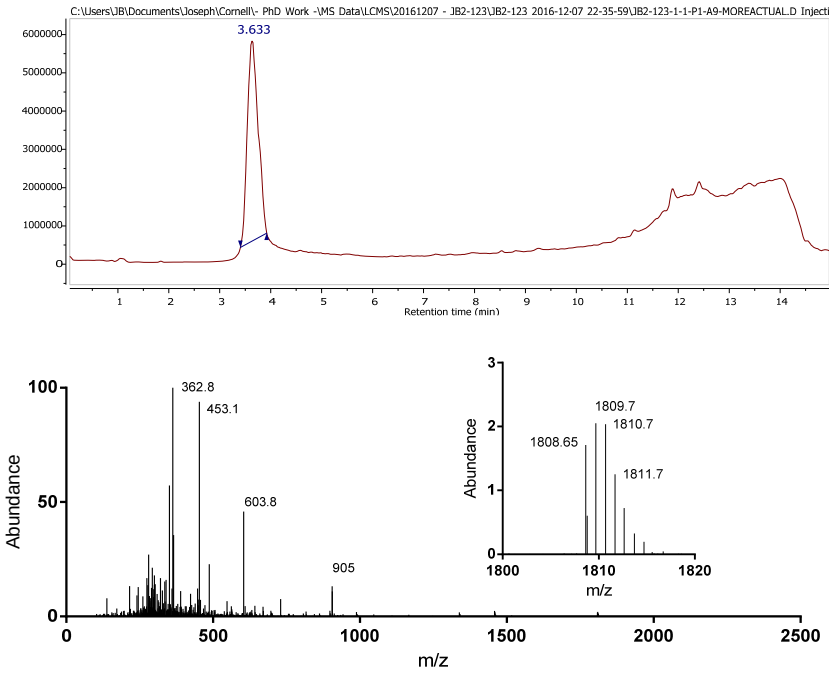


**Figure S62.** Positive mode LCMS of the $NH_2$-(DTT-G)$_5$ with the TIC (top) and the corresponding mass spectra (bottom). Parent mass: 1807.78; $[M+H]^{+1}$ Expected: 1808.79 Obs. 1808.65; $[M+2H]^{+2}$ Expected: 904.90 Obs. 905.0; $[M+3H]^{+3}$ Expected: 603.60 Obs. 603.8; $[M+4H]^{+4}$ Expected: 452.95 Obs. 453.1; $[M+5H]^{+5}$ Expected: 362.56 Obs. 362.8.

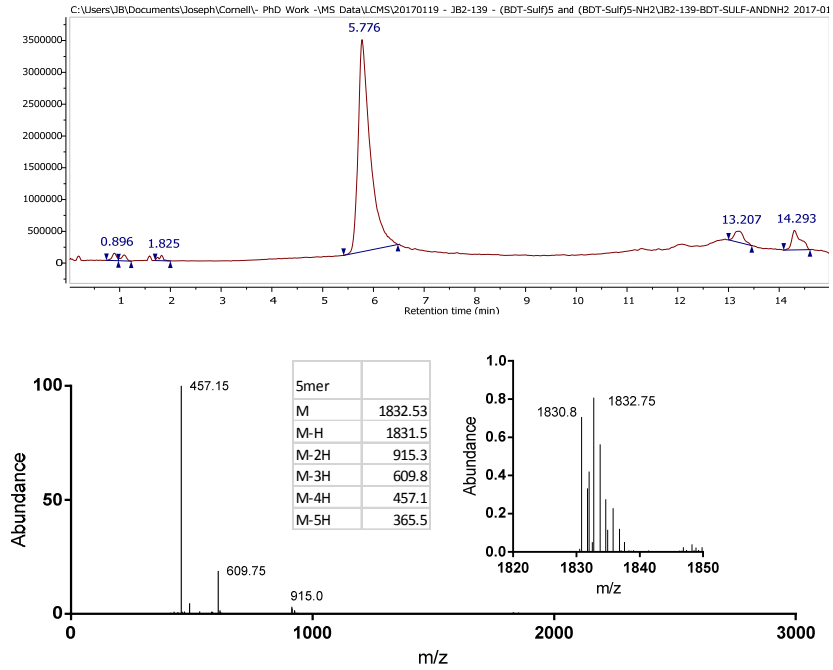


**Figure S63.** Negative mode mass spectra from the LCMS of the (BDT-Sulf)$_5$. The parent mass $(M+H)^{+1}$ is observed as well as the 2$^{nd}$, 3$^{rd}$, and 4$^{th}$ expected masses in table shown.

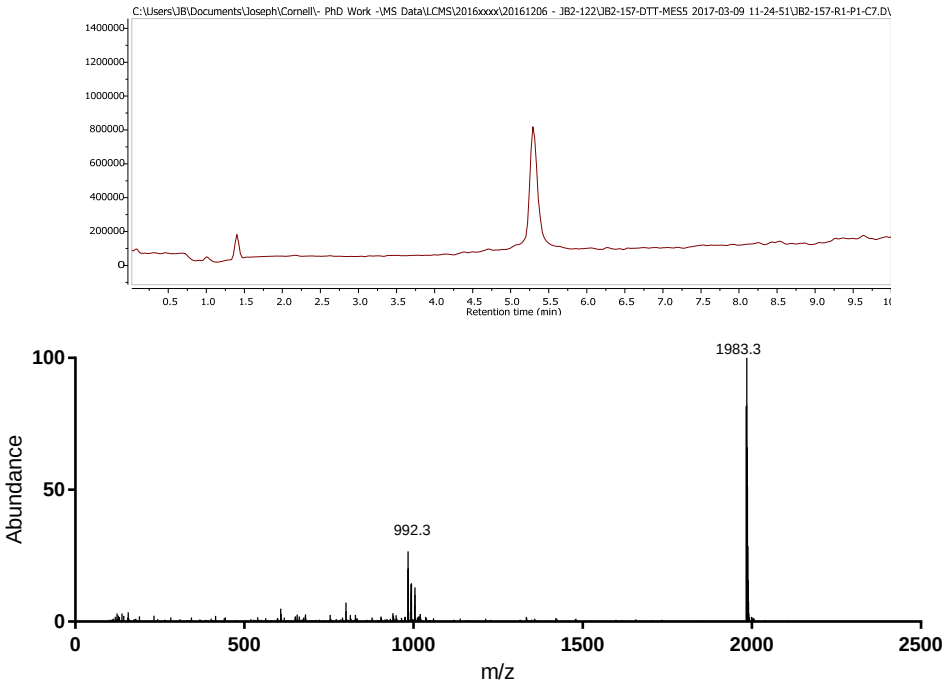


**Figure S64.** Positive mode LCMS TIC (top) and mass spectra (bottom) of the purified $(DTT\text{-}MeS)_5$. Parent mass: 1982.6; $[M+1]^{+1}$ Expected: 1983.6 Obs. 1983.3; $[M+2H]^{+2}$ Expected 992.3 Obs. 992.3.

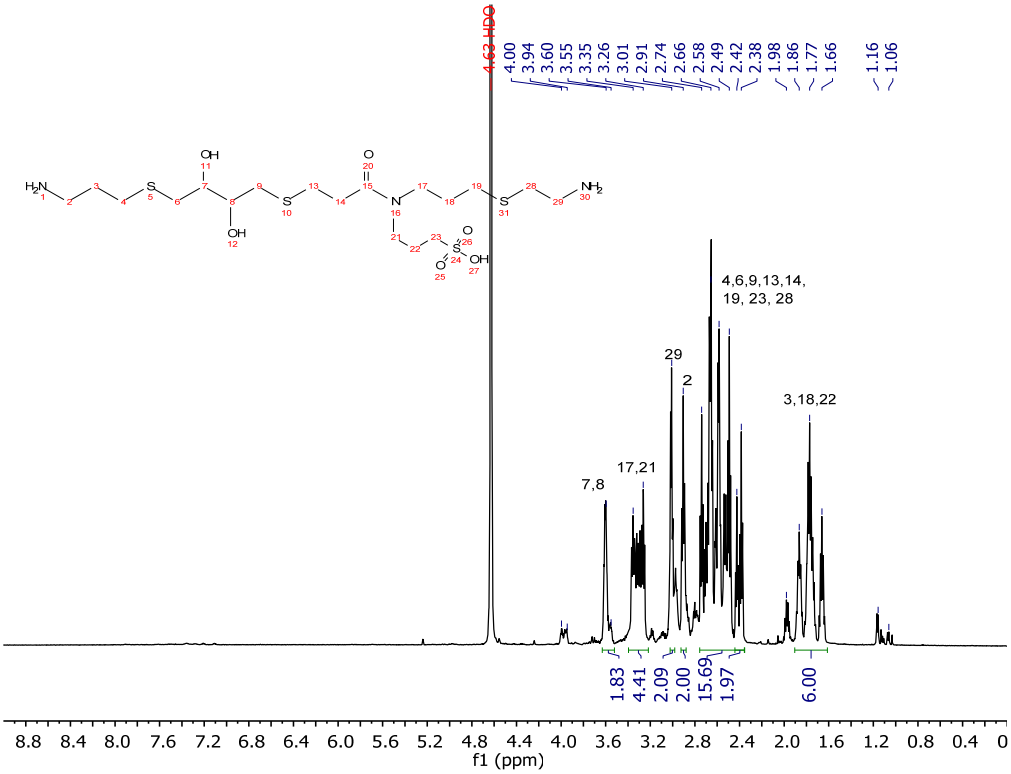


**Figure S65.** $^1H$ NMR of the crude mixture of the amine-capped 2mer $NH_2$-$(DTT\text{-}PSM)_1$-$NH_2$ after TFA cleavage in deuterated water prepared for ESR di-spin labeling with a TEMPO NHS.

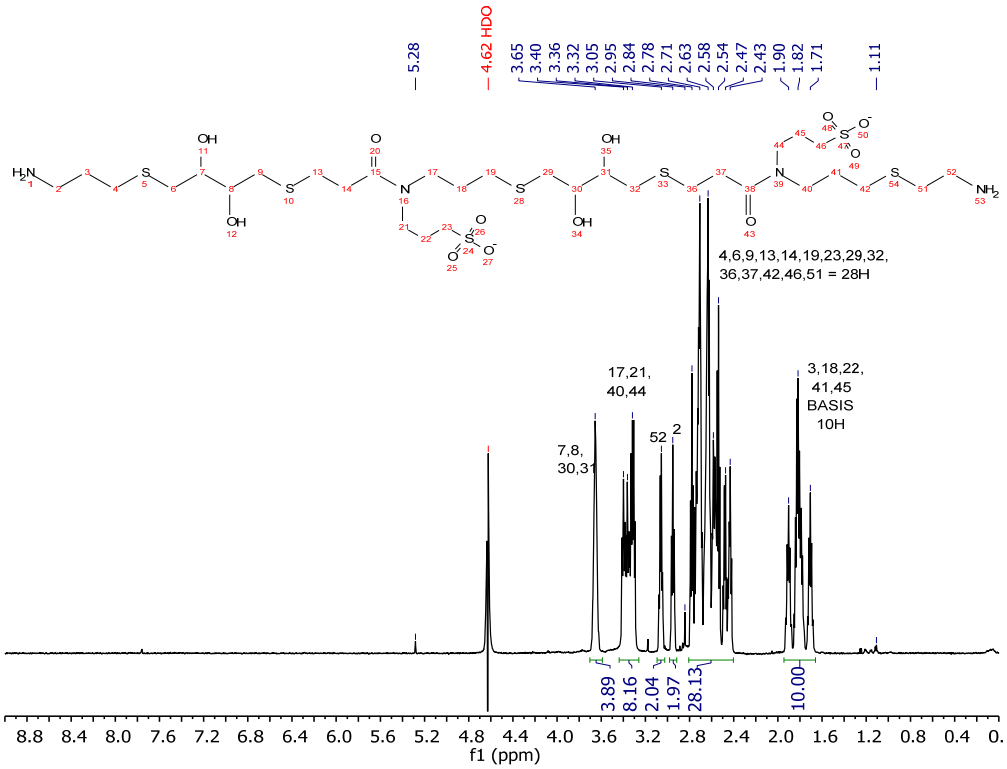


**Figure S66.** $^{1}$H NMR of the amine-capped 4mer $NH_2$-(DTT-PSM)$_2$-$NH_2$ after TFA cleavage and HPLC in deuterated water prepared for ESR di-spin labeling. Solvent suppression was used on the HDO peak.

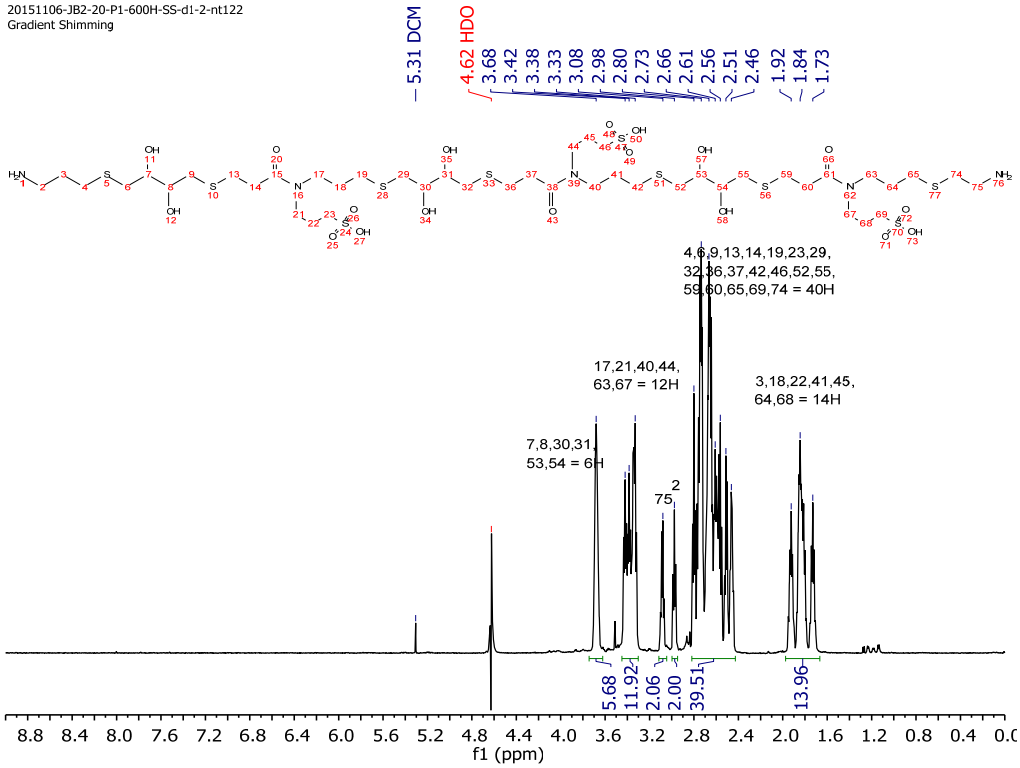


**Figure S67.** $^{1}$H NMR of the amine-capped 6mer $NH_2$-(DTT-PSM)$_3$-$NH_2$ after HPLC in deuterated water for ESR di-spin labeling. Solvent suppression was used on the HDO peak.

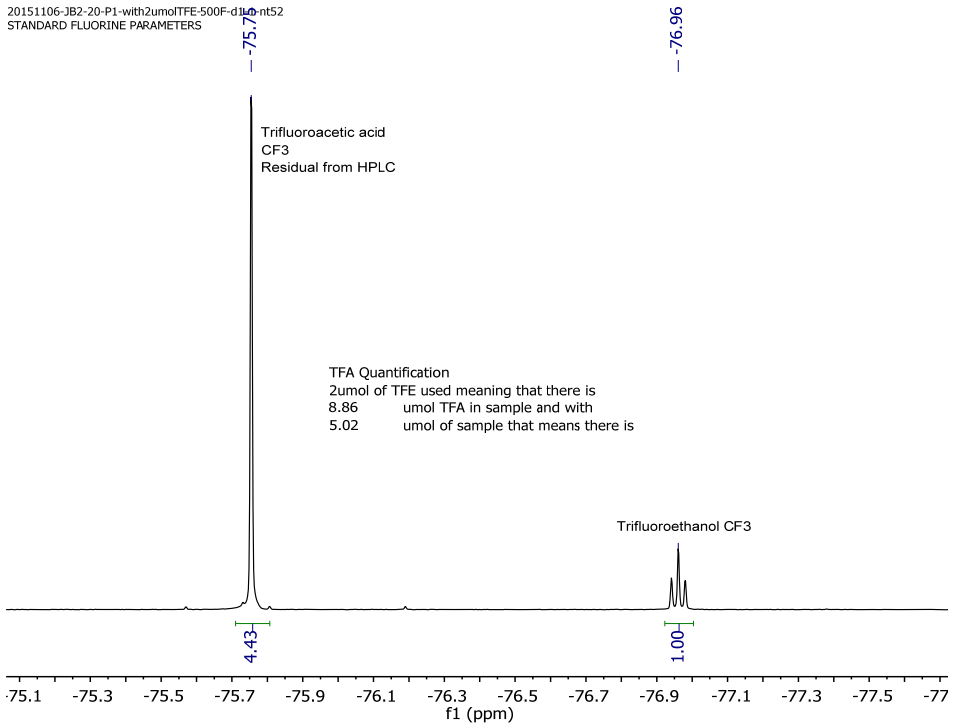


**Figure S68.** $^{19}F$ NMR of the amine-capped 6mer to quantify residual TFA after HPLC where the trifluoro groups for TFA and a trifluoroethanol standard appear at -75.75 and -76.96ppm, respectively. This spectra is shown as an example of the other oligomers where the TFA quantification ensured the correction to the amount of base used in the NHS spin labeling.

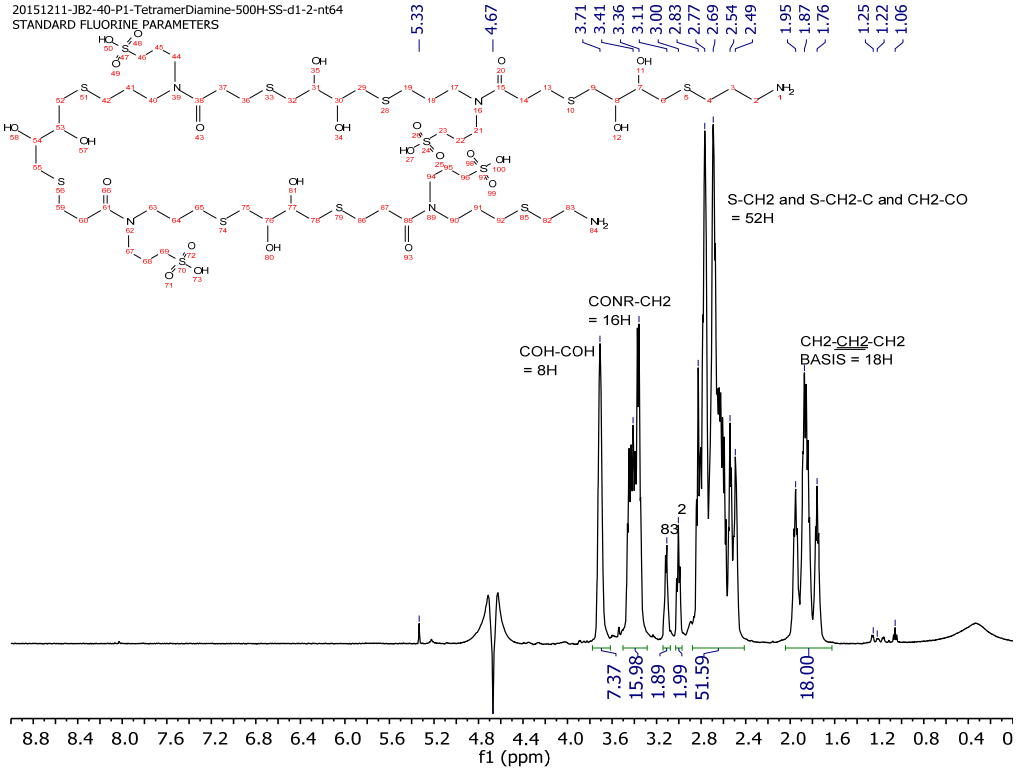


**Figure S69.** $^{1}H$ NMR of the amine-capped 8mer $NH_2$-(DTT-PSM)$_4$-$NH_2$ after HPLC in deuterated water for ESR di-spin labeling. Solvent suppression was used on the HDO peak.

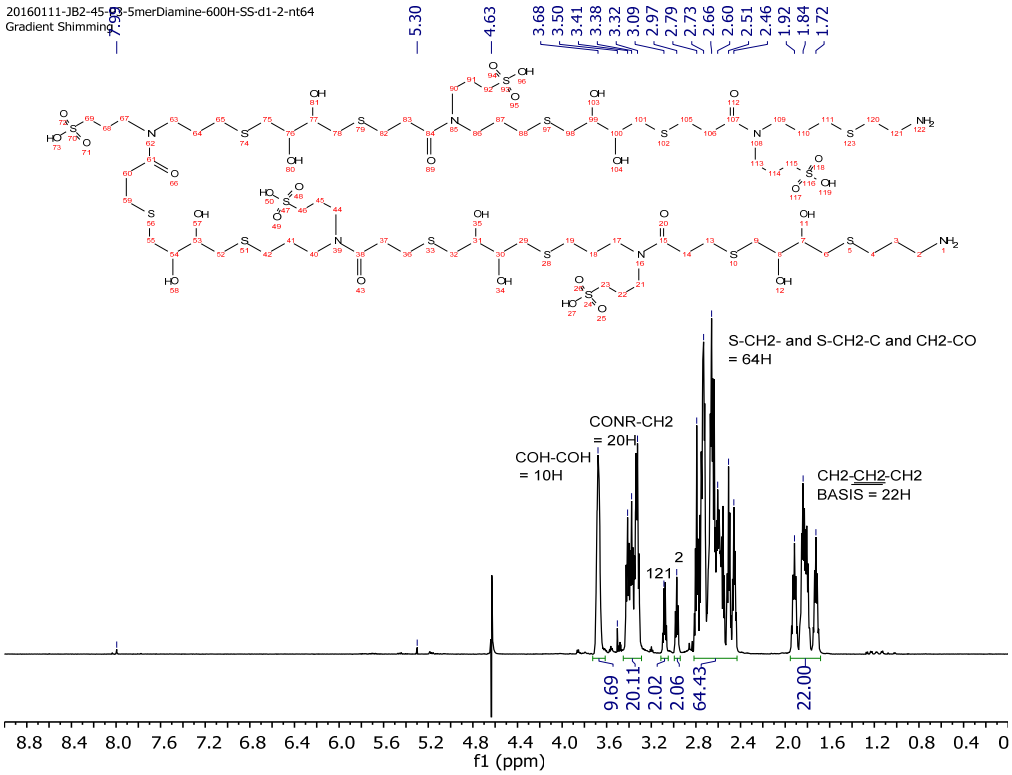


**Figure S70.** $^{1}$H NMR of the amine-capped 10mer $NH_2$-(DTT-PSM)$_5$-$NH_2$ after HPLC in deuterated water for ESR di-spin labeling. Solvent suppression was used on the HDO peak.

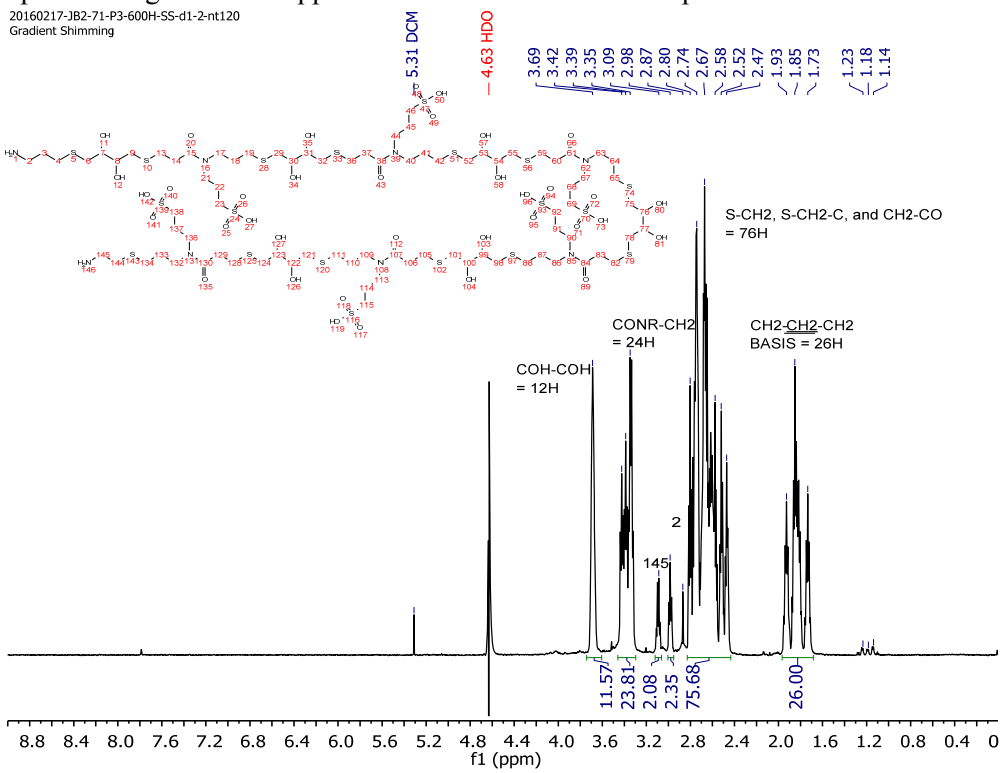


**Figure S71.** $^{1}$H NMR of the amine-capped 12mer $NH_2$-(DTT-PSM)$_6$-$NH_2$ after HPLC in deuterated water for ESR di-spin labeling. Solvent suppression was used on the HDO peak.

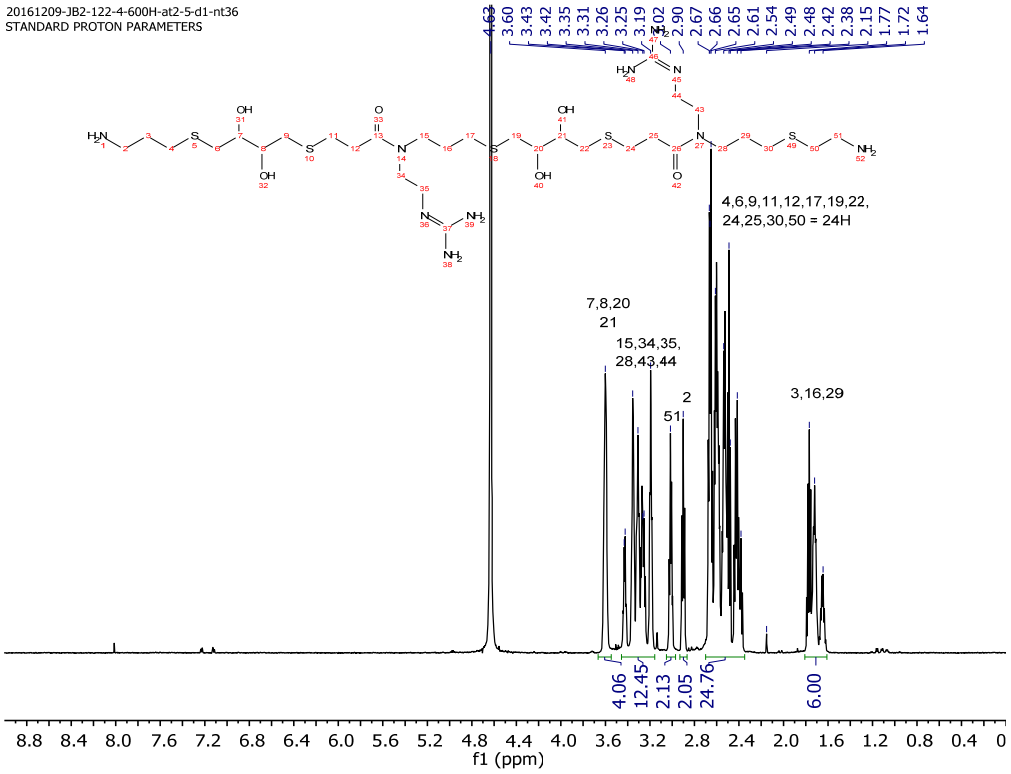


**Figure S72.** $^{1}$H NMR of the amine-capped 4mer $NH_2$-(DTT-G)$_2$-$NH_2$ after HPLC in deuterated water for ESR di-spin labeling.

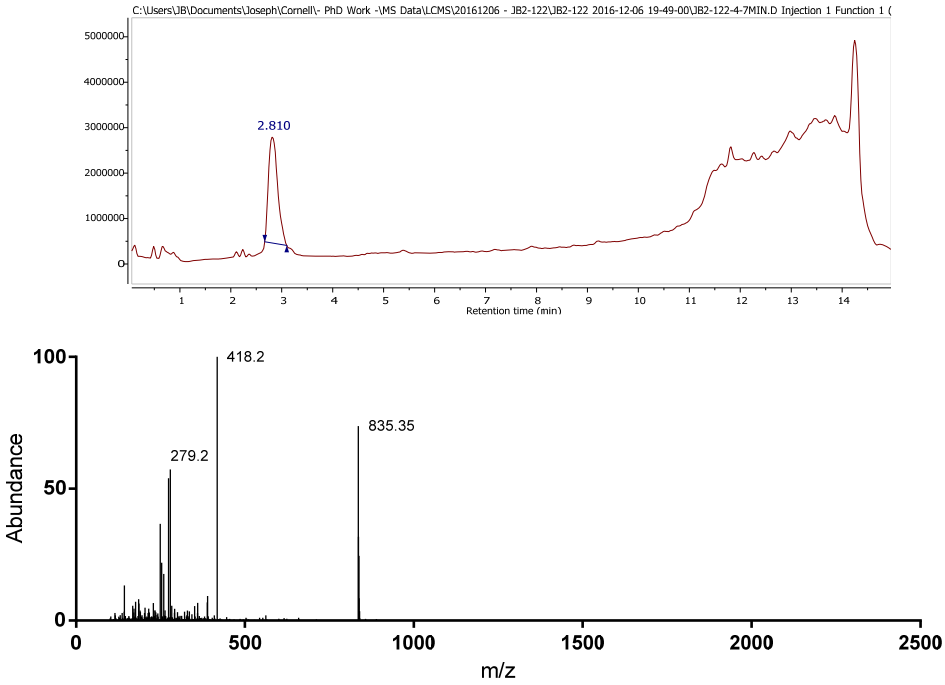


**Figure S73.** Positive mode LCMS of the amine capped $NH_2$-(DTT-G)$_2$-$NH_2$ with the TIC (top) and the mass spectra (bottom). Parent mass: 834.38 as [M]; $[M+H]^{+1}$ Expected: 835.38 Obs. 835.35; $[M+2H]^{+2}$ Expected: 418.20 Obs. 418.2; $[M+3H]^{+3}$ Expected: 279.13 Obs. 279.2.

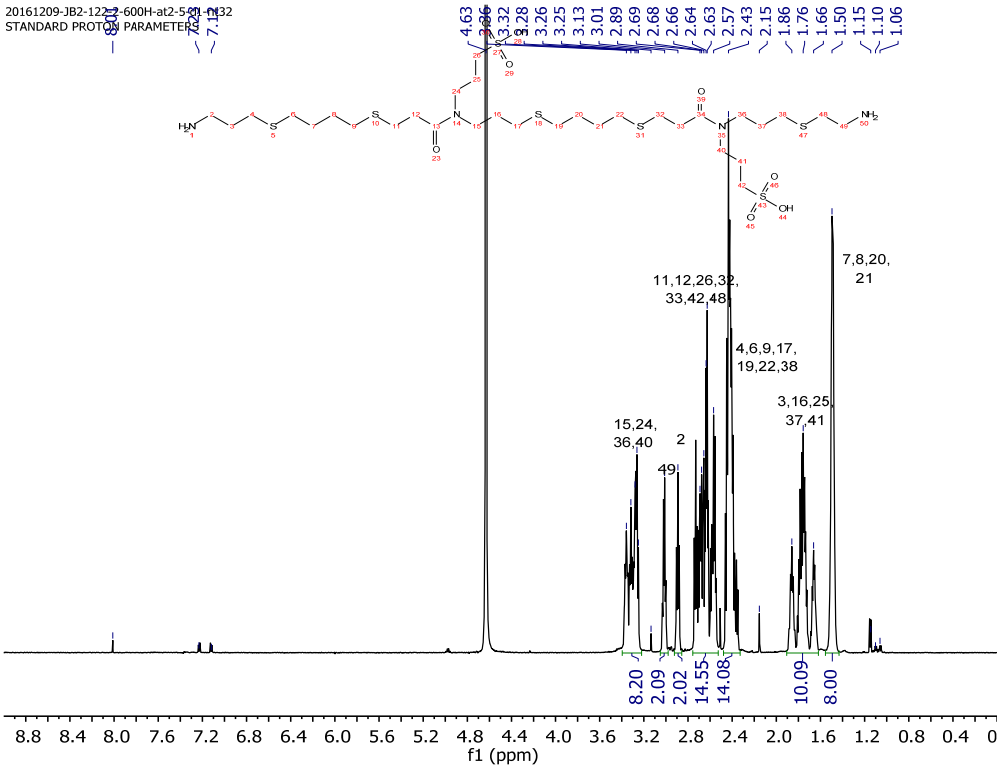


**Figure S74.** $^{1}$H NMR of the amine-capped 4mer $NH_2$-(BDT-Sulf)$_2$-$NH_2$ after HPLC in deuterated water for ESR di-spin labeling.

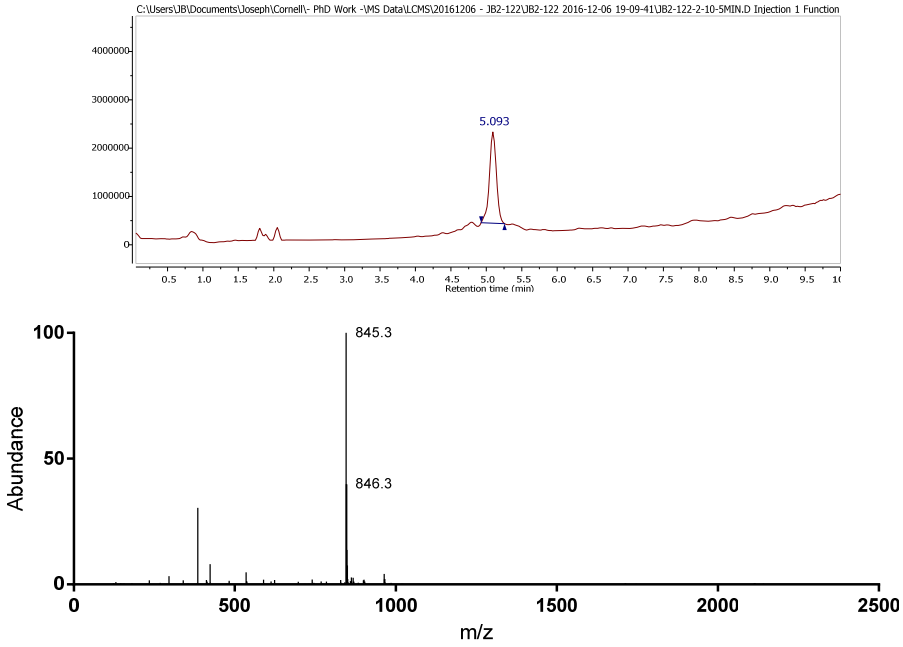


**Figure S75.** Positive mode LCMS of the amine capped $NH_2$-(BDT-Sulf)$_2$-$NH_2$ with the TIC (top) and the mass spectra (bottom). Parent mass: 844.28 as [M]; $[M+H]^{+1}$ Expected: 843.29 Obs. 845.3

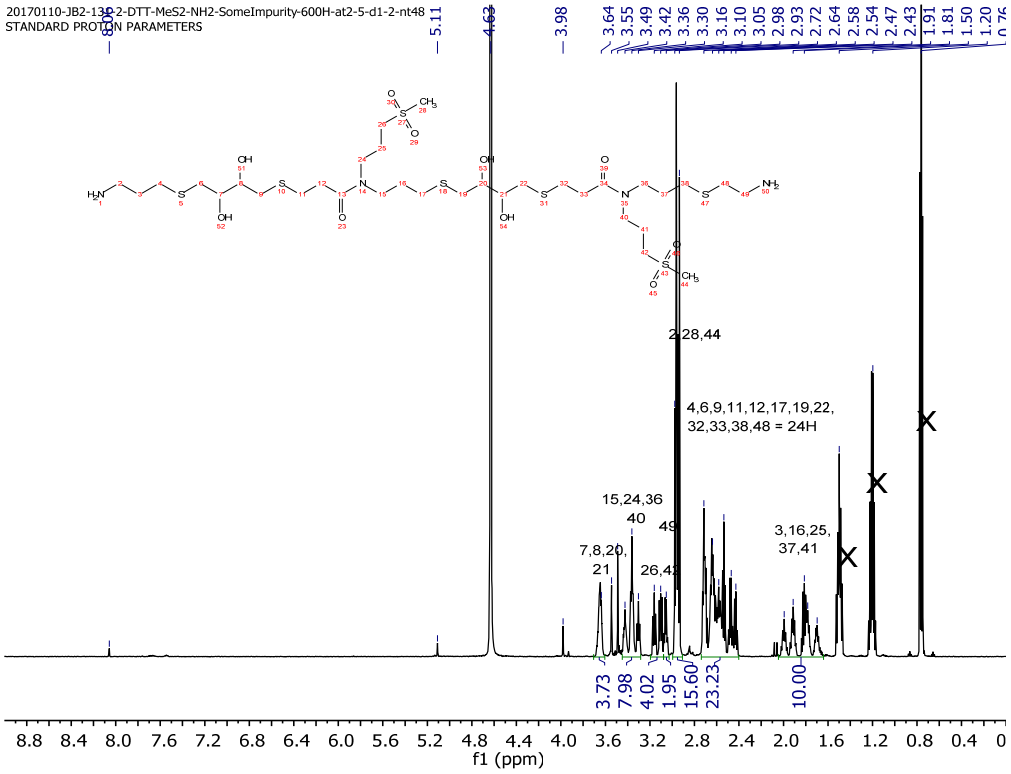


**Figure S76.** $^{1}$H NMR of the amine-capped 4mer $NH_2$-(DTT-MeS)$_2$-$NH_2$ after HPLC in deuterated water for ESR di-spin labeling. The X's mark propylamine contaminant from co-solvent evaporation.

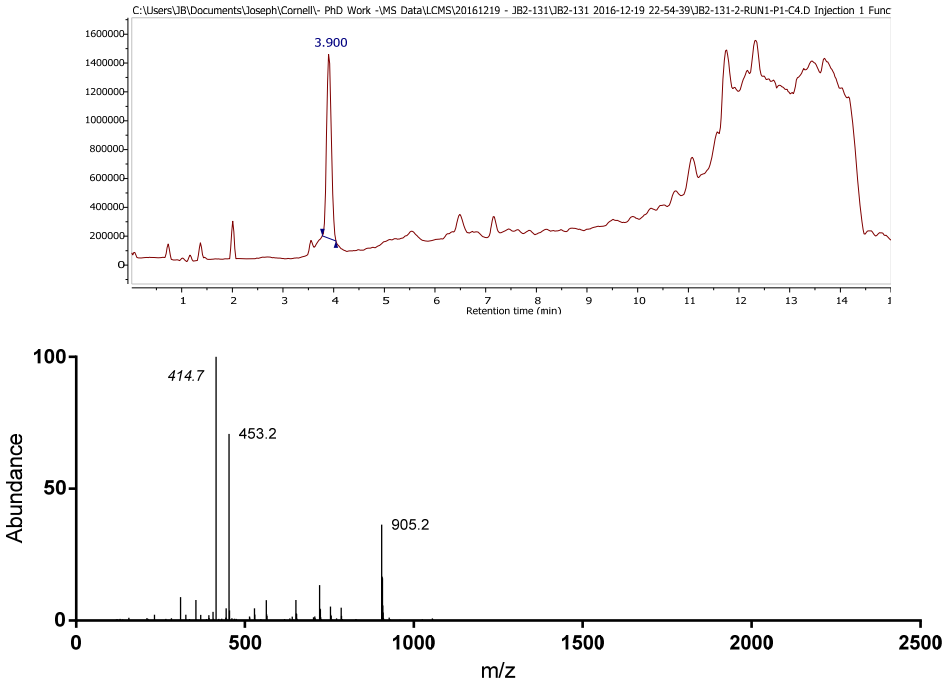


**Figure S77.** Positive mode LCMS of the amine capped $NH_2$-(DTT-MeS)$_2$-$NH_2$ with the TIC (top) and the mass spectra (bottom). Parent mass: 904.30 as [M]; $[M+H]^{+1}$ Expected: 905.31 Obs. 905.2; $[M+2H]^{+2}$ Expected: 453.16 Obs. 453.2. The 414.7m/z is unknown.

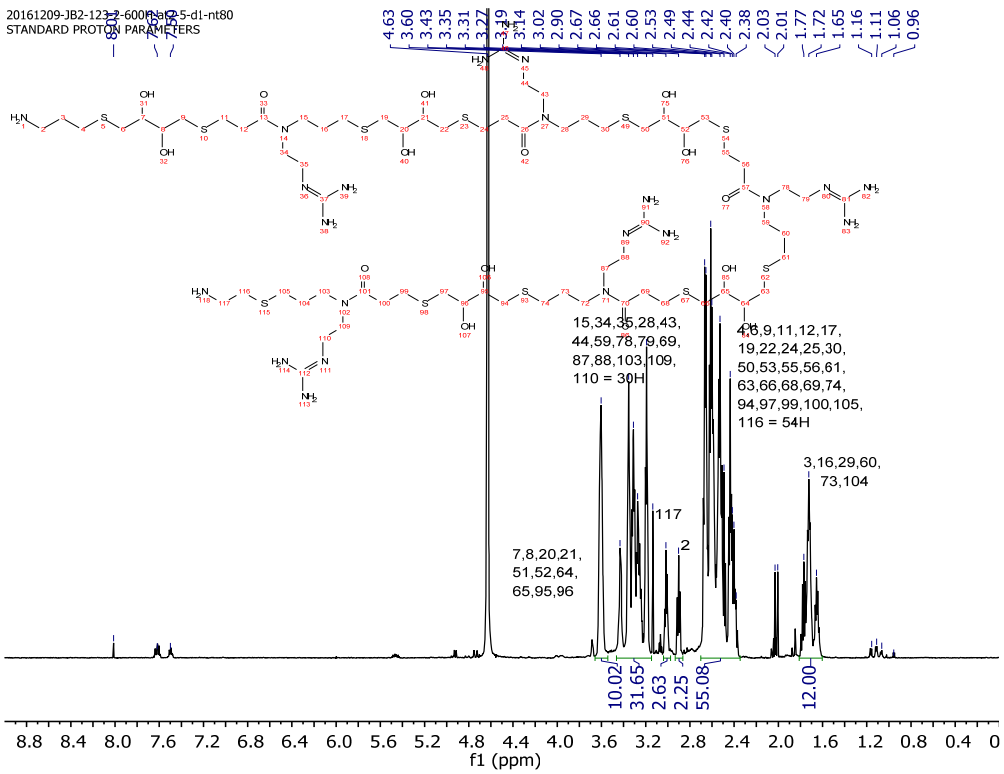


**Figure S78.** $^{1}$H NMR of the amine-capped 10mer $NH_2$-(DTT-G)$_5$-$NH_2$ after HPLC in deuterated water for ESR di-spin labeling.

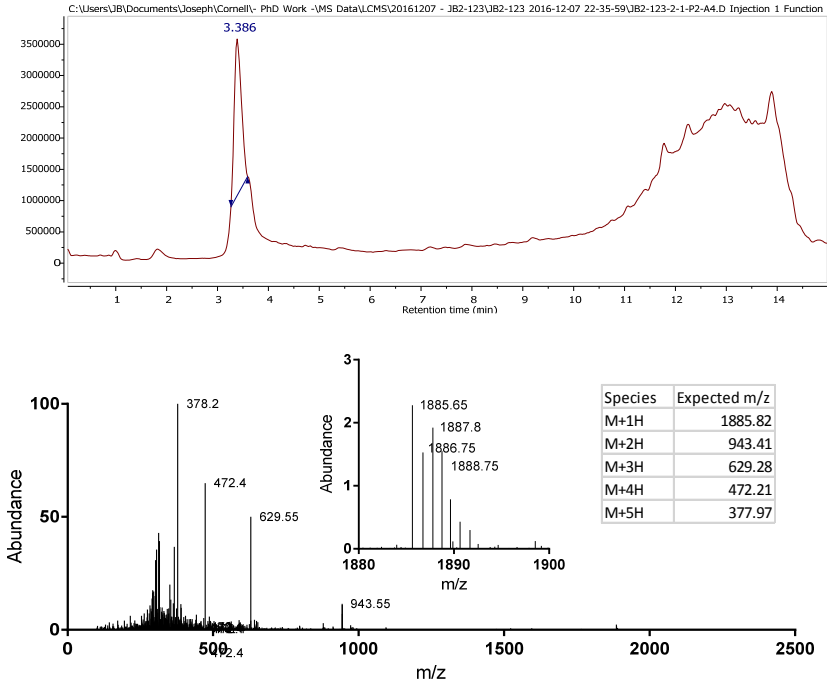


**Figure S79.** Positive mode LCMS of the amine capped $NH_2$-(DTT-G)$_5$-$NH_2$ with the TIC (top) and the mass spectra (bottom). Masses were expected as indicated in the inset table and observed as seen.

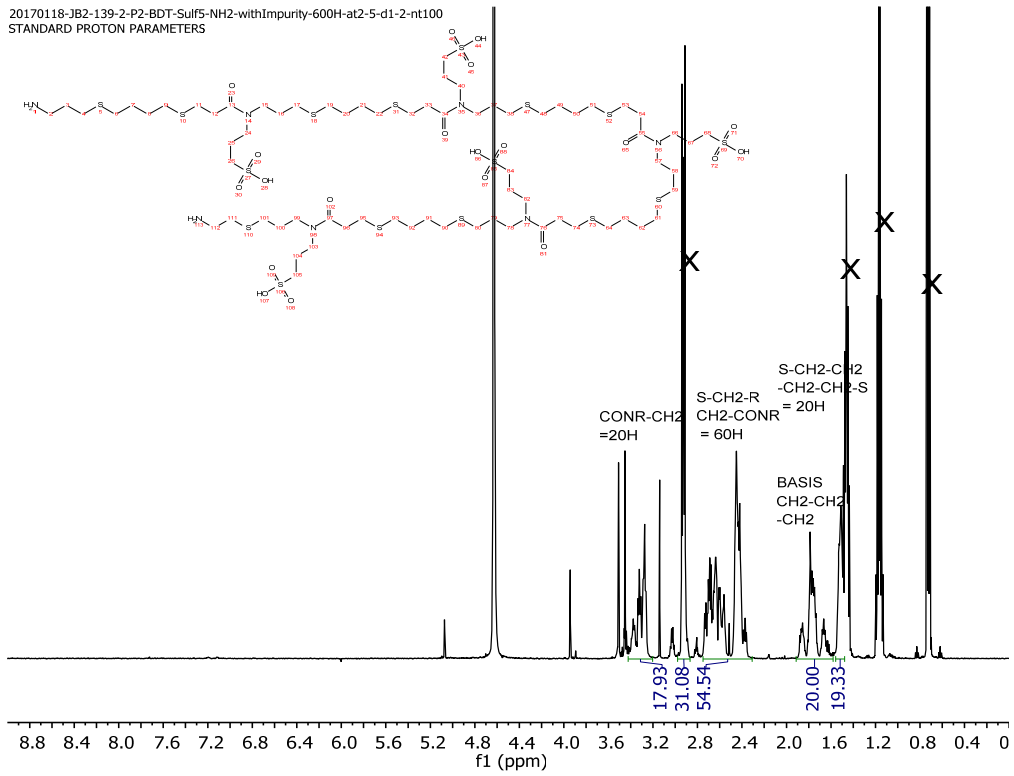


**Figure S80.** $^{1}$H NMR of the amine-capped 10mer $NH_2$-(BDT-Sulf)$_5$-$NH_2$ after HPLC in deuterated water for ESR di-spin labeling.

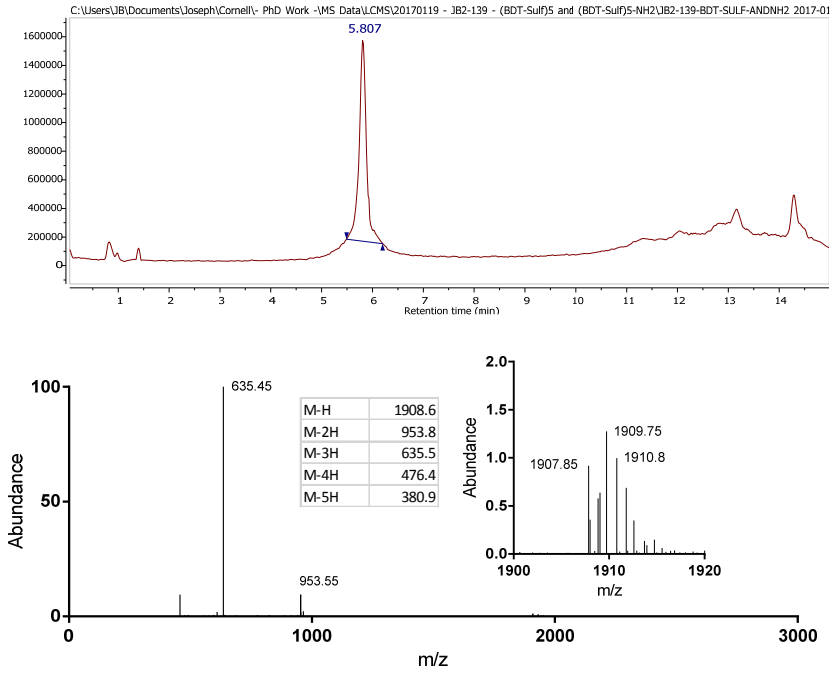


**Figure S81.** Negative mode LCMS of the amine capped $NH_2$-(BDT-Sulf)$_5$-$NH_2$ with the TIC (top) and the mass spectra (bottom). Masses were expected as indicated in the inset table and observed as seen.

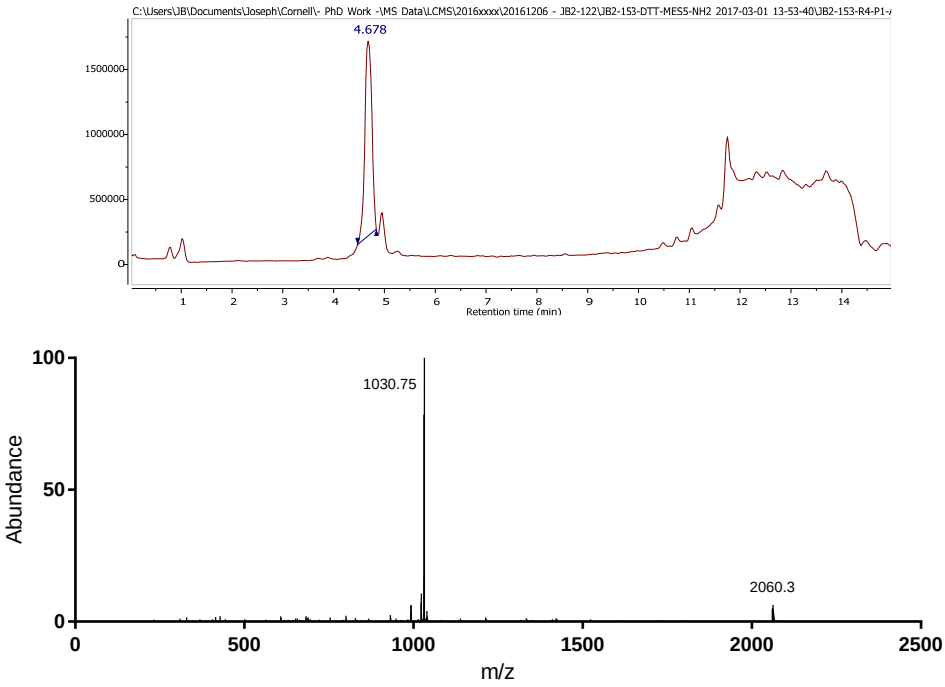


**Figure S82.** Positive mode LCMS of the amine capped $NH_2$-(DTT-MeS)$_5$-$NH_2$ with the TIC (top) and the mass spectra (bottom). Parent mass: 2059.61; $[M+H]^{+1}$ Expected 2060.62 Obs. 2060.3; $[M+2H]^{+2}$ Expected 1030.81 Obs. 1030.75.

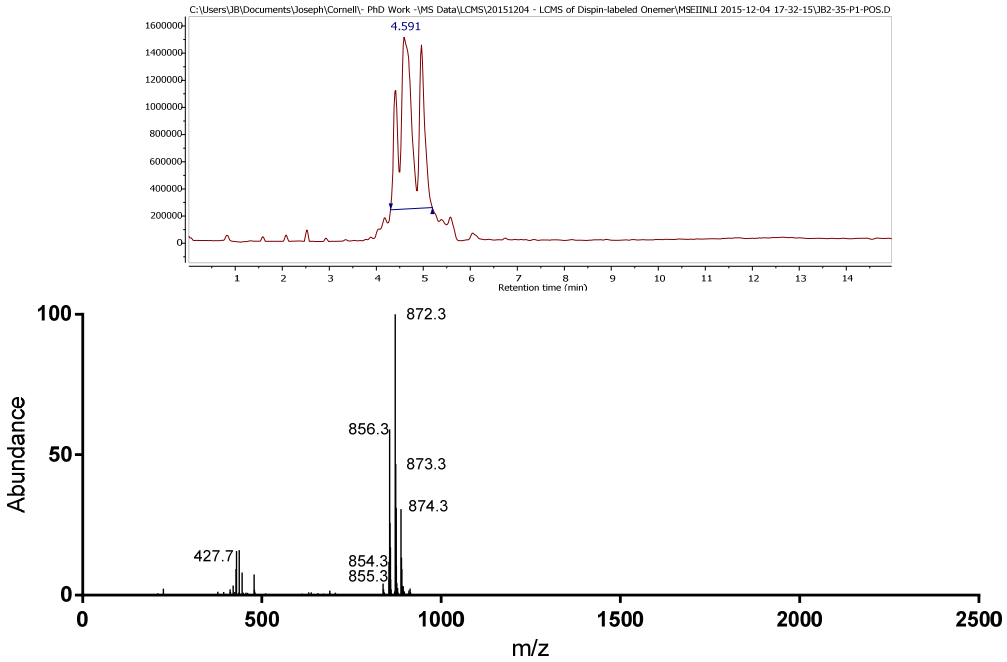


**Figure S83.** Positive mode LCMS of the dispin labeled (PROXYL) 2mer with the TIC (top) and the mass spectra (bottom) showing a distribution of the nitroxide oxidation states. Parent mass: 853.35 as $[M]^{\bullet\bullet}$; $[M+H]^{+1\bullet\bullet}$ Expected: 854.36 Obs. 854.3; $[M+H]^{+1\bullet}$ Expected: 855.37 Obs. 855.3; $[M+H]^{+1}$ Expected: 856.37 Obs. 856.3; $[M+NH_4]^{+1\bullet}$ Expected: 872.40 Obs. 872.3; $[M+NH_4]^{+1}$ Expected: 873.40 Obs. 873.3.

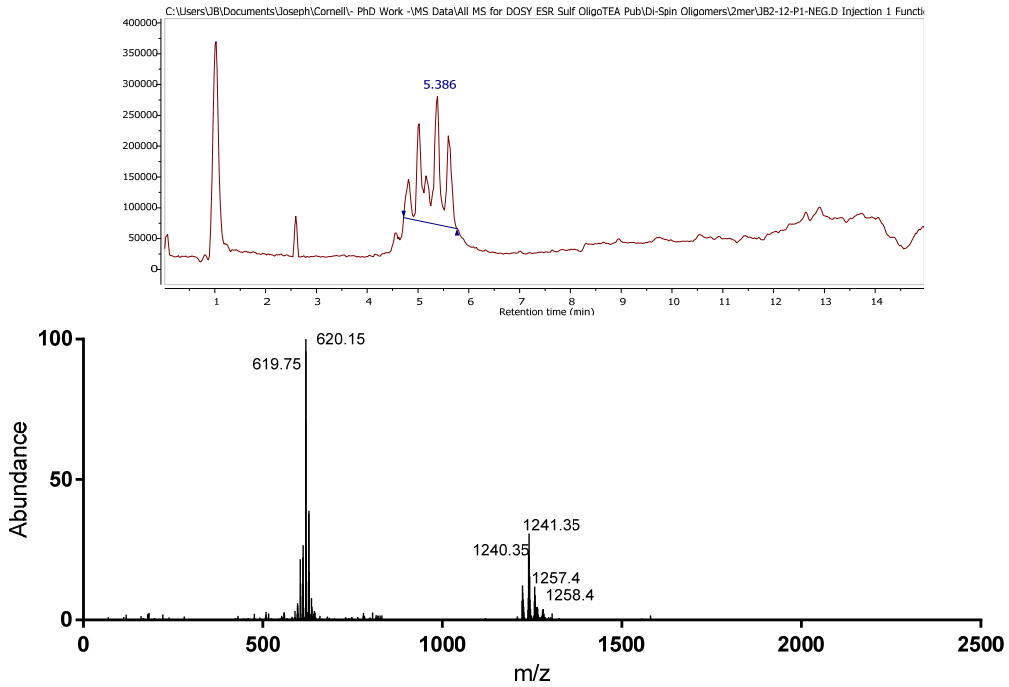


**Figure S84.** Negative mode LCMS of the dispin labeled (PROXYL) 4mer with the TIC (top) and the mass spectra (bottom) showing a distribution of the nitroxide oxidation states. Parent mass: 1240.43 as $[M]^{\bullet\bullet}$; $[M\text{-}H]^{-1\bullet}$ Expected: 1240.43 Obs. 1240.35; $[M\text{-}H]^{-1}$ Expected: 1241.44 Obs. 1241.35; $[M\text{-}2H\text{+}NH_4]^{-1\bullet}$ Expected: 1257.46 Obs. 1257.4; $[M\text{-}2H\text{+}NH_4]^{-1}$ Expected: 1258.47 Obs. 1258.4; $[M\text{-}2H]^{-2\bullet}$ Expected: 619.71 Obs. 619.75; $[M\text{-}2H]^{-2}$ Expected: 620.22 Obs. 620.15.

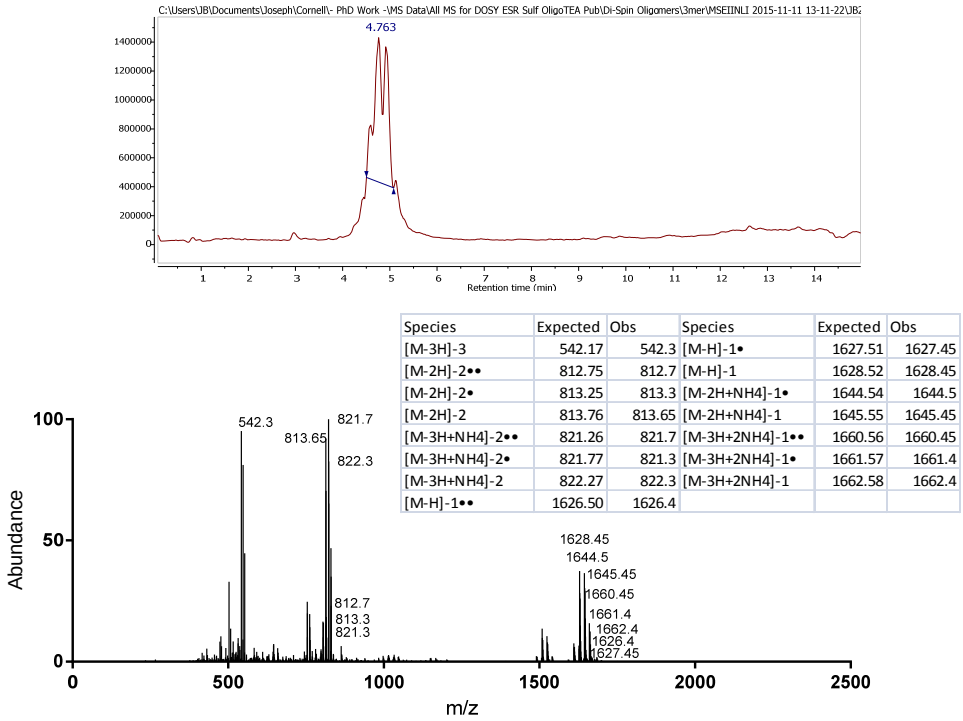


| Species | Expected | Obs | Species | Expected | Obs |
|---|---|---|---|---|---|
| [M-3H]-3 | 542.17 | 542.3 | [M-H]-1• | 1627.51 | 1627.45 |
| [M-2H]-2•• | 812.75 | 812.7 | [M-H]-1 | 1628.52 | 1628.45 |
| [M-2H]-2• | 813.25 | 813.3 | [M-2H+NH4]-1• | 1644.54 | 1644.5 |
| [M-2H]-2 | 813.76 | 813.65 | [M-2H+NH4]-1 | 1645.55 | 1645.45 |
| [M-3H+NH4]-2•• | 821.26 | 821.7 | [M-3H+2NH4]-1•• | 1660.56 | 1660.45 |
| [M-3H+NH4]-2• | 821.77 | 821.3 | [M-3H+2NH4]-1• | 1661.57 | 1661.4 |
| [M-3H+NH4]-2 | 822.27 | 822.3 | [M-3H+2NH4]-1 | 1662.58 | 1662.4 |
| [M-H]-1•• | 1626.50 | 1626.4 | | | |

**Figure S85.** Negative mode LCMS of the dispin labeled (TEMPO) 6mer with the TIC (top) and the mass spectra (bottom) showing a distribution of the nitroxide oxidation states. Parent mass: 1627.51 as $[M]^{\bullet\bullet}$ where observed species are indicated in the inset table.

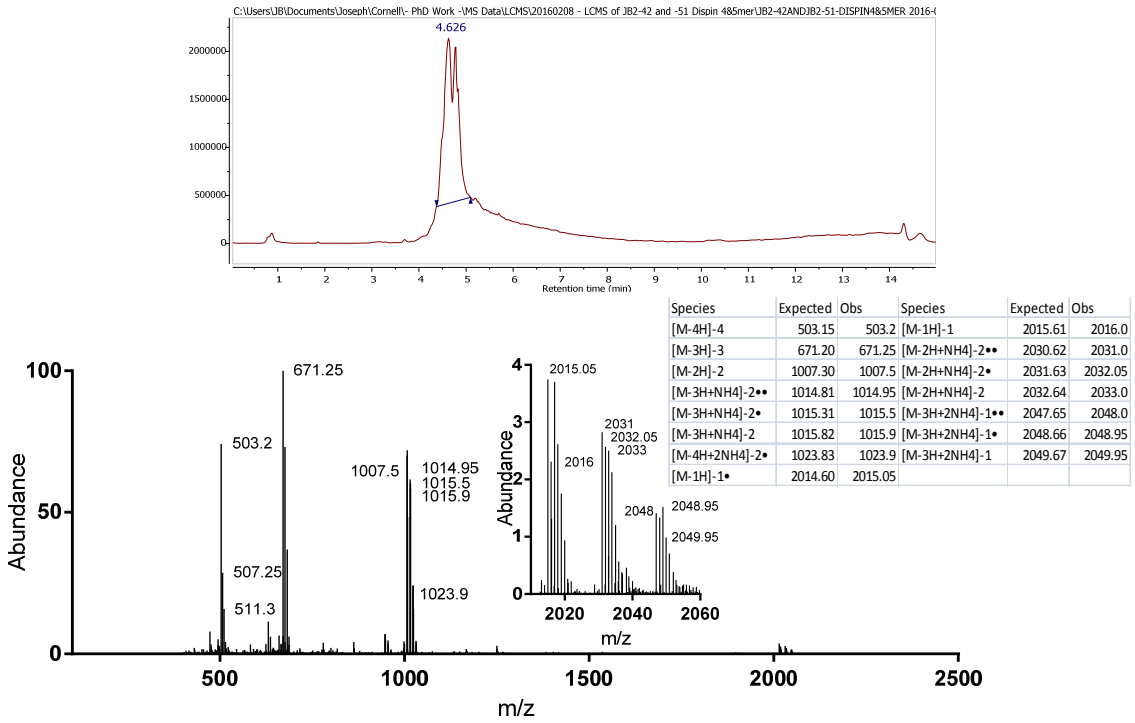


| Species | Expected | Obs | Species | Expected | Obs |
|---|---|---|---|---|---|
| [M-4H]-4 | 503.15 | 503.2 | [M-1H]-1 | 2015.61 | 2016.0 |
| [M-3H]-3 | 671.20 | 671.25 | [M-2H+NH4]-2•• | 2030.62 | 2031.0 |
| [M-2H]-2 | 1007.30 | 1007.5 | [M-2H+NH4]-2• | 2031.63 | 2032.05 |
| [M-3H+NH4]-2•• | 1014.81 | 1014.95 | [M-2H+NH4]-2 | 2032.64 | 2033.0 |
| [M-3H+NH4]-2• | 1015.31 | 1015.5 | [M-3H+2NH4]-1•• | 2047.65 | 2048.0 |
| [M-3H+NH4]-2 | 1015.82 | 1015.9 | [M-3H+2NH4]-1• | 2048.66 | 2048.95 |
| [M-4H+2NH4]-2• | 1023.83 | 1023.9 | [M-3H+2NH4]-1 | 2049.67 | 2049.95 |
| [M-1H]-1• | 2014.60 | 2015.05 | | | |

**Figure S86.** Negative mode LCMS of the dispin labeled (PROXYL) 8mer with the TIC (top) and the mass spectra (bottom) showing a distribution of the nitroxide oxidation states. Parent mass: 2014.60 as [M]¨ where observed species are indicated in the inset table.

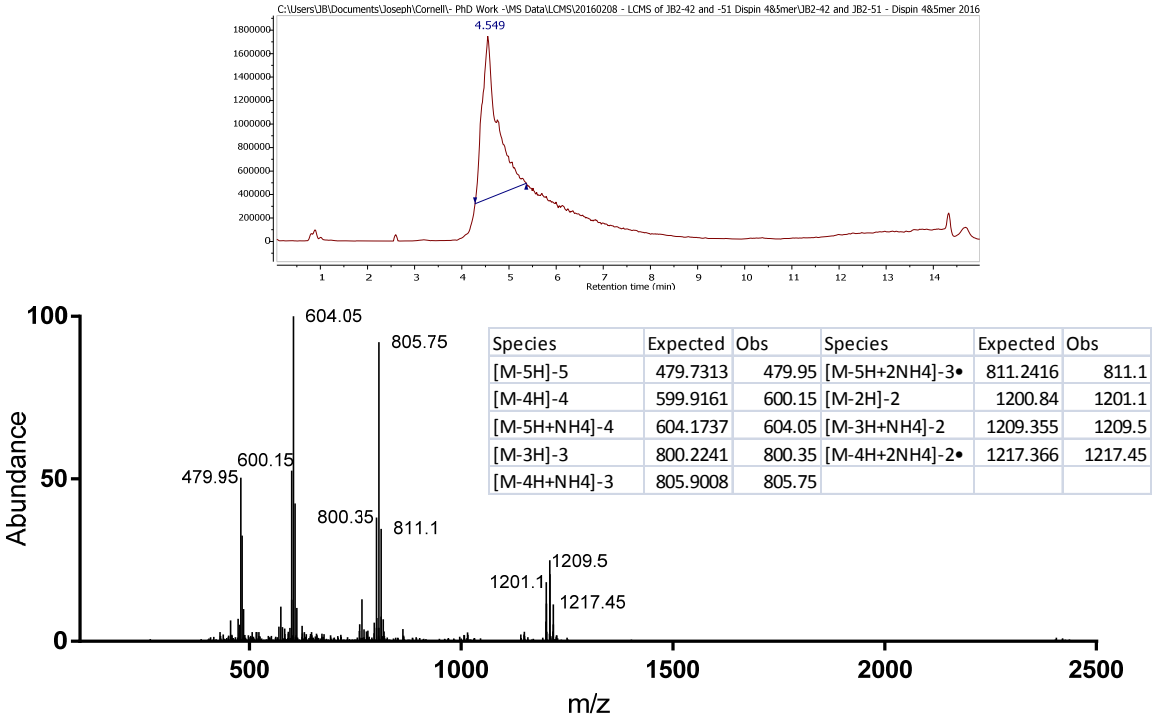


| Species | Expected | Obs | Species | Expected | Obs |
|---|---|---|---|---|---|
| [M-5H]-5 | 479.7313 | 479.95 | [M-5H+2NH4]-3• | 811.2416 | 811.1 |
| [M-4H]-4 | 599.9161 | 600.15 | [M-2H]-2 | 1200.84 | 1201.1 |
| [M-5H+NH4]-4 | 604.1737 | 604.05 | [M-3H+NH4]-2 | 1209.355 | 1209.5 |
| [M-3H]-3 | 800.2241 | 800.35 | [M-4H+2NH4]-2• | 1217.366 | 1217.45 |
| [M-4H+NH4]-3 | 805.9008 | 805.75 | | | |

**Figure S87.** Negative mode LCMS of the dispin labeled (PROXYL) 10mer with the TIC (top) and the mass spectra (bottom) showing a distribution of the nitroxide oxidation states. Parent mass: 2401.68 as [M]¨ where observed species are indicated in the inset table.

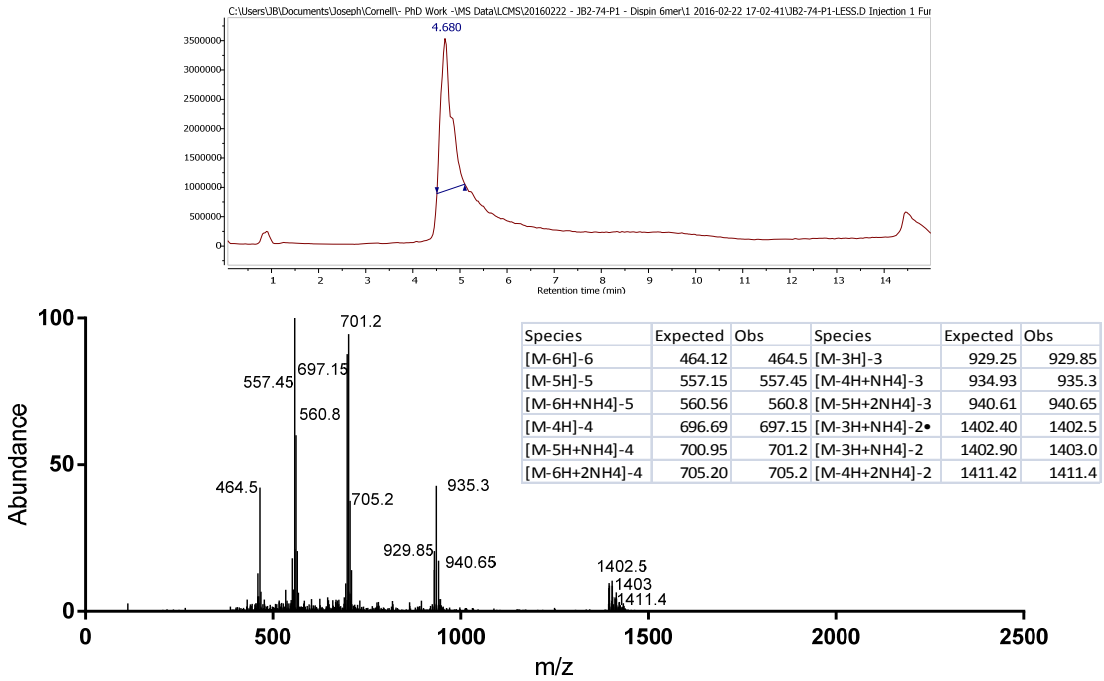


**Figure S88.** Negative mode LCMS of the dispin labeled (PROXYL) 12mer with the TIC (top) and the mass spectra (bottom) showing a distribution of the nitroxide oxidation states. Parent mass: 2788.77 as [M]¨ where observed species are indicated in the inset table.

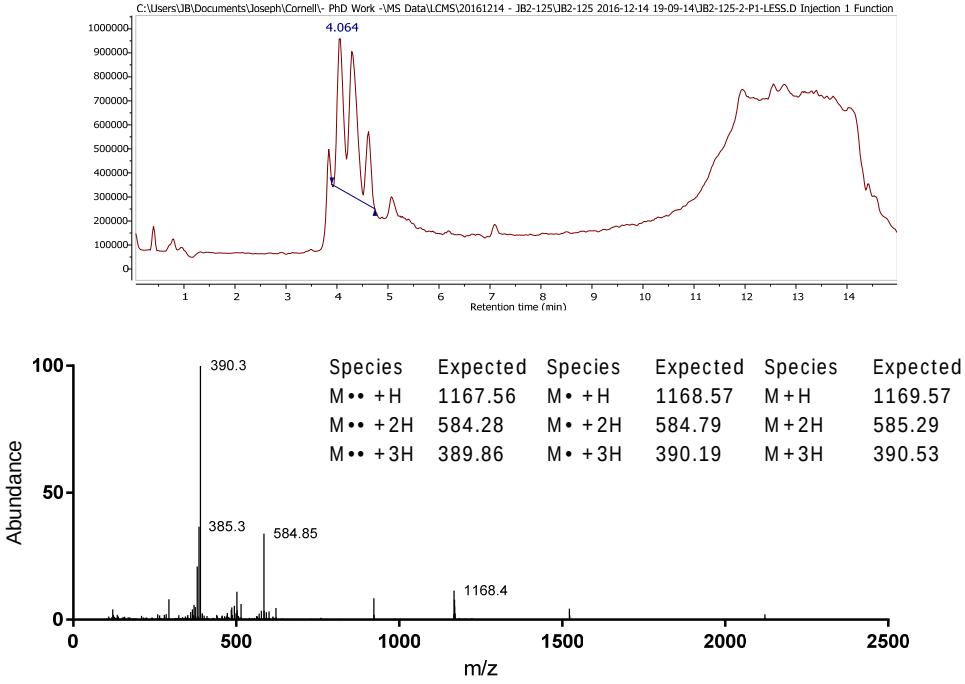


**Figure S89.** Positive mode LCMS of the dispin labeled (PROXYL) $(DTT\text{-}G)_2$ where the parent and half-mass are observed as indicated in the table showing a distribution of the nitroxide oxidation states.

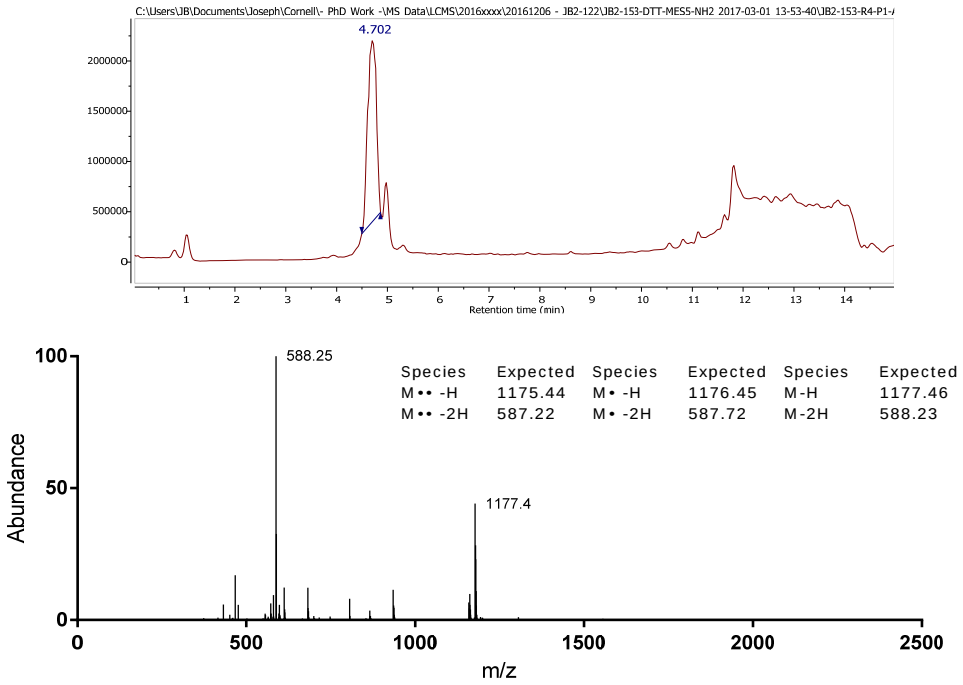


**Figure S90.** Negative mode LCMS of the dispin labeled (PROXYL) $(BDT\text{-}Sulf)_2$ where the parent and half-mass are observed as indicated in the table showing a distribution of the nitroxide oxidation states.

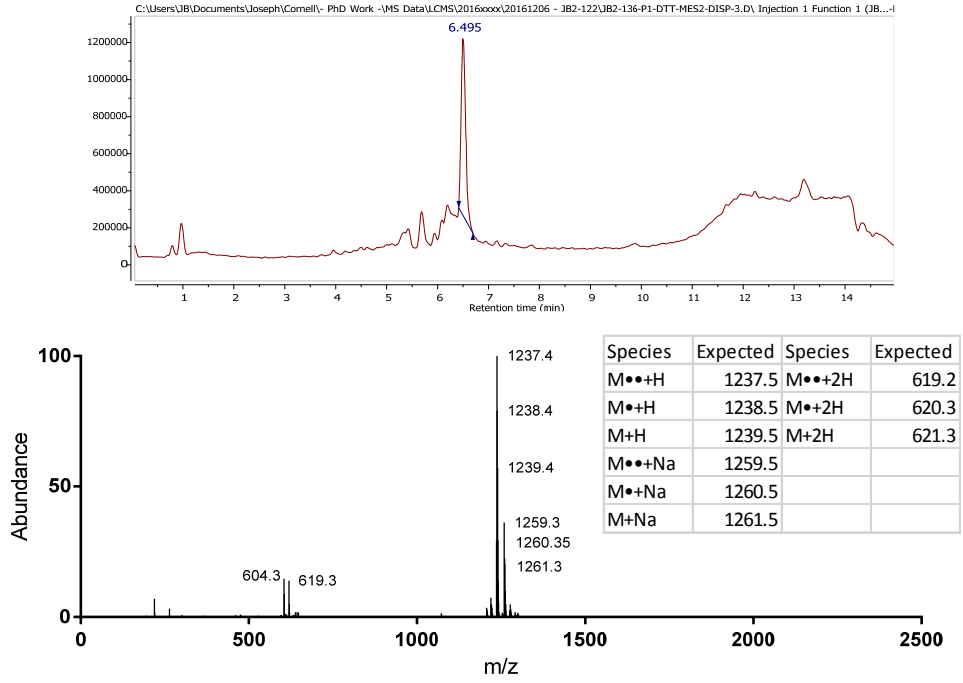


**Figure S91.** Positive mode mass spectra from the LCMS of the collected peak from HPLC of the dispin labeled $(DTT\text{-}MeS)_2\text{-}NH_2$. The parent and half masses are observed showing a distribution of the nitroxide oxidation states.

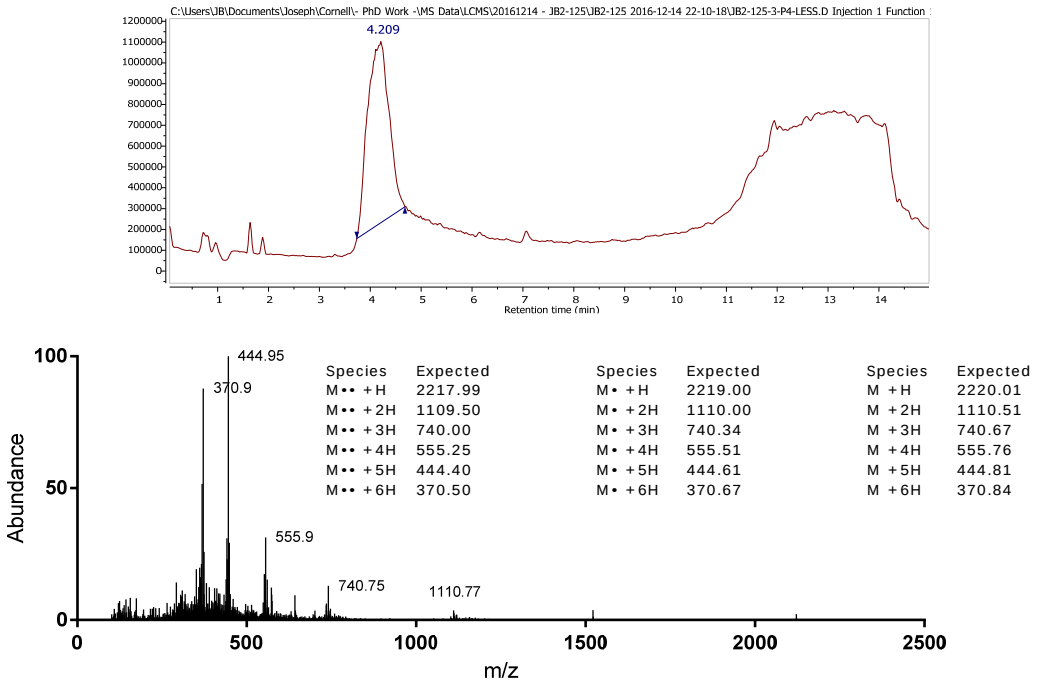


**Figure S92.** Positive mode mass spectra from the LCMS of the collected peak from HPLC of the dispin labeled $(DTT\text{-}G)_5\text{-}NH_2$. The parent mass is not observed, but the half, third, fourth, and fifth masses are observed showing a distribution of the nitroxide oxidation states.

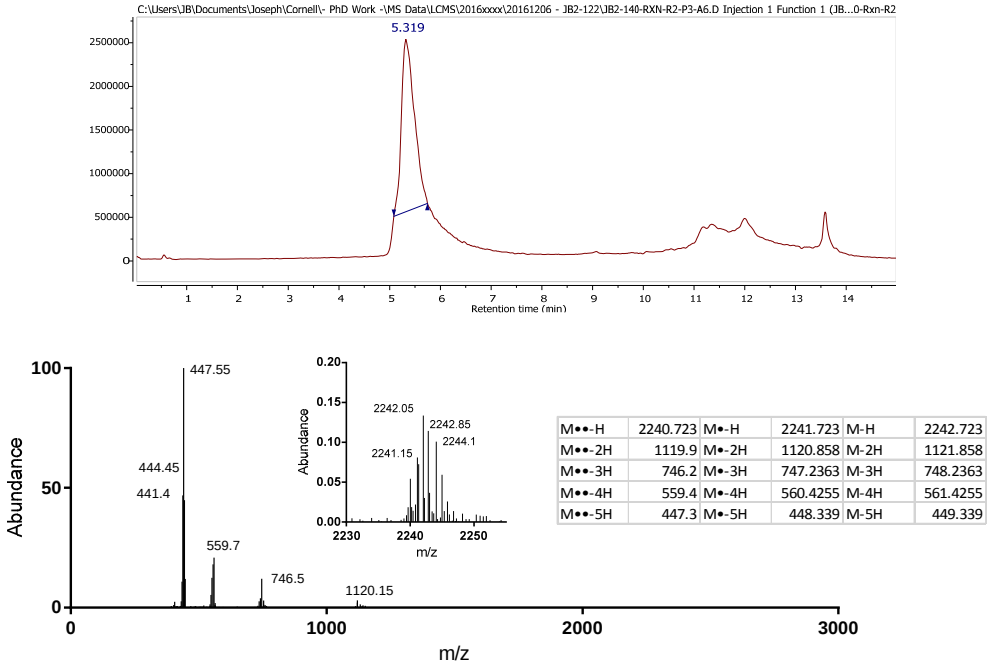


**Figure S93.** Negative mode mass spectra from the LCMS of the dispin labeled $(BDT\text{-}Sulf)_5\text{-}NH_2$. The parent mass $(M+H)^{+1}$ is observed as well as the 2nd and 3rd masses showing a distribution of the nitroxide oxidation states.

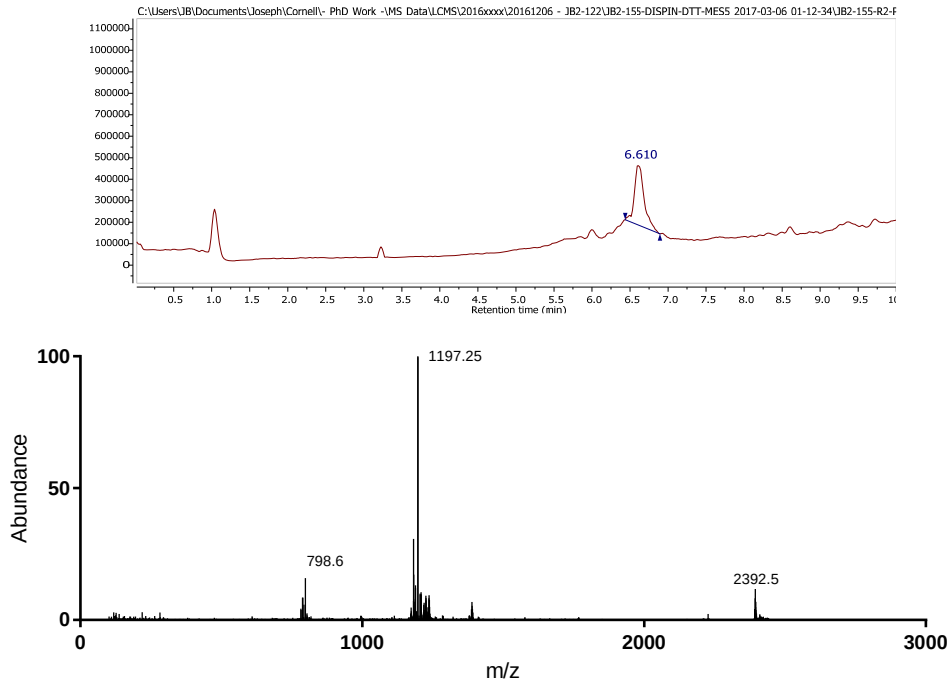


**Figure S94.** Positive mode LCMS TIC (top) and mass spectra (bottom) of the purified dispin labeled $(DTT\text{-}MeS)_5\text{-}NH_2$. The full (expected 2392.8 m/z), half mass (expected 1196.9 m/z), and third mass (expected 798.3 m/z) are observed. The PROXYL-$(DTT\text{-}MeS)_5$-PROXYL does not ionize that well, which makes sense with no simple means of ionization (amine, etc).

## References


(1) Pauff, S. M.; Miller, S. C. A Trifluoroacetic Acid-Labile Sulfonate Protecting Group and Its Use in the Synthesis of a near-IR Fluorophore. *J. Org. Chem.* **2013**, *78* (2), 711–716.

(2) Porel, M.; Alabi, C. A. Sequence-Defined Polymers via Orthogonal Allyl Acrylamide Building Blocks. *J. Am. Chem. Soc.* **2014**, *136* (38), 13162–13165.

(3) Egwim, I. O.; Gruber, H. J. Spectrophotometric Measurement of Mercaptans with 4,4'-dithiodipyridine. *Anal. Biochem.* **2001**, *288* (2), 188–194.

(4) Grassetti, D. R.; Murray, J. F. Determination of Sulfhydryl Groups with 2,2'- or 4,4'-dithiodipyridine. *Arch. Biochem. Biophys.* **1967**, *119* (1), 41–49.

(5) Alexej, J.; Norbert, M. Suppression of Convection Artifacts in Stimulated-Echo Diffusion Experiemnts. Double-Stimulated-Echo Experiments. *J. Magn. Reson.* **1997**, *375* (125), 372–375.

(6) Antalek, B. Using Pulsed Gradient Spin Echo NMR for Chemical Mixture Analysis: How to Obtain Optimum Results. *Concepts Magn. Reson. Part A Bridg. Educ. Res.* **2002**, *14* (4), 225–258.

(7) Holz, M.; Heil, S. R.; Sacco, A. Temperature-Dependent Self-Diffusion Coefficients of Water and Six Selected Molecular Liquids for Calibration in Accurate 1H NMR PFG Measurements. *Phys. Chem. Chem. Phys.* **2000**, *2* (20), 4740–4742.

(8) Longsworth, L. G. THE MUTUAL DIFFUSION OF LIGHT AND HEAVY WATER. *J. Phys. Chem.* **1960**, *64* (12), 1914–1917.

(9) Lapham, J.; Rife, J. P.; Moore, P. B.; Crothers, D. M. Measurement of Diffusion Constants for

Nucleic Acids by NMR. *J. Biomol. NMR* **1997**, *10* (3), 255–262.
(10) Plimpton, S. Fast Parallel Algorithms for Short-Range Molecular Dynamics. *Journal of Computational Physics*. 1995, pp 1–19.
(11) Jorgensen, W. L.; Maxwell, D. S.; Tirado-Rives, J. Development and Testing of the OLPS All-Atom Force Field on Conformational Energetics and Properties of Organic Liquids. *J. Am. Chem. Soc.* **1996**, *118* (15), 11225–11236.
(12) Canongia Lopes, J. N.; Pádua, A. A. H.; Shimizu, K. Molecular Force Field for Ionic Liquids IV: Trialkylimidazolium and Alkoxycarbonyl-Imidazolium Cations; Alkylsulfonate and Alkylsulfate Anions. *J. Phys. Chem. B* **2008**, *112* (16), 5039–5046.
(13) Canongia Lopes, J. N.; Pádua, A. A. H. CL&P: A Generic and Systematic Force Field for Ionic Liquids Modeling. *Theor. Chem. Acc.* **2012**, *131* (3), 1–11.
(14) Jorgensen, W. L.; Chandrasekhar, J.; Madura, J. D.; Impey, R. W.; Klein, M. L. Comparison of Simple Potential Functions for Simulating Liquid Water. *J. Chem. Phys.* **1983**, *79* (2), 926–935.
(15) Chen, H. C.; Chen, S. H. Diffusion of Crown Ethers in Alcohols. *J. Phys. Chem.* **1984**, *88* (21), 5118–5121.
(16) Ortega, A.; García de la Torre, J. Hydrodynamic Properties of Rodlike and Disklike Particles in Dilute Solution. *J. Chem. Phys.* **2003**, *119* (18), 9914.
(17) Perrin, F. Mouvement Brownien D'un Ellipsoide - I. Dispersion Diélectrique Pour Des Molécules Ellipsoidales. *J. Phys. le Radium* **1934**, *5* (10), 497–511.
(18) Perrin, F. Mouvement Brownien D'un Ellipsoide (II). Rotation Libre et Dépolarisation Des Fluorescences. Translation et Diffusion de Molécules Ellipsoidales. *J. Phys. le Radium* **1936**, *7* (1), 1–11.
(19) Koenig, S. H. Brownian Motion of an Ellipsoid: A Correction to Perrin's Results. *Biopolymers* **1975**, *14*, 2421–2423.
(20) Macchioni, A.; Ciancaleoni, G.; Zuccaccia, C.; Zuccaccia, D. Determining Accurate Molecular Sizes in Solution through NMR Diffusion Spectroscopy. *Chem. Soc. Rev.* **2008**, *37* (3), 479–489.